

Modeling Wilms tumor in human kidney organoids

Inauguraldissertation

zur

Erlangung der Würde einer Doktorin der Philosophie

vorgelegt der

Philosophisch-Naturwissenschaftlichen Fakultät

der Universität Basel

von

Verena Waehle

aus Deutschland

Basel, 2021

Originaldokument gespeichert auf dem Dokumentenserver der Universität Basel
edoc.unibas.ch

Genehmigt von der Philosophisch-Naturwissenschaftlichen Fakultät

auf Antrag von

Prof. Dr. Susan Gasser

Dr. Jörg Betschinger

Prof. Dr. Soeren Lienkamp

Basel, den 15.12.2020

Prof. Dr. Martin Spiess

Dekan

Table of contents

| | |
|--|------------|
| I. SUMMARY | V |
| II. LIST OF ABBREVIATIONS | VII |
| III. LIST OF FIGURES | XI |
| 1. INTRODUCTION | 1 |
| 1.1 Embryonic kidney development | 1 |
| 1.2 Wilms tumor | 4 |
| 1.2.1 Epidemiology | 4 |
| 1.2.2 Genetics | 5 |
| 1.2.3 Model systems | 7 |
| 1.2.3.1 <i>In vitro</i> | 7 |
| 1.2.3.2 <i>In vivo</i> | 9 |
| 1.3 Human induced pluripotent stem cells and the advent of organoid systems | 10 |
| 1.3.1 Human organoid systems | 10 |
| 1.3.2 Generation of kidney organoids | 11 |
| 2. AIM OF THIS THESIS | 15 |
| 3. RESULTS | 17 |
| 3.1 Experiments using a combined protocol by Taguchi et al. and Brown et al. | 17 |
| 3.1.1 Generation of hiPSC-derived kidney organoids | 17 |
| 3.1.2 Inducible overexpression of LIN28A in human kidney organoids | 19 |
| 3.2 Generation of kidney organoids using the protocol developed by Morizane et al. | 22 |
| 3.3 Overexpression of Wilms tumor oncogenes in kidney organoids - Morizane protocol | 27 |
| 3.3.1 Generating new Wilms tumor oncogene cell lines | 27 |
| 3.3.2 Characterization of Wilms tumor oncogene overexpression phenotypes | 29 |
| 3.3.3 Additional observations | 34 |
| 3.4 Mimicking β-catenin stabilization by prolonged treatment of organoids with CHIR 37 | 37 |

| | |
|--|------------|
| 3.5 Inducible knockout of <i>WT1</i> in developing human kidney organoids | 40 |
| 3.5.1 Generation of hiPSC lines with an inducible <i>WT1</i> knockout | 40 |
| 3.5.2 Phenotypic characterization of <i>WT1</i> KO organoids | 40 |
| 3.5.3 <i>WT1</i> KO time course | 43 |
| 3.5.4 Influence of <i>WT1</i> KO on different processes during organoid development | 48 |
| 3.6 RNA-seq of <i>WT1</i> KO and wildtype samples | 53 |
| 3.6.1 Quality control experiments | 53 |
| 3.6.2 Transcriptional changes upon <i>WT1</i> KO reflect impaired differentiation and maintenance of progenitor cells | 55 |
| 3.6.3 Deregulated gene clusters overlap with gene sets that define fetal kidney cell types | 57 |
| 3.6.4 Transcriptional changes in <i>WT1</i> KO organoids are conserved in Wilms tumor patients | 61 |
| 3.7 Competition between <i>WT1</i> KO d9 NPCs and wildtype NPCs | 64 |
| 3.8 Functional properties of <i>WT1</i> KO organoid-derived cells | 67 |
| 3.8.1 Serial passaging of KO ^{d4-7} cells derived from d21 organoids with wildtype d9 NPCs | 67 |
| 3.8.2 Transplantation of organoid-derived KO ^{d4-7} cells into wildtype organoids | 71 |
| 3.8.2.1 Transplantation in the presence of growth factors | 71 |
| 3.8.2.2 Transplantation in the absence of growth factors | 74 |
| 4. DISCUSSION | 77 |
| 4.1 Overexpression of LIN28 – divergent phenotypes in organoids and mice | 77 |
| 4.2 Activation of canonical WNT signaling by CHIR may mask effects of SIX2 and SIX2 Q177R overexpression in human kidney organoids | 82 |
| 4.3 Ectopic activation of WNT/β-catenin signaling in kidney organoids via CHIR recapitulates its roles during kidney development | 85 |
| 4.4 <i>WT1</i> KO organoids recapitulate roles of WT1 during kidney development | 89 |
| 4.5 <i>WT1</i> KO organoids transcriptionally resemble human Wilms tumors | 91 |
| 4.6 Kidney organoids and mouse models allow to study Wilms tumor initiation | 92 |
| 4.7 Later loss of WT1 is consistent with defects in podocyte development | 95 |
| 4.8 <i>WT1</i> KO organoids extend the scope of existent kidney disease models | 96 |
| 4.9 <i>WT1</i> KO organoids contribute a novel developmental tumor model | 98 |
| 4.10 Limitations and future perspectives of hiPSC-derived Wilms tumor organoids | 101 |
| 5. CONCLUSION | 105 |

| | |
|---|------------|
| 6. METHODS | 107 |
| 6.1 Cell culture | 107 |
| 6.1.1 Culture of human iPSCs | 107 |
| 6.1.2 Generation of kidney organoids | 107 |
| 6.1.3 Dissociation of kidney organoids into single cells | 109 |
| 6.2 Measuring organoid growth | 109 |
| 6.3 Functional assays | 110 |
| 6.3.1 Cleaved Caspase Assay | 110 |
| 6.3.2 Mixing of <i>WT1</i> KO and GFP-expressing wildtype d9 NPCs | 110 |
| 6.3.3 Serial passaging of cells derived from d21 organoids | 111 |
| 6.3.4 Transplantation of cells derived from d21 organoids or d9 NPCs into GFP-expressing wildtype organoids | 111 |
| 6.4 Molecular biology: Generation of Dox-inducible Wilms tumor oncogene lines | 112 |
| 6.5 Lentivirus production and transduction | 113 |
| 6.6 RNA isolation, cDNA synthesis, qPCR | 113 |
| 6.7 Flow cytometry and FACS | 114 |
| 6.7.1 Live cells | 114 |
| 6.7.2 Flow cytometry of fixed and stained cells | 114 |
| 6.7.3 High-throughput flow cytometry analysis | 114 |
| 6.7.4 FACS-based purification of Wilms Tumor oncogene lines | 115 |
| 6.8 Immunofluorescence staining of kidney organoids | 115 |
| 6.9 RNA-seq | 117 |
| 7. LIST OF MATERIALS | 119 |
| 8. ACKNOWLEDGEMENTS | 125 |
| 9. REFERENCES | 127 |

I. Summary

Wilms tumor is a pediatric kidney cancer that affects one in 10,000 children and is thought to arise from impaired nephrogenesis, leading to an expansion of immature cells at the expense of functional kidney tissue. In the past years, numerous genetic alterations associated with Wilms tumor have been identified. These include loss of the tumor suppressor gene *WT1*, biallelic expression of *IGF2*, as well as mutations in *CTNNB1*, miRNA processing genes like *LIN28* and *DROSHA*, and the kidney progenitor transcription factors *SIX1* and *SIX2*. Several model systems have been developed to study Wilms tumor, including cell lines, transgenic mice, patient-derived xenografts, and three-dimensional cultures from patient tissues. However, these systems often fail to recapitulate tumor properties accurately, and most of them are generated from patient tumors and are therefore unsuitable to study tumor initiation. Pluripotent stem cell-derived kidney organoids recapitulate human kidney development *in vitro* and largely reflect the cellular composition and architecture of the kidney. In combination with gene editing technologies, they offer a promising platform to study Wilms tumorigenesis.

In this thesis, I introduced previously described Wilms tumor mutations into human kidney organoids in order to develop an *in vitro* model for Wilms tumor.

We showed that overexpression of the miRNA processing genes *LIN28A* and *LIN28B* impairs organoid formation, without retaining kidney progenitor cells or enhancing proliferation. We observed similar phenotypes upon induction of the nephron progenitor transcription factor *SIX2* and its Wilms tumor-specific variant *SIX2 Q177R*. This indicates that overexpression of both, *SIX2* / *SIX2 Q177R* and *LIN28A* / *B* are insufficient to induce Wilms tumorigenesis in kidney organoids.

Moreover, we used ectopic chemical activation of canonical WNT signaling to mimic a stabilizing mutation of *CTNNB1* and found defects in epithelialization and nephron patterning. While this recapitulates known functions of WNT signaling in nephrogenesis, further experiments are needed to confirm if this reflects a Wilms tumor phenotype.

Finally, loss of the tumor suppressor gene *WT1* results in a Wilms tumor phenotype accompanied by a developmental arrest of kidney progenitors, enhanced proliferation and impaired differentiation into nephron cell types. As shown by transcriptional profiling, *WT1* KO organoids resemble human Wilms tumors and share a subtype-specific upregulation of muscle-related transcription. Using serial passaging and *in vitro* transplantation experiments, we showed that cells derived from *WT1* KO organoids can be maintained in a *SIX2*-expressing state in the presence of “fetal” and differentiated wildtype cells.

Summary

In conclusion, we developed the first human kidney organoid model for Wilms tumor. We provide evidence for the applicability of kidney organoids to study kidney development and developmental diseases, and for their use as a surrogate system for tumor cell propagation. This work sets the stage for generating additional organoid models for pediatric kidney cancers, and proposes to extend the use of kidney organoids as transplantation platforms in kidney cancer research.

II. List of abbreviations

| | |
|------------|--|
| 2D | two-dimensional |
| 3D | three-dimensional |
| AT/RT | atypical teratoid/rhabdoid tumor |
| BDM | basic differentiation medium |
| BMP | bone morphogenetic protein |
| BrdU | bromodeoxyuridine |
| BSA | bovine serum albumin |
| BWS | Beckwith-Wiedemann syndrome |
| Cas9 | clustered regularly interspaced short palindromic repeats associated protein 9 |
| C. elegans | Caenorhabditis elegans |
| CHIR | CHIR99021 |
| ChIP-seq | chromatin immunoprecipitation sequencing |
| CNS | central nervous system |
| Cre | Cre recombinase |
| CRISPR | clustered regularly interspaced short palindromic repeats |
| CT | cycle threshold |
| d | day |
| DDS | Denys-Drash syndrome |
| DMEM | Dulbecco's Modified Eagle Medium |
| Dox | doxycycline |
| E | embryonic day |
| EB | embryoid body |
| ESC | embryonic stem cell |
| FACS | fluorescence-activated cell sorting |
| FC | fold change |
| FCS | fetal calf serum |
| FGF | fibroblast growth factor |

List of abbreviations

| | |
|---------------|--|
| FGFR | FGF receptor |
| FWT | Familial Wilms Tumor |
| GNDF | glial cell-derived neurotrophic factor |
| GSK-3 β | glycogen synthase kinase-3 β |
| GFP | green fluorescent protein |
| GO | gene ontology |
| gRNA | guide RNA |
| h | hour/s |
| hiPSCs | human induced pluripotent stem cells |
| HTS | High Throughput Sampler |
| IF | immunofluorescence |
| iPSCs | induced pluripotent stem cells |
| ITS | Insulin-Transferrin-Selenium |
| KICH | kidney chromophobe carcinoma |
| KIRC | kidney clear cell carcinoma |
| KIRP | kidney papillary cell carcinoma |
| KIM-1 | kidney injury molecule-1 |
| KO | knockout |
| LTL | lotus tetragonolobus lectin |
| MRTK | malignant rhabdoid tumor of the kidney |
| MET | mesenchymal-to-epithelial transition |
| mins | minutes |
| miRNA | micro RNA |
| MM | metanephric mesenchyme |
| ND5 | ND41865 |
| Nes | Nestin |
| NPC | nephron progenitor cell |
| p | passage |
| PBS | Phosphate Buffered Saline |
| PC | principle component |
| PCA | principle component analysis |
| PCR | polymerase chain reaction |

| | |
|-----------|---|
| PDTX | patient-derived tumor xenograft |
| PFA | paraformaldehyde |
| PKD | polycystic kidney disease |
| qPCR | quantitative real-time polymerase chain reaction |
| RNA-seq | RNA-sequencing |
| RFP | red fluorescent protein |
| ROCK | rho-associated protein kinase |
| RT | room temperature |
| rtTA | reverse tetracycline transactivator |
| scRNA-seq | single-cell RNA sequencing |
| SD | standard deviation |
| SEM | standard error of the mean |
| t-SNE | t-distributed stochastic neighbor embedding |
| TRE | tetracycline response element |
| UB | ureteric bud |
| UPL | Universal Probe Library |
| WAGR | Wilms Tumor, aniridia, genitourinary tract abnormalities and mental retardation |
| WNT | Wingless-related integration site |
| YEATS | YAF9, ENL, AF9, TAF14, SAS5 |

III. List of figures

Figure 1. Schematic representation of kidney development.

Figure 2. Kidney organoid differentiation according to the Taguchi/Brown protocol.

Figure 3. LIN28A overexpression induces a Wilms tumor-like phenotype in kidney organoids.

Figure 4. Kidney organoid differentiation according to the Morizane protocol.

Figure 5. Image- and flow cytometry-based characterization of kidney organoids.

Figure 6. Generation of hiPSC lines with Dox-inducible Wilms tumor oncogenes.

Figure 7. Early overexpression of Wilms tumor oncogenes impairs the development of mature kidney structures.

Figure 8: SIX2 expression is not maintained upon LIN28A or LIN28B overexpression.

Figure 9. Proliferation is not elevated in Wilms tumor oncogene-expressing kidney organoids.

Figure 10. Wilms tumor oncogenes are induced in d21 organoids and d9 NPCs.

Figure 11. Prolonged activation of WNT signaling in kidney organoids disrupts differentiation.

Figure 12. Inducible KO of *WT1* results in maintenance of SIX2-expressing cells in d21 organoids.

Figure 13. *WT1* KO at different time points elicits distinct phenotypes in *WT1* KO organoids.

Figure 14. *WT1* KO organoids contain fewer nephron structures, upregulate IGF2 and harbor novel SIX2-EPCAM double-positive cells.

Figure 15. Influence of *WT1* KO on different processes during organoid development.

Figure 16. Set-up and quality controls of RNA-seq experiments.

Figure 17. *WT1* KO organoids are developmentally delayed.

Figure 18. Deregulated genes upon *WT1* KO overlap with gene sets that define fetal kidney cell types.

Figure 19. Gene clusters 1, 8, 13, and 17 are linked to NPCs, proliferation and kidney differentiation.

Figure 20. *WT1* KO organoids resemble human Wilms tumor.

Figure 21. NPCs derived from KO^{d4-7} cells outcompete wildtype NPCs during organoid growth.

Figure 22. SIX2-expressing cells from KO^{d4-7} d21 organoids can be maintained for several passages in the presence of wildtype NPCs.

Figure 23. SIX2-expressing KO^{d4-7} cells from d21 organoids expand within wildtype organoids in the presence of growth factors.

Figure 24. SIX2-expressing KO^{d4-7} cells from d21 organoids expand within wildtype organoids in the absence of growth factors.

1. Introduction

Human cancer cell lines, genetic mouse models and patient-derived tumor xenografts (PDX) have been seminal for advancing both cancer research and drug discovery (Kim et al., 2020).

Most human cancer cell lines are cheap and easy to maintain, but lack a three-dimensional (3D) organization and the physiological context of a tissue. Mouse models provide both a tissue environment, three-dimensionality, as well as additional influencing factors like blood vessels and an immune system, but they do not reflect features that are specific to human tumorigenesis. PDX models represent human 3D tissues that are transplanted into an organismal context, but such models are difficult to use for drug testing. Most human cancer model systems, unfortunately, are poor predictors of clinical efficiency (Kim et al., 2020).

Wilms tumor is a pediatric kidney cancer that first manifests in children but is thought to arise due to impaired nephrogenesis. Histological analyses of patient biopsies show the presence of undifferentiated progenitor cells, which normally only exist temporarily during development and disappear before birth (Hohenstein et al., 2015; Rivera and Haber, 2005; Treger et al., 2019). While samples from Wilms tumor patients provide snapshot insights into the advanced tumor, they do not inform about tumor initiation. Vice versa, mouse models can model tumorigenesis but may lack important features specific to human tumorigenesis. Therefore, models recapitulating the etiology of Wilms tumors will become essential to study mechanisms of tumorigenesis, and may allow for the identification of relevant biomarkers and, if scalable, provide experimental models for drug discovery and development.

1.1 Embryonic kidney development

In order to recognize how faulty developmental programs cause Wilms tumors, we need to understand how the kidney develops under healthy conditions.

The postnatal kidney is a highly complex organ that contains more than 25 different cell types. Functionally, the kidney filters our blood to produce the urine, and thereby reabsorbs important nutrients and ions, and actively secretes nitrogenous waste products. In addition, the kidney is involved in regulating our blood pressure, as well as bone density and erythropoiesis (reviewed in Little and Combes, 2019).

During mammalian development, the primitive streak generates trunk mesoderm, which is patterned along the mediolateral axis into (1) paraxial mesoderm that gives rise to the somites, (2) lateral plate mesoderm that gives rise to the limb buds and heart, and (3) intermediate

mesoderm that gives rise to the genitourinary tract. Along the anterior-posterior axis of the intermediate mesoderm both, the Wolffian duct and nephrogenic cord are specified. From the nephrogenic cord itself, three distinct excretory organs develop sequentially along the anterior-posterior axis, the pronephros, mesonephros and metanephros. Both, pronephros and mesonephros develop structures similar to nephrons, but these eventually regress, while the metanephros ultimately develops into the permanent kidney (Little et al., 2016).

To achieve this, the anterior and posterior regions of the intermediate mesoderm contribute to distinct portions of the kidney: the anterior intermediate mesoderm generates the Wolffian Duct from which the ureteric epithelium develops, and within the posterior intermediate mesoderm a condensation of the nephrogenic cord forms the metanephric mesenchyme (MM), the precursor of the nephron (Taguchi et al., 2014; Xu et al., 2014).

Reciprocal interactions between cells of these two tissues initiate the formation of the kidney (Fig. 1). At the onset of nephrogenesis, a caudal outgrowth of the Wolffian duct, named ureteric bud (UB), invades the adjacent MM that contains SIX2-positive nephron progenitors and FOXD1-positive stromal progenitors. Invasion of the UB induces the MM to condense at its tip into cap mesenchyme, which leads to the formation of a self-renewing population of SIX2- and CITED1-positive nephron progenitor cells (NPCs), while the FOXD1-positive stromal progenitors are not included into cap mesenchyme (Little et al., 2016). Cells at the tip of the UB secrete signaling factors, including bone morphogenetic protein (BMP), fibroblast growth factor (FGF) and low levels of Wingless-related integration site (WNT) 9b, which help maintain a proliferating NPC population surrounding the bud tip. Signals derived from FOXD1-positive stromal cells also contribute to this niche. In contrast, UB cells at the transition from tip to stalk secrete higher levels of WNT, which induces adjacent NPCs to express *WNT4*, and give rise to pre-tubular aggregates. These subsequently undergo a mesenchymal-to-epithelial transition (MET) to form the first epithelial precursors of the later nephron.

Reversely, NPCs of the cap mesenchyme provide BMP, FGF and glial cell-derived neurotrophic factor (GDNF) signals that induce the outgrowth and branching of the UB. Collectively, these reciprocal interactions ensure a balance between maintenance of a progenitor cell pool, UB branching, and induction of nephrogenesis (Little and Combes, 2019; Little et al., 2016).

After MET, early epithelia are arranged in renal vesicles, which display an initial proximal-distal patterning. Renal vesicles develop into primitive tubules called comma- and s-shaped bodies. In these structures, patterning is refined into proximal, medial and distal portions, which correspond to later segments of the mature kidney. Ultimately, these primitive tubules give rise to the podocytes of the glomerulus, proximal tubules, loop of Henle and distal tubules. A number of genes that are expressed in specific regions of developing nephrons have been implicated in regulating the acquisition of specific cell type identities, including *LHX1*, *HNF1B* and *WT1*.

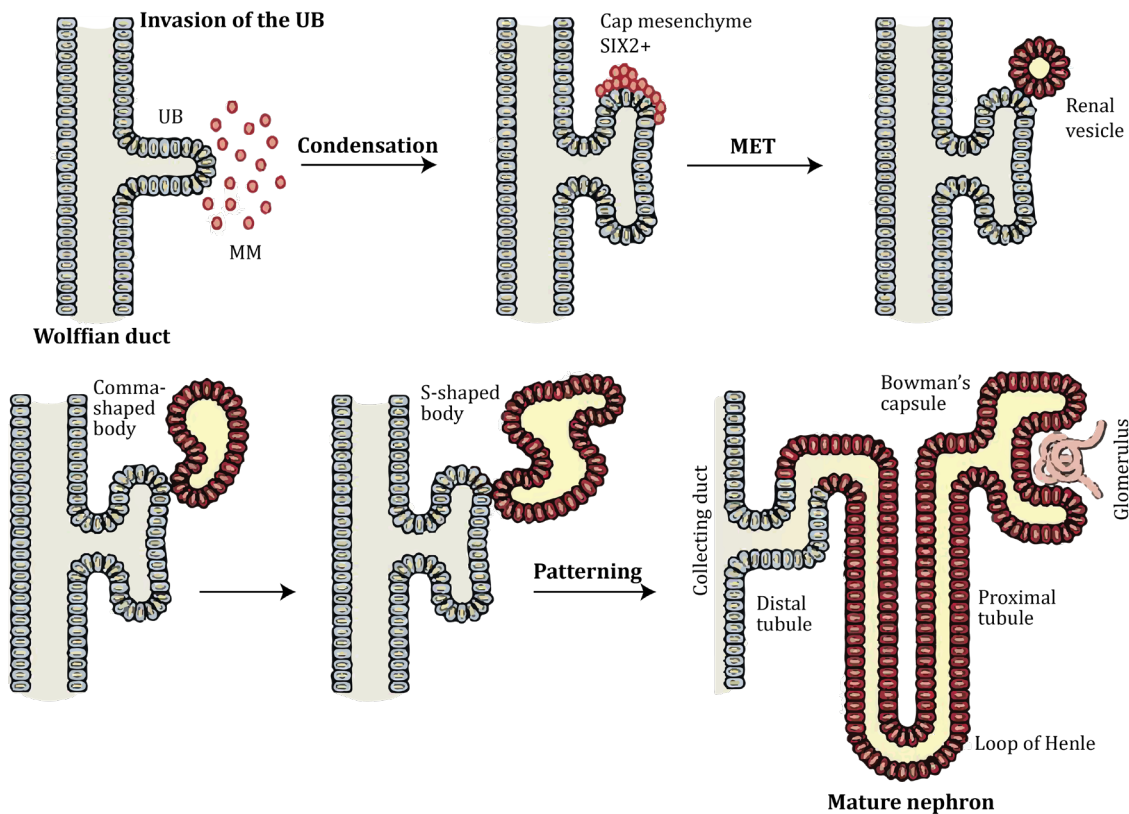


Figure 1. Schematic representation of kidney development. (adapted from Hohenstein et al. 2015)

Reciprocal interactions between the UB and MM induce the MM to condense into cap mesenchyme, which contains SIX2- and CITED1-positive NPCs. Additional signals from the UB induce NPCs either to proliferate or to undergo an MET that leads to the formation of renal vesicles, which further develop, into comma- and s-shaped bodies. Patterning of these structures ultimately gives rise to the mature nephron, which consists of a glomerulus with a Bowman's capsule and a tubular system. At its distal end, it connects to the collecting duct, which itself develops from the UB. In Wilms tumor, nephron development is arrested prematurely.

In addition, both Notch and WNT signaling play a role in nephrogenesis and nephron patterning (Little and Combes, 2019). A gradient of WNT signaling activity is particularly involved in patterning the proximal-distal axis of the developing nephron. High WNT levels are present in the distal nephron and they gradually decrease via the medial portion to low levels in the proximal nephron. Notably, manipulations of this gradient in culture can tweak the proportions of distal (WNT activation) and proximal nephron elements (WNT inhibition) (Lindström et al., 2015). At the same time as nephrons form from renal vesicles, the ureteric epithelium branches repeatedly and itself gets patterned into distinct regions. Ultimately, the ureteric tree gives rise to the collecting duct system of the kidney, which connects to the distal tubules of the nephron and therefore ultimately allows the excretion of the urinary filtrate via the ureter into the bladder (Little and Combes, 2019).

In addition to cell types derived from the UB and the MM, the mature kidney contains supporting cell types, including endothelial cells and pericytes that make up the blood vessels, interstitial fibroblasts and more specialized stromal cells which are, among others, responsible for secreting

renin, an important regulator of blood pressure. However, a precise understanding of the developmental origins of these cell types and how their specification is regulated, is still lacking (Little et al., 2016).

The processes of progenitor proliferation, UB branching and MET continue throughout embryonic development. Right around birth in mice or at 36 weeks of gestation in humans, nephron progenitors undergo a final burst of commitment and give rise to the final set of nephrons (Hartman et al., 2007; Hinchliffe et al., 1991; Short et al., 2014). Consequently, the adult human kidney does not contain any nephron progenitors, and the final number of nephrons, on average around 1 million per kidney, is fixed at birth (Humphreys et al., 2008; Little and Combes, 2019).

1.2 Wilms tumor

1.2.1 Epidemiology

Nephroblastoma, or Wilms tumor, named after the German surgeon Max Wilms, affects one in 10,000 children each year (Stiller and Parkin, 1990). It makes up for around 7% of all pediatric cancers and 90% of all kidney cancers in children. Around 90% of Wilms tumors arise due to sporadic mutations and are restricted to one kidney only (Breslow et al., 1993; Miller et al., 1995). Children are diagnosed at a median age of three to four years in case of sporadic tumors (Breslow et al., 1988). However, Wilms tumor can also occur bilaterally or multifocally, especially in the context of cancer predisposition syndromes. These account for around 10% of Wilms tumor cases and are diagnosed at an earlier median age of two to three years (Scott et al., 2006).

Surgery and chemo-/ radiotherapy are the standard treatment paradigms applied to Wilms tumor patients and have considerably increased survival rates to around 90% in the past years. However, these treatments have non-negligible side effects, and there are certain higher risk variants of the disease that relapse more frequently and are associated with reduced survival rates. The underlying mechanisms are insufficiently understood and more research is needed to determine genetic risk factors as well as biomarkers for better risk stratification (reviewed in Treger et al., 2019).

Wilms tumor presents with a characteristic triphasic histology that comprises blastemal, stromal and epithelial cells (Hohenstein et al., 2015). This supports the theory that Wilms tumor arises from renal precursor cells, which undergo incomplete differentiation processes, resulting in aberrant nephrogenesis. Blastemal components appear very similar to the condensing MM of the developing kidney and are often found in so-called nephrogenic rests, which are thought to be

precursor lesions of Wilms tumor. Likewise, epithelial structures most closely resemble early tubules, including comma- and s-shaped bodies, and early glomeruli (Rivera and Haber, 2005; Treger et al., 2019). In fact, gene expression analyses of either Wilms tumor patient material (Gadd et al., 2012; Trink et al., 2018) or PDTX models (Dekel et al., 2006) showed expression patterns, that were similar to NPCs, un-induced MM or renal epithelium. Notably, the predominance of blastemal, stromal or epithelial cells helps defining different subclasses of Wilms tumors. Studies have suggested that such differences in Wilms tumor phenotype are determined by the identity and developmental stage of the tumor cell-of-origin and the subsequent arrest of kidney development (Gadd et al., 2012). This again supports the assumption that impaired nephrogenesis causes the formation of Wilms tumors.

1.2.2 Genetics

Considering its phenotypic appearance, it is not surprising that many of the genes mutated in Wilms tumor are related to embryonic kidney development. In fact, there are around 40 different genetic changes associated with Wilms tumor, but all of them occur at a very low frequency and rarely appear to be mutated in the same tumor (Treger et al., 2019). This is in contrast to other childhood malignancies, which have a small set of driver mutations. However, the median somatic mutation rate of Wilms tumor as a pediatric cancer is still much lower than that of adult kidney cancers, such as papillary renal cell carcinoma or clear cell renal cell carcinoma (Alexandrov et al., 2013; Ma et al., 2018).

The first gene identified to be causally connected to Wilms tumor is *WT1*. *WT1* encodes a zinc finger transcription factor that is expressed throughout kidney development, first in the intermediate mesoderm, then within the MM, in the proximal portion of early tubules and finally in podocytes of the glomerulus (Dong et al., 2015a; Hastie, 2017). *WT1* was discovered as a tumor suppressor gene through the study of syndromes that predispose to Wilms tumor. These include Wilms tumor, aniridia, genitourinary tract abnormalities and mental retardation (WAGR) syndrome, Denys-Drash syndrome (DDS), as well as Frasier syndrome (reviewed in Hastie, 2017; Rivera and Haber, 2005; Treger et al., 2019). In these cases, one mutant *WT1* allele is inherited while the other allele is inactivated during development. In fact, Alfred Knudson based his “two-hit”-model of tumor suppression on Wilms tumor, next to retinoblastoma and neuroblastoma (Knudson and Strong, 1972). In addition to causing Wilms tumor in the context of syndromes, mutations in *WT1* also appear in sporadic Wilms tumor, either as nonsense and missense mutations or splicing defects that are distributed throughout the entire coding sequence (Rivera and Haber, 2005).

Another syndrome, Beckwith-Wiedemann syndrome (BWS), is strongly associated with loss-of-imprinting at 11p15, which results in biallelic expression of *IGF2* (Scott et al., 2012). Other Wilms tumor predisposition syndromes include Simpson-Golabi-Behmel syndrome with mutations in *GPC3*, which result in activation of WNT signaling, Perlman syndrome with mutant *DIS3L2*, which disrupts micro RNA (miRNA) biogenesis, Li Fraumeni syndrome with mutant *TP53*, and Fanconi anemia with defective *BRCA2* and *PALB2*. Two other loci that upon mutation predispose to Wilms tumor, Familial Wilms tumor (FWT) 1 and FWT2, have not been fully characterized yet. There are several additional genes which are mutated in non-syndromic familial Wilms tumor cases (reviewed in Hohenstein et al., 2015; Rivera and Haber, 2005; Treger et al., 2019).

The great majority of Wilms tumors, however, does not occur in the context of germline mutations and/or predisposition syndromes but arises due to sporadic mutations. The best-characterized somatic mutations in Wilms tumor are very similar to those associated with the abovementioned syndromes and include *WT1*, biallelic expression of *IGF2*, activation of WNT signaling, as well as mutations in *TP53* and *MYCN*. Occasionally, these mutations also occur together, for example combinations of *WT1* loss-of-function and WNT signaling activation (Gadd et al., 2012; Hohenstein et al., 2015; Treger et al., 2019). In this case, CTNNB1 protein (=β-catenin), the effector of canonical WNT signaling, is protected from degradation by mutations of S45 that prevent phosphorylation and ubiquitylation (Amit et al., 2002). Similarly, mutations in the YAF9, ENL, AF9, TAF14, SAS5 (YEATS) domain of *MLL1* that alter its DNA-binding specificity co-occur with β-catenin activation (Perlman et al., 2015; Treger et al., 2019). WNT signaling plays important roles at multiple stages of kidney development, including primitive streak specification, maintenance of NPCs and their differentiation, and nephron patterning.

Genome-wide sequencing of Wilms tumor patient samples identified additional genes associated with Wilms tumorigenesis. These include genes involved in miRNA processing, such as *DROSHA*, *DICER1*, *DGCR8*, *XPO5* and *TARBP2* (Rakheja et al., 2014; Torrezan et al., 2014; Walz et al., 2015; Wegert et al., 2015). A recurrent E1147K point mutation in the RNase IIIb domain of *DROSHA* inhibits its RNase activity, while other mutations of *DROSHA*, *DGCR8* and *DICER1* impair their RNA-binding capacities. Mutations in *DROSHA* result in global downregulation of miRNAs including those of the *let-7* family (Rakheja et al., 2014; Torrezan et al., 2014). The miRNA processing protein LIN28 also inhibits *let-7* miRNA maturation. *LIN28B* copy number gains and consequential downregulation of *let-7* occur in Wilms tumor (Gadd et al., 2017), and overexpression of murine and human LIN28 induces tumorigenesis in a Wilms tumor mouse model (Urbach et al., 2014). Originally, *lin-28* was discovered as a heterochronic gene in *Caenorhabditis elegans* (*C. elegans*) development (Ambros and Horvitz, 1984), but has since been implicated in regulating pluripotency, stem cell self-renewal, tissue metabolism and cancer. Many

of these processes involve repression of *let-7* miRNA biogenesis (Nguyen and Zhu, 2015; Viswanathan and Daley, 2010; Viswanathan et al., 2009).

Sequencing of Wilms tumor patient samples also identified recurrent point mutations in the transcription factors SIX1 and SIX2. These mutations result in an amino acid substitution at position 177 (Q177R), which is located in the DNA binding domain and thus alters DNA-binding specificity of SIX1 and SIX2 (Gadd et al., 2017; Walz et al., 2015; Wegert et al., 2015). Interestingly, the SIX1/SIX2 Q177R mutations are specific to Wilms tumor and associated with a blastemal histology. Both SIX1 and SIX2 play important but independent roles during kidney development. In fact, SIX1 is required for the UB to invade the MM, which undergoes apoptosis upon loss of SIX1 (Xu et al., 2003). SIX2, on the other hand, prevents the differentiation of NPCs and thus helps maintaining a proliferating progenitor population during nephrogenesis (Park et al., 2012; Self et al., 2006). *SIX1* and *SIX2* mutations are associated with an upregulation of cell cycle genes in Wilms tumor patients, which therefore suggests a role in driving the proliferation of undifferentiated MM in Wilms tumor (Walz et al., 2015; Wegert et al., 2015).

The “Therapeutically Applicable Research to Generate Effective Treatments” (TARGET) initiative further expanded the list of Wilms tumor genes by means of whole-genome and whole-exome sequencing of 117 Wilms tumor samples (Gadd et al., 2017 and reviewed in Treger et al., 2019).

1.2.3 Model systems

Until now, several systems have been used to study Wilms tumor, including Wilms tumor cell lines, primary cultures, PDX models and transgenic mouse models. More recently, tubuloids, spheroids and organoids were derived from Wilms tumors and healthy kidneys.

1.2.3.1 *In vitro*

Wilms tumor cell lines have proven to be difficult to establish and there are only very few immortalized cell lines available, which often represent rare subclasses of Wilms tumor. The WiT-49 line was derived from a Wilms tumor lung metastasis with *TP53* mutations, and the WT-Pe.1 line contains various chromosomal aberrations. There are additional Wilms tumor lines published, but genetic profiling later on revealed that these lines actually arose from different tumors and not from Wilms tumor: the WT-CLS1 and G401 lines comprised rhabdoid tumor cells, the SK-NEP1 line developed from a Ewing sarcoma of the kidney, and the WCCS-1 originated from a clear cell sarcoma of the kidney (Murphy et al., 2019; Wegert et al., 2012). Therefore, the

available Wilms tumor cell lines either represent rare Wilms tumor subtypes or are derived from different kidney tumors, and are therefore not suitable for studying Wilms tumor.

Several groups have tried to establish Wilms tumor cell lines from primary tissues, with the aim to better represent the molecular heterogeneity of Wilms tumor. In fact, one group successfully generated long-term cultures derived from *WT1* mutant Wilms tumors (Royer-Pokora et al., 2010). In addition, primary cultures from Wilms tumors with different mutations were generated (Wegert et al., 2012). These cultures exhibit distinct life spans and ultimately undergo senescence. Since primary cultures proved to be transfectable, they are considered useful for studying additional genetic alterations or for testing potential new drugs. However, cell line generation and two-dimensional (2D) culture on plastic involve considerable cellular selection and a loss of genuine physiological properties of the tumor, which are required for an accurate Wilms tumor model system (Ben-David et al., 2019).

Recently, more advanced 3D models were developed from Wilms tumor patient samples, named tubuloids, spheroids and organoids.

Tubuloids were first developed when digested kidney tissue or even fragments derived from urine were embedded in Matrigel and cultured under elaborate conditions that were adapted from the culture of human intestinal stem cells (Schutgens et al., 2019). Tubuloids were successfully generated from healthy kidney and from two Wilms tumor patients. Such tumor tubuloids contained stromal, blastemal and epithelial cell types and showed elevated expression of *SIX2*, which was absent in tubuloids from corresponding healthy tissues.

Wilms tumor spheroids in turn were originally found as a by-product in the supernatant of primary cultures of Wilms tumor tissue. These spheroids are expandable upon suspension culture and allow the maintenance of blastemal tumor cells *in vitro*, which had not been achieved before (Wegert et al., 2019). Both tubuloids and spheroids represent the first 3D culture systems for Wilms tumor cells.

Even more recently, an entire organoid biobank representing pediatric cancers, including Wilms tumor, was established and these organoids were extensively characterized (Calandrini et al., 2020). In this study, organoids were derived from Wilms tumors and matching wildtype tissues and could be maintained in culture for more than 20 passages. Notably, organoids resembled their primary tumor-of-origin and retained their triphasic appearance. In fact, organoids from different Wilms tumor subtypes showed gene expression patterns consistent with histology, which demonstrated that the cellular heterogeneity of these Wilms tumors could be recapitulated in organoid cultures.

Collectively, Wilms tumor tubuloids, spheroids and organoids are derived from primary human tumors and recapitulate their features. In addition, they are easy to generate, affordable and offer

platforms for genetic manipulation and drug testing. Nevertheless, they represent the tumors at an advanced stage of the disease and are thus unsuitable for studying tumor initiation and the potential causal contributions of known Wilms tumor genes to tumorigenesis.

1.2.3.2 *In vivo*

In contrast to 2D and 3D cultures, mouse models are thought to recapitulate tumor physiology in an organismal context, and advances in gene editing technologies have enabled the generation of desired transgenic mouse lines. To date, several mouse models for Wilms tumor have been developed. The first relies on upregulation of *Igf2*, which mimics the loss-of-imprinting phenotype observed in Wilms tumor, together with an inducible and sporadic loss of WT1 (Hu et al., 2011). This model recapitulates a triphasic histology with blastemal predominance as well as upregulation of NPC markers. An extension of this model induces *Wt1* loss at later developmental stages and also combines it with stabilization of β -catenin, instead of *Igf2* (Huang et al., 2016). Another group reported one rare case of kidney overgrowth by depleting *Wt1* alone (Berry et al., 2015).

Building on a different class of Wilms tumor mutations, another model uses tissue-specific and inducible overexpression of murine and human LIN28 (Urbach et al., 2014). This manipulation results in the development of a Wilms tumor, which shows an expansion of cap mesenchyme. Notably, tumor cells undergo differentiation when Lin28 overexpression is switched off.

While mouse models represent different Wilms tumor subtypes, they recapitulate the histology of the corresponding human tumors only to a limited extent. In addition, some of these mouse models rely on genetic alterations that in humans occur sequentially and not simultaneously (like *Wt1* with *Igf2* or *Ctnnb1*). Moreover, they neglect the many additional classes of Wilms tumor. Finally, mouse and human physiology differ in important aspects, and the generation of transgenic lines is very time consuming and expensive (Kim et al., 2020).

A viable alternative to transgenic mice is the use of PDTX models, which were originally developed in order to facilitate faithful propagation of tumor tissue without the implicit selective pressures of 2D culture on plastic. In PDTX models, fragments derived from patient tumors are transplanted either orthotopically or ectopically into mice, which then serve as a vehicle to propagate the tissue and as a system to study tumor properties and therapy response (Hidalgo et al., 2014). In 2019, Murphy et al. (2019) generated a library of 45 xenograft models derived from diverse Wilms tumor subclasses. The models recapitulated the divergent histological features of their primary tumors as well as the expression of relevant markers for progenitors and nephrogenesis. In addition, they shared many genetic alterations with their primary tumors and showed very similar responses to chemotherapy. Therefore, PDTX are considered suitable

models to study disease progression and therapy response. However, it has been demonstrated repeatedly that Wilms tumor PDX models over time show an enrichment of blastemal histology and expression of blastema-related genes (Dekel et al., 2006; Garvin et al., 1987; Murphy et al., 2019). This suggests selection during prolonged propagation of tumors in mice, which may preclude their applicability as preclinical models. Moreover, similar to transgenic mouse lines, the generation of PDX is slow, expensive and does not allow for high-throughput screens (Kim et al., 2020). Finally, alike tubuloids, spheroids and Wilms tumor organoids, PDX models are generated from fully developed tumor tissues and are therefore unsuitable for studying tumor initiation.

Taken together, the currently available model systems for Wilms tumor each have their own advantages but none combines all benefits in the same system. For studying Wilms tumorigenesis, we need a system that is of human origin, developmental, physiological, easily accessible, scalable and amenable to both, genetic manipulation and drug screenings. Therefore, we turned to recently developed pluripotent stem cell-derived kidney organoid systems.

1.3 Human induced pluripotent stem cells and the advent of organoid systems

1.3.1 Human organoid systems

The advent of mouse and human induced pluripotent stem cells (iPSCs) realized by Shinya Yamanaka in 2006 (Takahashi and Yamanaka, 2006) and 2007 (Takahashi et al., 2007) awarded him the Nobel Prize in Medicine and Physiology in 2008, and demarcates one of the great milestones in the younger history of biology. Since then, the application of human induced pluripotent stem cells (hiPSCs) has greatly shaped many disciplines of biomedical research. Having similar developmental potential as human embryonic stem cells (ESCs), hiPSCs offer a variety of applications that range from studying early processes of human development to the ambitious aim of building stem cell-derived transplantable cell types or even whole organs. One intermediate step towards this goal is the generation of miniature organs, or organoids. Per definition, organoids are generated from pluripotent stem cells or tissue progenitor cells by manipulating signaling pathways that are similarly active during *in vivo* development or regenerative processes. Organoids present as 3D entities, that recapitulate at least partially the cell type composition of the respective organ and its spatial organization, and they fulfill some of the specific functions of the tissue (Lancaster and Huch, 2019; Lancaster and Knoblich, 2014). To date, organoids representing a variety of tissues have been developed, including the brain, optic

cup, intestine, liver and lung, as well as the kidney, endometrium and blood vessels (reviewed in Clevers, 2016; Kim et al., 2020; Lancaster and Huch, 2019)

The generation of organoids from pluripotent stem cells usually comprises two steps: first, the specification of a tissue-specific progenitor population, and second the differentiation and spontaneous self-organization of this progenitor to give rise to organ-specific cell types and structures. The second step is supported by creating cell culture environments that allow 3D organoid growth, including 3D matrices, scaffolds, suspension culture or liquid-air-interface systems (Kim et al., 2020).

Embryonic development is achieved through a series of differentiation events and lineage choices that are guided by the localized activation and inhibition of a set of signaling pathways that confer very specific cell type identities in the correct position at the right time. In general, mimicking such lineage choices *in vitro*, by providing the appropriate signals at the correct time in the right concentrations, instructs specific cell types in a cell culture dish. In order to do so, a very detailed understanding of how these cell types or tissues develop *in vivo* is required (Lancaster and Huch, 2019; Little et al., 2016).

1.3.2 Generation of kidney organoids

The first step in developing kidney organoids from pluripotent stem cells is the specification of nephron progenitors of the MM and/or precursors of the ureteric epithelium in the UB (Little and Combes, 2019; Little et al., 2016). As mentioned, this requires the understanding and subsequent faithful recapitulation of *in vivo* kidney development. Indeed, one of the first kidney organoid protocols was based on characterizing the key developmental decisions in mouse kidney development (Taguchi et al., 2014). In a backward-approach starting from the embryonic day (E) 11.5 MM, this study uncovered the signaling pathways that are crucial for the induction of several intermediate cell populations on the developmental path from pluripotency to nephron progenitor identity. This knowledge was first translated into a step-wise differentiation protocol to derive mouse NPCs from mouse ESCs. Subsequently, by adjusting the growth factors to induce mesoderm formation and increasing the incubation periods, the authors developed a similar protocol to generate human nephron progenitors from hiPSCs. Notably in this protocol, the differentiation of pluripotent stem cells into nephron progenitors is carried out in an embryoid body (EB)-based format. Afterwards, both, mouse and human NPC-containing EBs are co-cultured with embryonic spinal cord as a source of exogenous WNT signals at the liquid-air-interface, to induce NPCs to differentiate and self-organize (Taguchi et al., 2014).

Since then, several additional protocols to generate human kidney organoids have been published: The protocol by Takasato et al. (2015) takes advantage of different durations of WNT signaling activation to simultaneously induce UB and MM, which are derived from anterior and posterior intermediate mesoderm, respectively. While progenitor differentiation is carried out in a monolayer format, cells are subsequently detached, aggregated and transferred onto transwell filters for organoid culture. Here, treatment with the glycogen synthase kinase 3 β (GSK-3 β) inhibitor CHIR99021 (CHIR) substitutes for embryonic spinal cord to activate WNT signaling (Takasato et al., 2015).

Similarly, the protocol by Morizane et al. (2015) derives NPC-containing MM using monolayer culture. Afterwards, cells are detached and seeded into U-bottom ultra-low attachment plates in the presence of CHIR to facilitate organoid culture. Deriving organoids in multi-well plates enables the simultaneous generation of many organoids in parallel (Morizane and Bonventre, 2017b; Morizane et al., 2015).

Furthermore, in a protocol by Freedman et al. (2015) iPSCs are embedded in a Matrigel sandwich, which allows spheroid formation (Freedman et al., 2015).

Notably, these four protocols apply very different culture formats and substrates, and use distinct growth factor cocktails and incubation periods. However, all of them generate kidney organoids that contain nephron-like structures composed of glomeruli, proximal and distal tubules as well as loop of Henle, and in case of Takasato et al., also UB-derived collecting ducts (reviewed in Little and Combes, 2019; Morizane and Bonventre, 2017; Nishinakamura, 2019). In addition, single-cell RNA sequencing (scRNA-seq) of some of these organoids revealed that they also contain small fractions of endothelial cells as well as off-target populations like muscle and neuronal cell types (Combes et al., 2019; Wu et al., 2018).

Importantly, both whole-organoid RNA sequencing (RNA-seq) and scRNA-seq demonstrated that organoids correspond to cell types of the fetal kidney. In fact, Takasato et al. (2015) mapped kidney organoids to developmental stages of Trimester I kidneys. A more precise integration of cell populations identified in human kidney organoids and human fetal kidney confirmed an overlap of stromal, endothelial and nephron clusters between these two sets, and the relative abundances of these and other cell types in organoids and fetal kidney were very similar (Combes et al., 2019).

Following the development of these original protocols, several groups have published optimizations or extensions thereof. These efforts aimed at increasing cell type maturation, up-scaling for drug screening, enabling co-cultures and developing disease models (reviewed in Little and Combes, 2019).

Collectively, hiPSC-derived kidney organoids represent an *in vitro* system that recapitulates the developing fetal kidney, and thus encompasses the period of Wilms tumorigenesis. It offers unlimited supply of material, which is particularly scarce for pediatric cancers. In addition, kidney organoids are comparably cheap to generate and amenable to genetic manipulations.

Therefore, we decided to employ hiPSC-derived kidney organoids to study the role of different Wilms tumor patient alterations in Wilms tumorigenesis, aiming to expand existing preclinical models for Wilms tumor and to study the developmental roots of cancer initiation.

2. Aim of this thesis

Wilms tumor is a common pediatric kidney cancer that is thought to arise from impaired nephrogenesis. In the past years, numerous genetic alterations associated with Wilms tumor have been identified. Although various model systems exist, they are limited in their ability to recapitulate disease initiation. HiPSC-derived kidney organoids provide an alternative system to study Wilms tumorigenesis.

In my PhD project, I addressed the following points:

1. Establish and characterize a hiPSC-derived kidney organoid system
2. Probe the effects of selected Wilms tumor patient mutations in hiPSC-derived kidney organoids:
 - LIN28A and LIN28B overexpression as representatives of miRNA processing genes
 - A SIX2 Q177R variant as an NPC transcription factor
 - Treatment with CHIR in order to mimic stabilizing β -catenin mutations
 - Knockout of *WT1* as a tumor suppressor gene
3. Compare potential Wilms tumor organoid phenotypes and gene expression signatures to Wilms tumor patient data
4. Characterize functional properties of Wilms tumor organoids

3. Results

3.1 Experiments using a combined protocol by Taguchi et al. and Brown et al.

3.1.1 Generation of hiPSC-derived kidney organoids

As explained above, pluripotent stem cell-derived organoids are generated in two steps by first deriving tissue progenitor cells and subsequently inducing their differentiation and self-organization. We decided to take advantage of the protocol by Taguchi et al. (2014), which elegantly recapitulates embryonic development to derive NPCs, by sequentially modulating signaling pathways known to be relevant for the respective developmental steps *in vivo*, including BMP, Activin, FGF and WNT signaling. Following this principle, pluripotent stem cells are aggregated into EBs, steered through epiblast and mesodermal fates, further specified and regionalized into posterior intermediate mesoderm, and ultimately into the nephron progenitors of the MM (Fig. 2A). We can follow this developmental trajectory by measuring the expression of marker genes that are specific for distinct developmental stages (Fig. 2A, blue). In the original protocol, EBs are subsequently cultured with embryonic spinal cord as a source of canonical WNT signaling. However, we decided to adapt a protocol developed by Brown et al. that utilizes chemical activation of WNT signaling by CHIR (Brown et al., 2015 and A. Brown, personal communication). We placed each EB onto a polycarbonate filter sitting on CHIR-containing organoid culture medium. This induced the differentiation and self-organization of NPCs into nephron structures. Using this combined setup (=Taguchi/Brown protocol), we obtained one single organoid per EB after a total of 21 days. We tested several hiPSC lines with this protocol and chose the ND41865 (ND5) line for our experiments, as it showed the most efficient and reliable differentiation (data not shown).

To better characterize the system, we collected NPCs at day (d) 14 and assessed the expression of selected marker genes via quantitative real-time polymerase chain reaction (qPCR) (Fig. 2B). We detected expression of *HOXA10* and *HOXA11*, which are typically expressed in posterior tissues. In addition, NPCs expressed classical markers of posterior intermediate mesoderm and MM, including *OSR1*, *PAX2*, *WT1* as well as the *bona fide* nephron progenitor marker *SIX2*. This indicates that we indeed derived NPCs with our protocol. Next, we measured the expression of such progenitor markers and additional genes in d21 organoids (Fig. 2C). We detected the expression of mature kidney markers, like *NPHS1*. In addition, organoids expressed *WT1*, which is not only present in NPCs but also in podocytes of the glomerulus. We also detected expression of *CDH1*, which is expressed in early tubules after MET and later is confined to the distal tubules

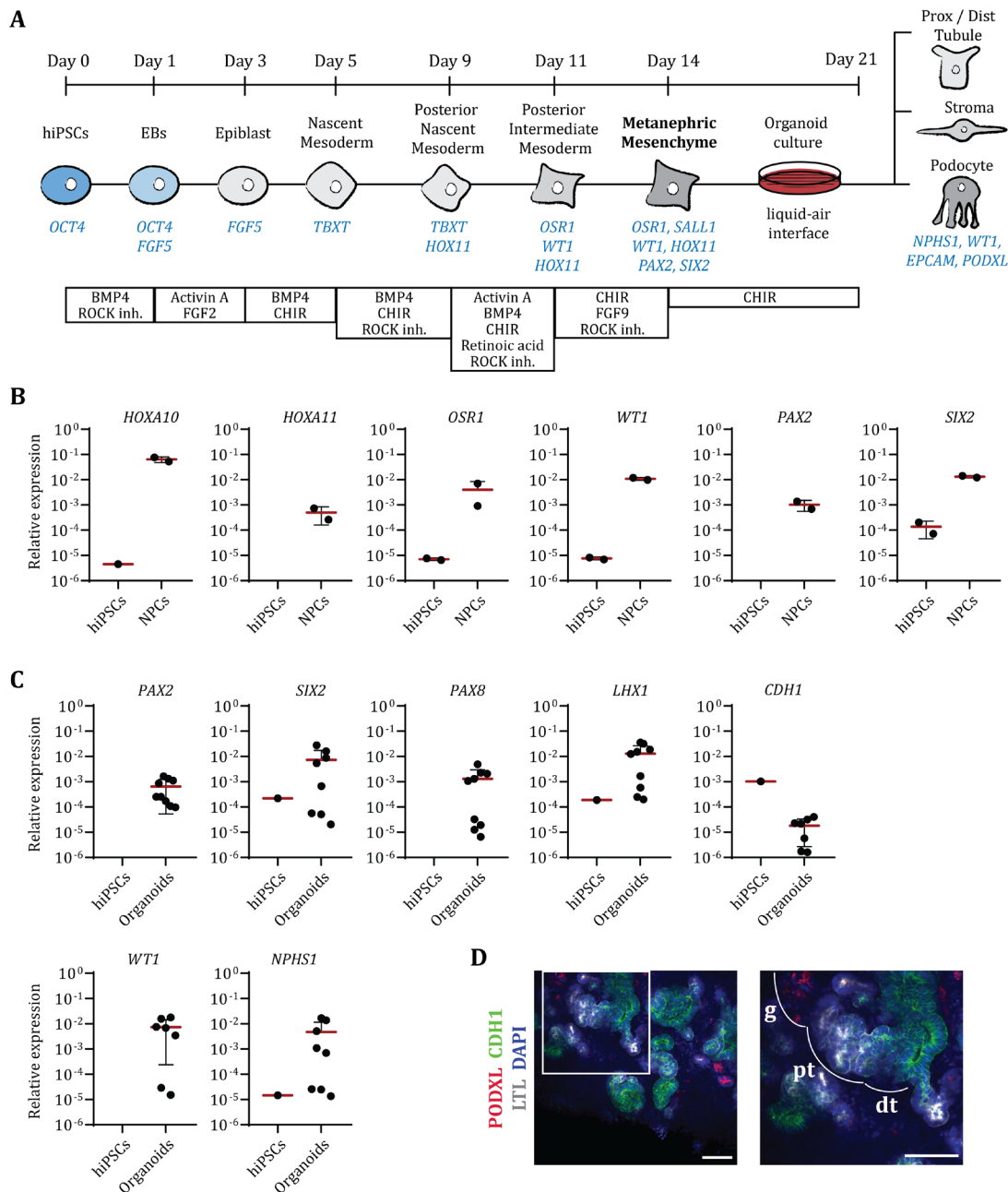


Figure 2. Kidney organoid differentiation according to the Taguchi/Brown protocol.

A: Overview of the protocol adapted from Taguchi et al., 2014 and Brown et al., 2015.

see Methods and List of materials for detailed culture medium and concentrations of growth factors; ROCK inh. = rho-associated protein kinase (ROCK) inhibitor; prox = proximal; dist = distal;

B: qPCR analysis of selected marker genes in hiPSCs and NPCs, shown as relative expression to *GAPDH*. Data is derived from n=2 independent differentiations and presented as mean +/- standard deviation (SD).

C: qPCR analysis of selected marker genes in hiPSCs and d21 organoids, shown as relative expression to *GAPDH*. Data is derived from n=2 (hiPSCs) or n=9 (d21 organoids) independent differentiations and presented as mean +/- SD. Missing values for hiPSCs = below limit of detection

D: IF staining for the indicated markers in a representative wildtype d21 organoid.

Left: 20x image; right: zoom in showing correct arrangement of nephron elements. Scale bars: 100 μ m
g = glomerulus; pt = proximal tubule; dt = distal tubule

of the nephron. In addition, d21 organoids expressed *PAX8* and *LHX1*, which are first upregulated in renal vesicles and comma- or s-shaped bodies, and persisted into our d21 organoids. Notably, organoids still expressed *PAX2* and to variable degrees *SIX2*, which indicates that these organoids still contained undifferentiated NPCs.

We also confirmed the presence of mature kidney markers in our organoids by immunofluorescence (IF) staining (Fig. 2D). Indeed, we found PODXL-positive glomeruli, lotus tetragonolobus lectin (LTL)-positive proximal tubules, and CDH1-positive distal tubules. In fact, we found nephron parts to be arranged in correct physiological order (Fig. 2D, right). Notably, we also detected *SIX2*-positive cells in d21 organoids, which were, however, confined to unstructured areas of the organoids, consistent with the qPCR analysis (Fig. 2C, 3B no Dox).

In conclusion, we established a kidney organoid protocol that, via a *SIX2*-positive NPC stage, yields organoids with nephron-like structures as well as residual *SIX2*-positive cells. We therefore decided to use this system to introduce Wilms tumor-specific alterations.

3.1.2 Inducible overexpression of LIN28A in human kidney organoids

The LIN28 paralogs are well-known miRNA processing factors, and have been implicated in stem cell control and in several human cancers, including Wilms tumor (Tzialikas and Romer-Seibert, 2015; Viswanathan et al., 2009). In fact, in mice, inducible overexpression of murine and human LIN28 leads to Wilms tumor formation, which is reversible upon LIN28 withdrawal. Importantly, LIN28 induction has to occur as early as the intermediate mesoderm stage in order to induce a tumor, whereas induction at the MM stage does not result in tumor formation (Urbach et al., 2014). Since these stages are recapitulated in developing kidney organoids, we decided to overexpress LIN28 in this system in order to generate an *in vitro* model for Wilms tumor.

We stably integrated a doxycycline (Dox) inducible LIN28A construct into the ND5 hiPSC line and selected single clones, which showed a robust induction of LIN28A upon Dox administration (not shown). We then differentiated our LIN28A clone and the parental line using the Taguchi/Brown protocol, and treated the corresponding EBs with Dox, starting at different time points (Fig. 3A). As expected, treatment with Dox did not affect organoid formation in the ND5 parental line and we obtained nicely structured organoids for nearly all EBs (not shown). Likewise, untreated EBs of our LIN28A line generated organoids that were mostly structured (Fig. 3B), and the same was true for LIN28A induction from d14 onwards (not shown), which marks the start of the organoid culture. However, expression of LIN28A starting at earlier time points, from d7, d9 or d11, resulted in organoids that were only partially structured or not structured at all (Fig. 3B).

In order to take a closer look at these organoids, we performed whole-mount IF staining and imaged the organoids at 4x magnification for overview and at 20x for more detailed images using a Yokogawa screening microscope (Fig. 3C). We stained for the mature proximal tubule marker LTL, the epithelial and distal tubule marker CDH1 as well as the nephron progenitor marker SIX2. Both, our Dox-treated parental ND5 lines (not shown) and untreated LIN28A organoids displayed CDH1-expressing distal tubular elements as well as LTL-positive proximal tubules, pointing to the successful generation of structured kidney organoids. We also observed SIX2-positive cells, which were, however, strictly confined to unstructured areas within the otherwise nicely structured organoids. In organoids treated with Dox from d7, d9 and d11 on, we found larger unstructured SIX2-positive areas, and if there were residual structures present, those stained positive for CDH1 but not for LTL (Fig. 3C). This indicates that early inducible overexpression of LIN28A disturbed kidney organoid differentiation.

During our experiments, however, we observed a considerable degree of heterogeneity at different levels of the system: (1) Within single wildtype/control organoids, we found areas that were nicely structured, and areas that were not structured at all (Fig. 3D, left). This is consistent with the observation that only around 60% of cells at d14 were NPCs, as demonstrated by flow cytometry analysis of the NPC marker SIX2 (Fig. 3D, right). Consequently, only around 60% of cells in a given EB have the potential to differentiate into kidney structures. (2) Organoids within the same Dox-treatment condition in a given experiment differed in the ratio of structured and unstructured parts. The same held true for organoids derived from independent LIN28A-expressing clones. (3) It proved particularly difficult to compare results between independent experiments.

In order to summarize our results, we classified ND5 parental and LIN28A organoids that were either untreated or treated with Dox at different time points, as structured, partially structured or unstructured based on their morphology (Fig. 3E). It was evident that also wildtype ND5 or un-induced LIN28A organoids occasionally failed to develop properly. However, we observed a trend towards fewer structures upon LIN28A overexpression from d7, d9 and d11 on, compared to the no Dox control. Nevertheless, a great fraction of these organoids was partially structured.

Therefore, we concluded that LIN28A overexpression indeed disturbed kidney organoid differentiation, albeit in a heterogeneous fashion, resulting in less structured organoids with considerable amounts of SIX2-positive cells. This is in agreement with the most prominent features of Wilms tumors which are a loss of (mature) kidney structures with a concomitant retention of blastemal cells that express SIX2. Since we observed residual SIX2-positive cells as well as unstructured parts also in our untreated organoids, the background against which phenotypic changes needed to be evaluated was already very noisy.

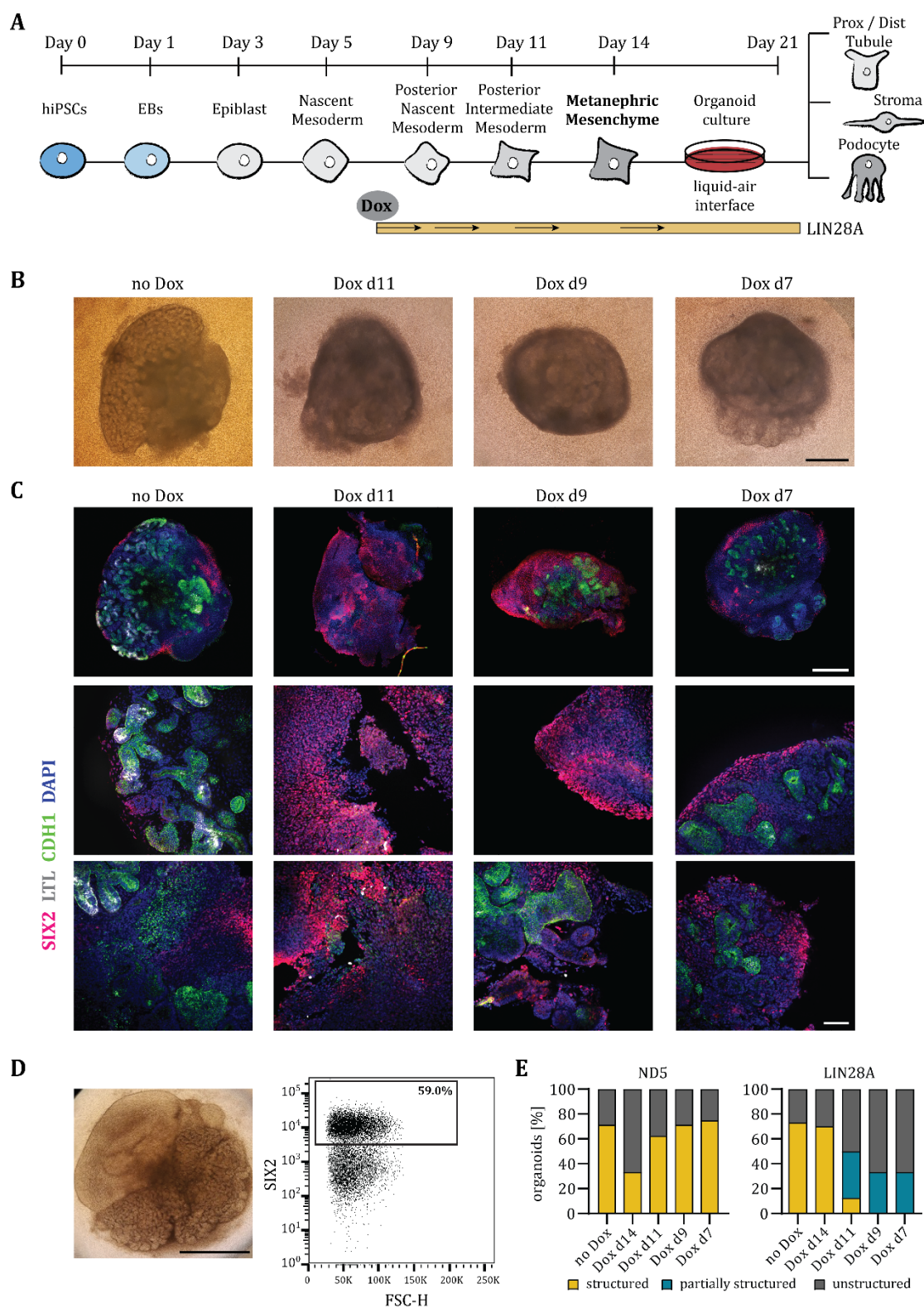


Figure 3. LIN28A overexpression induces a Wilms tumor-like phenotype in kidney organoids.

A: Schematic of the protocol and time points of LIN28A induction. Prox = proximal; Dist = distal

B: Brightfield images of d21 organoids which were either un-induced (no Dox) or were induced to overexpress LIN28A starting at the indicated time points. Scale bar: 500 μ m

C: Whole-mount IF staining of d21 organoids that were untreated (no Dox) or treated with Dox starting from the indicated time points. Top: 4x overview image; scale bar: 500 μ m. Middle and bottom: 20x images; scale bar: 100 μ m

D: Left: Brightfield image of a representative d21 organoid of the ND5 parental line; scale bar: 500 μm . Right: representative flow cytometry analysis of SIX2 in d14 NPCs of the ND5 parental line; FSC-H = Forward Scatter-Height

E: Percentage of structured, partially structured and unstructured d21 organoids of the ND5 parental line and the LIN28A oncogene line, dependent on treatment with Dox. Data is collected from n=5 independent differentiation experiments.

Note that time points are arranged according to increasing duration of treatment with Dox.

We considered this particularly problematic with respect to additional analyses like RNA-seq and functional studies, which would require a steeper signal-to-noise ratio. In addition, generation of organoids from single EBs in a liquid-air-interface system presented as very cumbersome and not suitable for experiments that required higher throughput. Therefore, we decided to turn to a different protocol that promised easier handling and to overcome many of the issues related to organoid maturity and heterogeneity.

3.2 Generation of kidney organoids using the protocol developed by Morizane et al.

We decided to adopt a different kidney organoid protocol (=Morizane protocol), which recapitulates embryonic development at a slightly different pace than the Taguchi/Brown protocol (Fig. 4A) (Morizane and Bonventre, 2017b; Morizane et al., 2015). In addition, we switched to a new hiPSC line, WT29, which had worked well using this protocol in the past (R. Ungricht, personal communication).

As before, the protocol comprises two distinct stages. Here, differentiation of iPSCs into NPCs occurs in a monolayer format by sequential activation of WNT, Activin and FGF signaling (Fig. 4A/B). After nine days, NPCs are detached from the cell culture dish and plated into U-bottom ultra-low attachment plates to allow for 3D aggregate formation (Fig. 4B). A 24-hour (h) pulse of WNT pathway activation and five days of FGF9 treatment induce the NPCs to differentiate further into tubular and glomerular cells. Afterwards, organoids are cultured in growth-factor-free conditions until they are harvested. Dissociating NPCs at d9 introduces a breakpoint into the protocol which also allows surplus NPCs to be frozen and stored for additional experiments using the same batch of NPCs. Compared to the previous protocol, this method offers easier handling, higher throughput and the generation of more homogeneous organoids which all stem from the same NPC pool and not from separate EBs. Culturing organoids in 96-well plates also offers the opportunity to record their growth using a time-lapse microscope (Fig. 4C). Organoids grow most within the first 10 days of the organoid culture. While growth is rather homogeneous within organoids of the same experiment as shown by small error bars, it can vary quite profoundly across different experiments.

In order to characterize the new organoid system, we performed a gene expression time course, covering markers known to be expressed at different steps during the differentiation protocol (Fig. 4D). In addition, we performed IF staining of organoids harvested at three different time points (Fig. 5A). iPSCs expressed the stem cell marker *NANOG*, which was rapidly downregulated as soon as cells transited through a mesoderm stage as shown by upregulation of *TBXT* (Brachyury) at d2 and d4 (Fig. 4D). Subsequently, starting at d4, cells acquired expression of the posterior Hox gene *HOXA11* that stayed upregulated throughout the differentiation process until d28. At d7, cells started to express *OSR1*, *PAX2* and *WT1*, which are characteristic for posterior intermediate mesoderm as well as the nephron progenitor-containing MM. While *OSR1* was downregulated at d11, *PAX2* stayed up until late organoid stages. Starting at d7, we could also detect expression of *SIX2*, the *bona fide* NPC marker, which was downregulated towards d11, when NPCs undergo MET and progress further towards more mature cell types of the kidney. This coincided with an upregulation of *LHX1*, typically expressed in renal vesicles and comma- or s-shaped bodies, as well as *CDH1*, which is expressed in epithelia and later marks distal tubules. Both *LHX1* and *CDH1* continued to be expressed in d21 and d28 organoids. In addition, other mature organoid markers, including *NPHS1*, *PODXL* and *SLC12A1*, a solute carrier that is specific to loop of Henle cells, started to be expressed at d14 or d18, respectively. *WT1* was expressed throughout kidney organoid differentiation after its acquisition at d7 and persisted until the final organoid stage as well, where it is expressed in glomerular podocytes.

In order to get a spatial overview, we performed IF staining on d14, d18 and d21 organoids as the endpoint of most of our future experiments (Fig. 5A). The overall structure of organoids can best be visualized using the glomerular marker *PODXL*, the proximal tubule marker *LTL*, as well as *CDH1*, which is confined to distal tubules. In agreement with our gene expression data, we detected *CDH1* staining already at d14. In contrast, there were only very few *PODXL*-positive cells which not yet assembled into glomeruli, and *LTL* staining was largely absent. At d18 and d21, however, both glomeruli and *LTL*-positive structures emerged and gave rise to the normal, mature organoid architecture.

Staining for *EPCAM* is useful to visualize all epithelial cells from proximal to distal tubule and is particularly helpful to provide structural information when combined with more restricted or nuclear markers. In combination with the glomerular markers *NPHS1* or *WT1* for example, this captures the entire nephron. All three markers, *NPHS1*, *WT1* and *EPCAM*, were already present at d14. At this stage, however, *EPCAM* staining overlapped with both *WT1* and *NPHS1*, pointing to an incomplete separation of future epithelia and glomeruli. At d18 and d21, we could clearly detect separated glomerular structures that expressed *WT1* or *NPHS1* in the nucleus or on the membrane, respectively, as well as tubules, which were positive for *EPCAM*.

Results

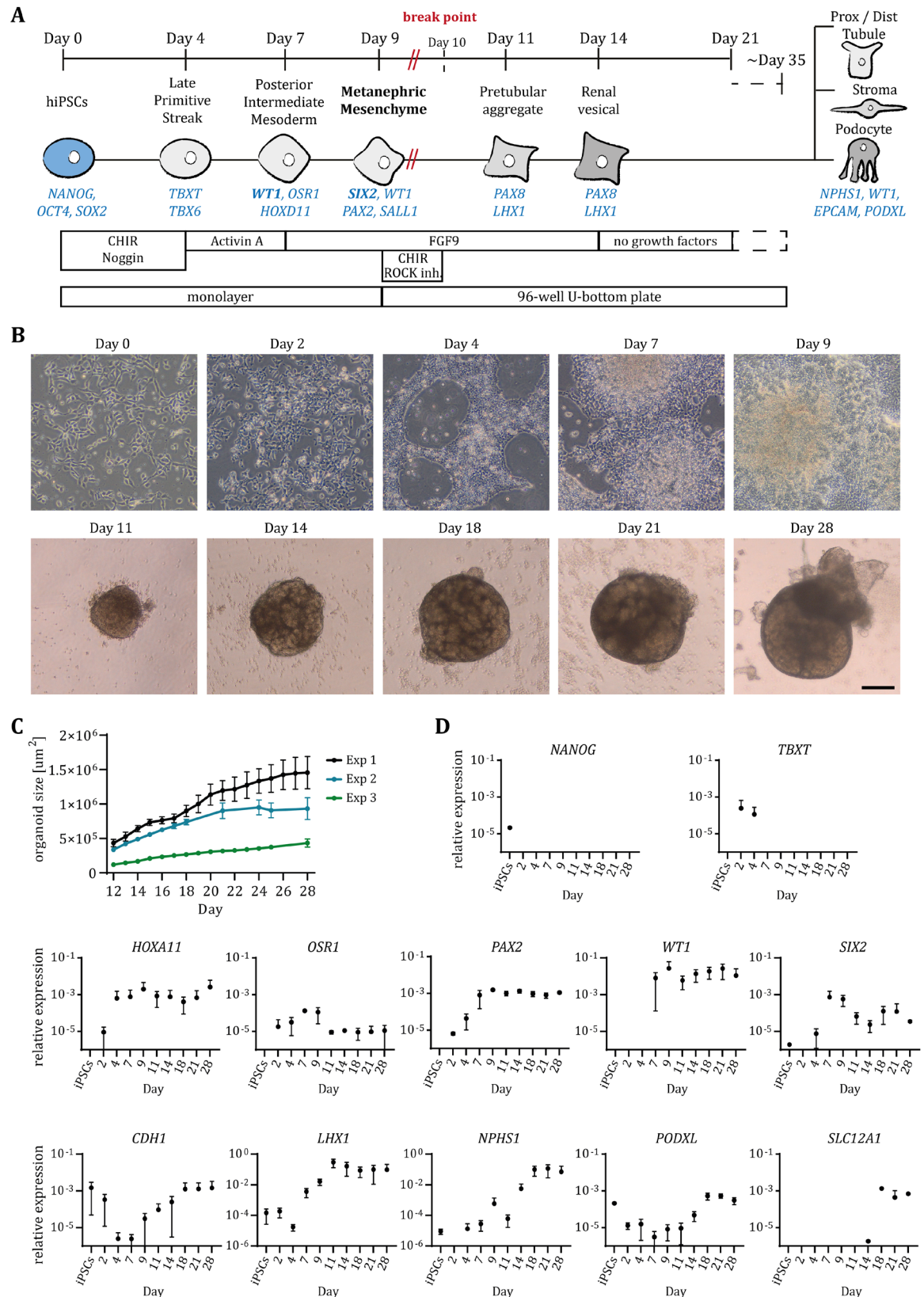


Figure 4. Kidney organoid differentiation according to the Morizane protocol.

A: Overview of the protocol adapted from Morizane et al., 2015; Prox = proximal; Dist = distal

B: Morphology of 2D monolayer and 3D organoid culture over time in brightfield images. Scale bar: 500 μm

C: Growth of wildtype organoids during organoid culture (d12-28) based on images acquired on an Incucyte® microscope (see Methods). Values in μm^2 are derived from three independent differentiation experiments with a minimum of $n=50$, $n=6$ and $n=14$ (at d28) organoids, and are presented as mean \pm SD. Note different starting cell numbers for Exp 1 and 2 (=50,000 cells/well) and Exp 3 (=25,000 cells/well). Exp = experiment

D: qPCR analysis of selected genes at different time points during organoid differentiation, shown as relative expression to *GAPDH*. Data from $n=2$ independent experiments is presented as mean \pm SD.

Interestingly, nephron structures appeared less densely packed in d21 organoids compared to earlier time points, and gaps between glomeruli or tubules were filled with stromal cells (not stained here).

In addition to markers that label mature kidney structures, we also stained for LHX1 and PAX8, which are expressed from the renal vesicle stage onwards (Fig. 5A). Notably, we detected both LHX1 and PAX8 in tubular and glomerular structures of d21 organoids, which is in agreement with our qPCR data (Fig. 4D and not shown). This indicates that those structures still possess an immature character. We found similar patterns for HOXA11 and PAX2 staining (not shown).

In order to confirm that nephron progenitors differentiated properly, we stained for the NPC marker SIX2. Indeed, SIX2 was absent from kidney organoids already at d14. Very rarely, single SIX2-positive cells could be observed outside of kidney structures. As a more functional parameter, we assessed proliferation by staining for Ki-67. Interestingly, we found the highest fraction of Ki-67-positive cells at d14, lower levels at d18 and the least at d21.

While IF staining is the most comprehensive method of assessing organoid structure, presence of progenitor cells and proliferation, a faster and more quantitative readout of these features is flow cytometry (Fig. 5B). For this, we dissociated d21 organoids and stained for selected markers.

We combined the tubular marker EPCAM with the glomerular marker WT1 to measure the presence of those nephron elements. We detected EPCAM-positive epithelial cells, WT1-positive glomerular cells, as well as EPCAM-WT1 double-positive cells, likely representing cells of the glomerular Bowman capsule (Fig. 5B, left) (Bariety et al., 2006). In addition, we selected SIX2 and Ki-67 staining to detect residual NPCs and to quantify proliferating cells, respectively. In agreement with the IF staining results, we found a fraction of Ki-67-positive but no SIX2-positive cells in d21 organoids.

Quantification of such markers by flow cytometry is therefore a useful tool to characterize kidney organoids and potential Wilms tumor phenotypes. For the latter, we would expect a loss of mature kidney structures, maintenance of SIX2-expressing progenitor cells, as well as an increase in proliferation or growth.

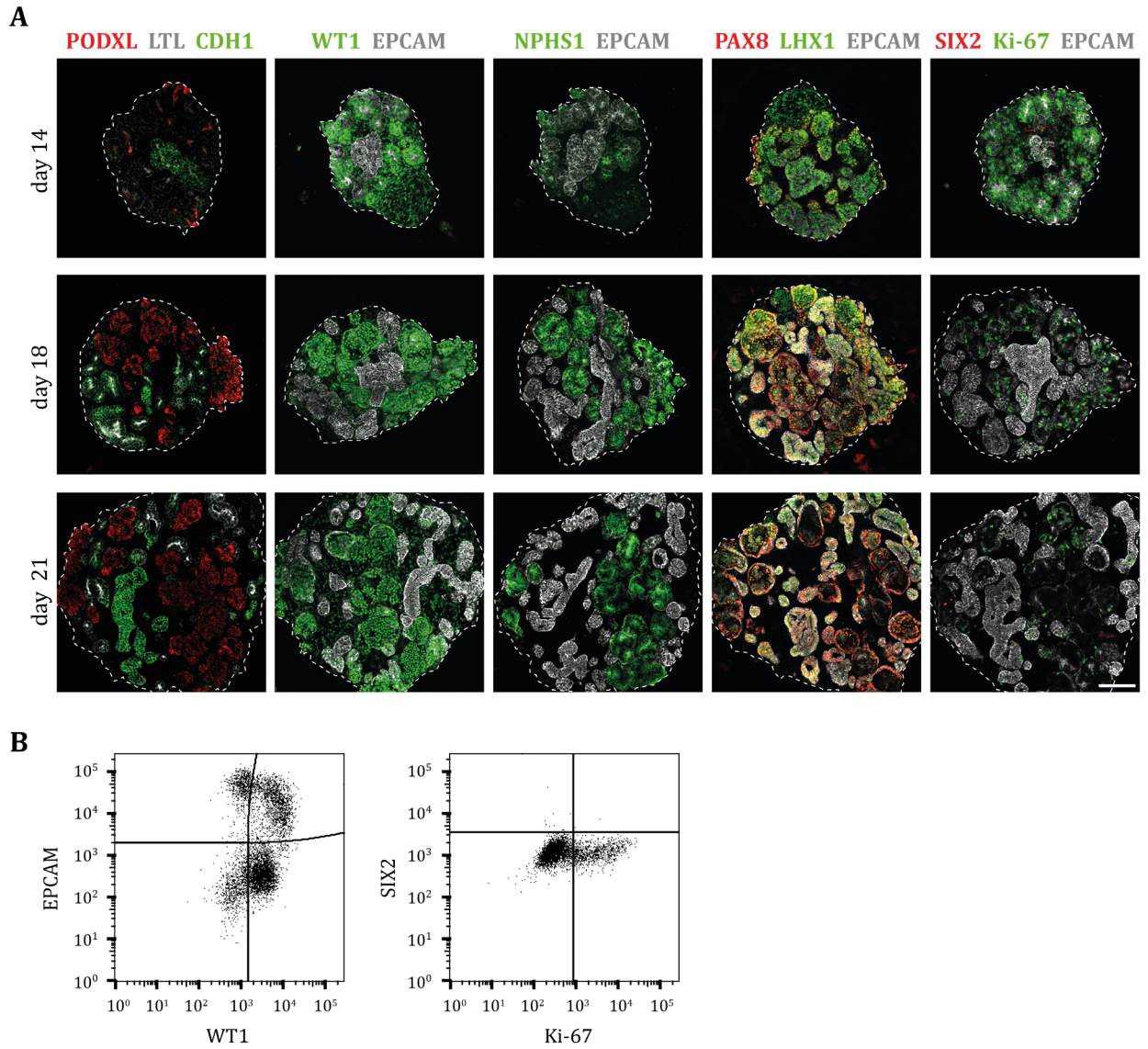


Figure 5. Image- and flow cytometry-based characterization of kidney organoids.

A: IF staining of the indicated markers at d14, d18 and d21 of organoid culture. Scale bar: 100 μ m

B: Representative flow cytometry analysis of pooled d21 wildtype organoids.

3.3 Overexpression of Wilms tumor oncogenes in kidney organoids - Morizane protocol

3.3.1 Generating new Wilms tumor oncogene cell lines

Having established the new kidney organoid protocol, we decided to follow up on the LIN28A phenotype that we observed using the Taguchi/Brown protocol (Section 3.1.2). We decided to generate new Dox-inducible cell lines in the WT29 cell line background and to expand our repertoire of Wilms tumor oncogenes: In addition to LIN28A we included its paralog LIN28B, wildtype SIX2 and SIX2 Q177R, a point-mutated SIX2 variant that had been identified in Wilms tumor patient samples (Walz et al., 2015; Wegert et al., 2015).

We reasoned that it would be helpful to control for the induction of our oncogenes in real time without having to stain for the actual proteins. Therefore, we generated vectors containing a Dox-inducible promoter that controls a mCherry sequence followed by a T2A signal and the coding sequence of either LIN28A, LIN28B, SIX2 or SIX2 Q177R. Like this, we obtained inducible mCherry-T2A-LIN28A, mCherry-T2A-LIN28B, mCherry-T2A-SIX2 and mCherry-T2A-SIX2 Q177R lines, from here on referred to as LIN28A, LIN28B, SIX2 and SIX2 Q177R lines or overexpression, or collectively as oncogenes (Fig. 6A).

We stably integrated these inducible mCherry-T2A-oncogene constructs into WT29 cells and selected for integration. Upon treatment with Dox, both, mCherry and the respective oncogene are transcribed into a single mRNA, which is then translated into two separate proteins. Consequently, the expression of the Wilms tumor oncogene correlates with mCherry fluorescence, which can be detected in real time by fluorescence microscopy during cell culture, by flow cytometry of live or fixed cells, and by confocal microscopy of cryosections in combination with IF staining.

In contrast to the previous experiments, we decided to use bulk/polyclonal cell lines instead of clonal lines derived from single cells. When we induced expression of the mCherry-T2A-oncogene constructs by treating iPSCs with Dox for 48 h and assessed mCherry induction via flow cytometry, we observed a very broad induction of mCherry that spanned several magnitudes of signal intensity. In addition, a fraction of cells did not induce mCherry at all (not shown). Therefore, of each line, we collected a fraction of cells with a medium-high mCherry signal via fluorescence-activated cell sorting (FACS). These cell populations were indistinguishable from control iPSCs, did not express mCherry in the absence of Dox, and showed a uniform mCherry peak upon treatment with Dox for 48 h (Fig. 6B). Of note, mCherry, and thus oncogene induction was weakest for LIN28B.

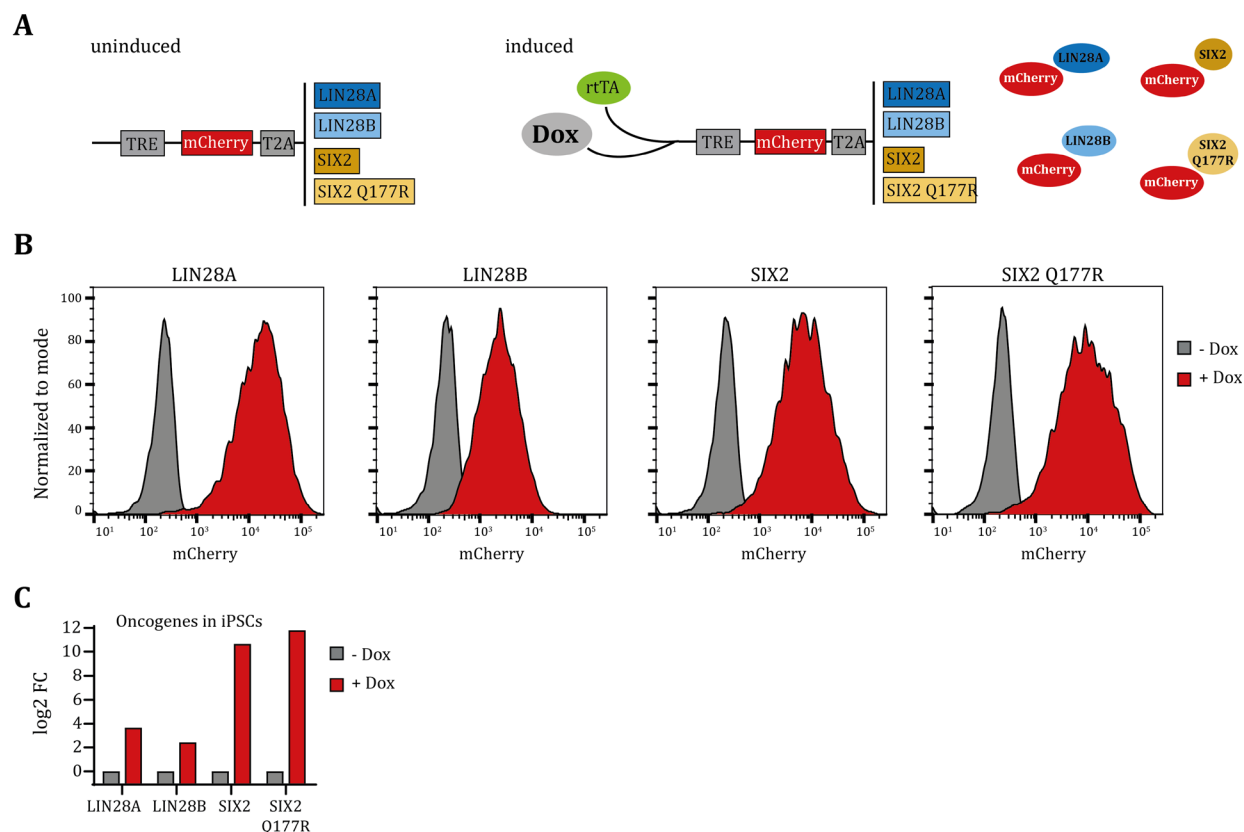


Figure 6. Generation of hiPSC lines with Dox-inducible Wilms tumor oncogenes.

A: Left: Schematic of oncogene constructs that were transfected into ND5 cells in order to generate mCherry-T2A-LIN28A (=LIN28A), mCherry-T2A-LIN28B (=LIN28B), mCherry-T2A-SIX2 (=SIX2) and mCherry-T2A-SIX2 Q177R (=SIX2 Q177R) iPSC lines; Right: relationship between mCherry signal and oncogene expression; TRE = tetracycline response element; rtTA = reverse tetracycline transactivator

B: Flow cytometry analysis of mCherry in LIN28A, LIN28B, SIX2 and SIX2 Q177R iPSC lines after purification by FACS, in untreated cells (-Dox) or after treatment with Dox for 48 h (+Dox).

C: qPCR analysis of oncogene expression in the indicated iPSC lines in untreated cells (-Dox) or after treatment with Dox for 48 h (+Dox). Data is presented as log₂ fold change (FC) in expression normalized to *GAPDH* and to the untreated control ($\Delta\Delta C_t$ method). Samples correspond to flow cytometry data in **B**.

In addition, we performed qPCR for LIN28A, LIN28B as well as SIX2 on these samples (Fig. 6C). In agreement with the mCherry flow cytometry results, we observed a strong induction of oncogenes upon treatment with Dox, compared to the respective untreated controls. Notably, SIX2 inductions were much more pronounced than those of LIN28A and LIN28B. In fact, *LIN28A* and *LIN28B* but not *SIX2*, are endogenously expressed in hiPSCs resulting in a smaller difference of their expression between induced and un-induced cells, as our qPCR probes do not discriminate between endogenous and transgenic mRNAs.

We therefore concluded that our newly generated Wilms tumor oncogene cell lines robustly induce the respective oncogenes upon treatment with Dox, and that mCherry fluorescence reports induction.

3.3.2 Characterization of Wilms tumor oncogene overexpression phenotypes

Next, we differentiated our newly generated cell lines into kidney organoids using the Morizane protocol. We knew from our previous results on LIN28A (Section 3.1.2) and experiments in mice (Urbach et al., 2014), that LIN28 needs to be induced before the NPC stage for a Wilms tumor phenotype to arise. Therefore, we started to induce LIN28A and LIN28B overexpression at d4, d7 and d9, and SIX2 and SIX2 Q177R overexpression at d7 and d9, which is before and at the time when SIX2 is normally expressed (Fig. 7A). In addition, we included untreated no Dox controls. We harvested organoids at d21 to characterize them via IF staining and flow cytometry.

As expected, we obtained nicely structured organoids for all untreated no Dox controls. These organoids contained EPCAM-positive tubular structures, as well as WT1-positive glomeruli (Fig. 7B no Dox). When we induced LIN28A and LIN28B overexpression starting at d7 and d9, organoids appeared unaffected and we found EPCAM-positive tubules and WT1-positive glomeruli similar to the untreated control (Fig. 7B). In contrast, overexpression from d4 yielded smaller organoids that contained only few EPCAM or WT1-positive nephron structures. We observed a very similar phenotype, when we induced SIX2 and SIX2 Q177R from d7 on and to a lesser extent upon induction from d9. Notably, the unstructured parts of affected d4 (LIN28) and d7 (SIX2) organoids stained weakly for WT1. Consistent with this, flow cytometry of these organoids revealed that the fractions of WT1-positive cells were barely diminished (Fig. 7C). In contrast, we detected a pronounced reduction in EPCAM as well as WT1-EPCAM double-positive cells that correspond to epithelia and encapsulated glomerular cells, respectively. In SIX2 Q177R Dox d7 organoids, however, WT1-EPCAM appeared unchanged. Induction of LIN28A and LIN28B from d7 and d9 as well as SIX2 and SIX2 Q177R from d9 resulted only in minor changes of WT1 and EPCAM in d21 organoids that can be ascribed to variability inherent to the organoid system (Fig. 7C).

We next assessed the presence of LTL-positive proximal tubules, SIX2-expressing nephron progenitors as well as Ki-67-positive proliferating cells (Fig. 8A; 9A). Both the maintenance of SIX2-positive cells and an increase in proliferation would support the induction of a Wilms tumor phenotype within the kidney organoid system.

Untreated organoids derived from all lines presented with LTL-positive proximal tubules and were devoid of SIX2 (Fig. 8A). Overexpression of LIN28A and LIN28B from d7 and d9 did not affect LTL-positive tubules and did not lead to a maintenance of SIX2-expressing cells. Interestingly, while LTL staining was reduced upon LIN28A or LIN28B overexpression from d4, this was not accompanied by a maintenance of SIX2. Consequently, we also did not detect any SIX2-expressing cells via flow cytometry in LIN28A or LIN28B overexpressing organoids (Fig. 8B). Together with a reduction of EPCAM and to a lesser extent of WT1, this points to a defect in

Results

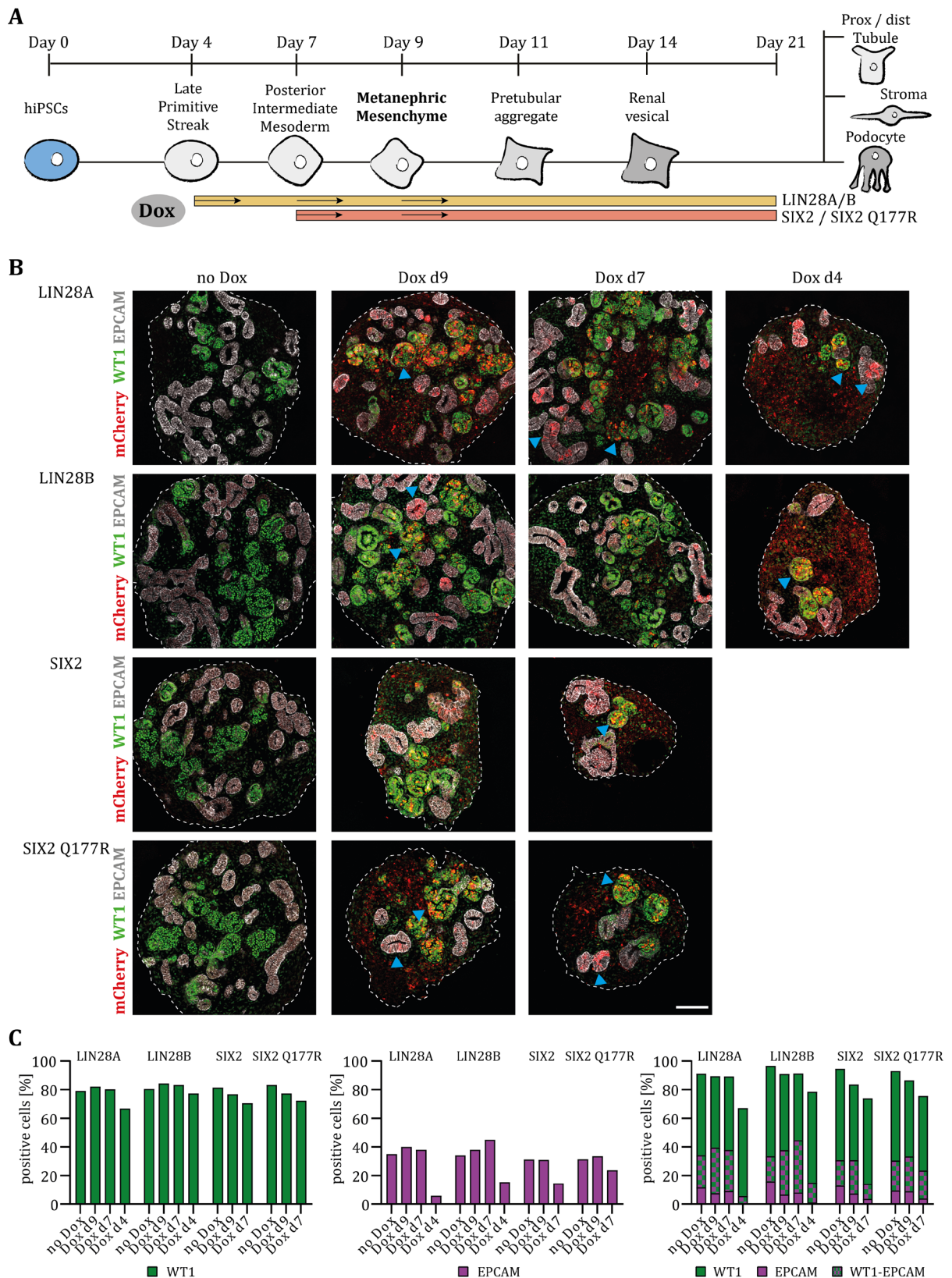


Figure 7. Early overexpression of Wilms tumor oncogenes impairs the development of mature kidney structures.

A: Experimental overview and induction of Wilms tumor oncogenes. Prox = proximal; Dist = distal

B: IF staining of WT1 and EPCAM in d21 organoids derived from the indicated Wilms tumor oncogene lines that were untreated (no Dox) or treated with Dox starting from the indicated time points. mCherry represents induction of the respective oncogene. Blue arrowheads show mCherry signal within WT1 or EPCAM-positive nephron structures. Scale bar: 100 μ m

C: Flow cytometry-based quantification of WT1 and EPCAM in pooled d21 organoids derived from untreated (no Dox) or Dox-treated Wilms tumor oncogene lines as in **B**. Data is shown as % of cells for one representative experiment.

Note that time points are arranged according to increasing duration of treatment with Dox.

kidney organoid formation which did not result from an inability of nephron progenitor cells to downregulate SIX2.

Since we induced SIX2 expression via Dox in the SIX2 and SIX2 Q177R lines and therefore expected the expression of this protein, it was difficult to deduce a differentiation defect from SIX2 staining. As for LIN28, untreated organoids displayed LTL-positive tubules and were devoid of SIX2. Induction of SIX2 and SIX2 Q177R from d9 did not obviously change the presence of LTL-positive tubules, whereas we found fewer LTL-positive tubules upon induction from d7. As expected, we found SIX2-positive cells in all Dox-treated organoids (Fig. 8A). In agreement with this, we detected between 25 and 40% of SIX2-positive cells upon SIX2 or SIX2 Q177R induction via flow cytometry (Fig. 8B). Notably, SIX2-positive cells were scattered within the organoids and did not grow in colonies. In order to determine whether SIX2 overexpression resulted in a maintenance of NPCs within the organoids, we also stained for SIX1, as an additional marker for NPCs. While SIX1-positive cells appeared to be more frequent upon Dox treatment, they often did not overlap with the mCherry reporter of SIX2 or SIX2 Q177R (not shown), which indicates that SIX2 overexpression did not result in a maintenance of NPCs. Even though this antibody has been described to stain SIX1 in human fetal kidney and to overlap to some extent with SIX2 (Lindström et al., 2018a), we did not test it in hiPSC-derived NPCs that should co-stain for both SIX2 and SIX1. Therefore, we cannot be certain that in our hands the antibody indeed labeled NPCs.

Ki-67-positive cells were present in all organoids, irrespective of oncogene induction. However, the fraction of Ki-67-positive cells appeared slightly increased in Dox treated organoids that were still well structured, including LIN28A and LIN28B Dox d7 and d9, as well as SIX2 and SIX2 Q177R Dox d9 organoids. This was true both in IF stainings and flow cytometry (Fig. 9A/B). Importantly, we found a reduced frequency of Ki-67-positive cells in organoids that showed fewer nephron structures upon oncogene induction, including LIN28A and LIN28B Dox d4 and SIX2 and SIX2 Q177R Dox d7 organoids. Of note, we detected a fraction of SIX2-Ki-67 double-positive cells upon induction of *SIX2* (Fig. 9B, right).

Collectively, these results suggest that early overexpression of Wilms tumor oncogenes led to a general differentiation defect that did not go in hand with maintenance of SIX2-expressing NPCs and increased proliferation, as would be expected from recapitulating Wilms tumorigenesis.

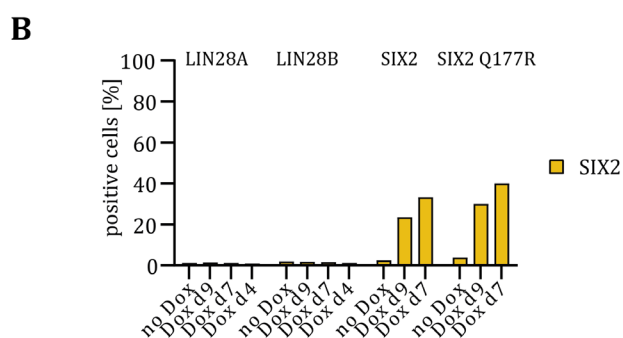
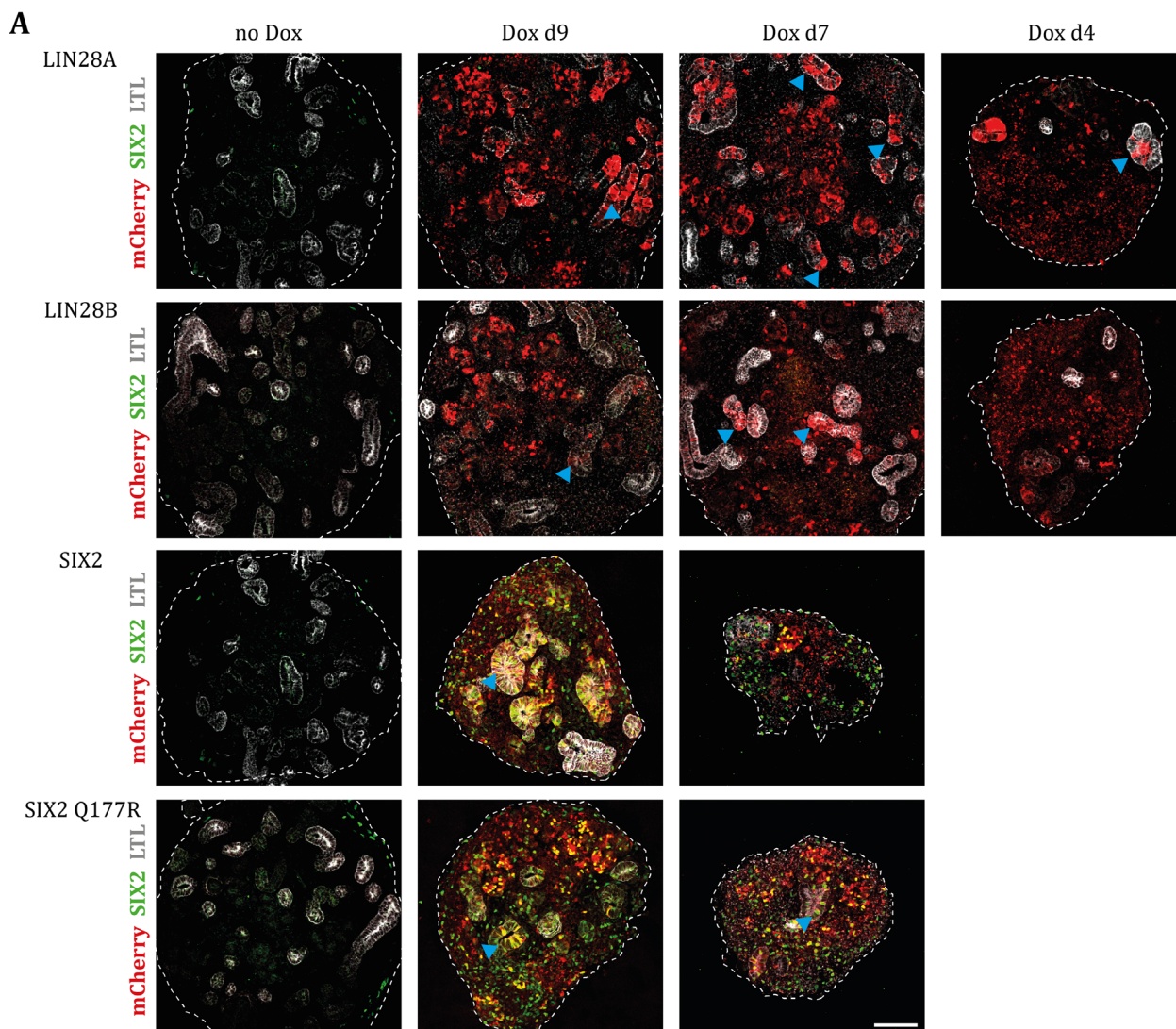


Figure 8: SIX2 expression is not maintained upon LIN28A or LIN28B overexpression.

A: IF staining of SIX2 and LTL in d21 organoids derived from the indicated Wilms tumor oncogene lines that were untreated (no Dox) or treated with Dox starting from the indicated time points. mCherry represents induction of the respective oncogene. Blue arrowheads show mCherry or SIX2 signal (for SIX2 and SIX2 Q177R) within LTL-positive nephron structures. Scale bar: 100 μm

B: Flow cytometry-based quantification of SIX2 in pooled d21 organoids derived from untreated (no Dox) or Dox-treated Wilms tumor oncogene lines as in A. Data is shown as % of cells for one representative experiment.

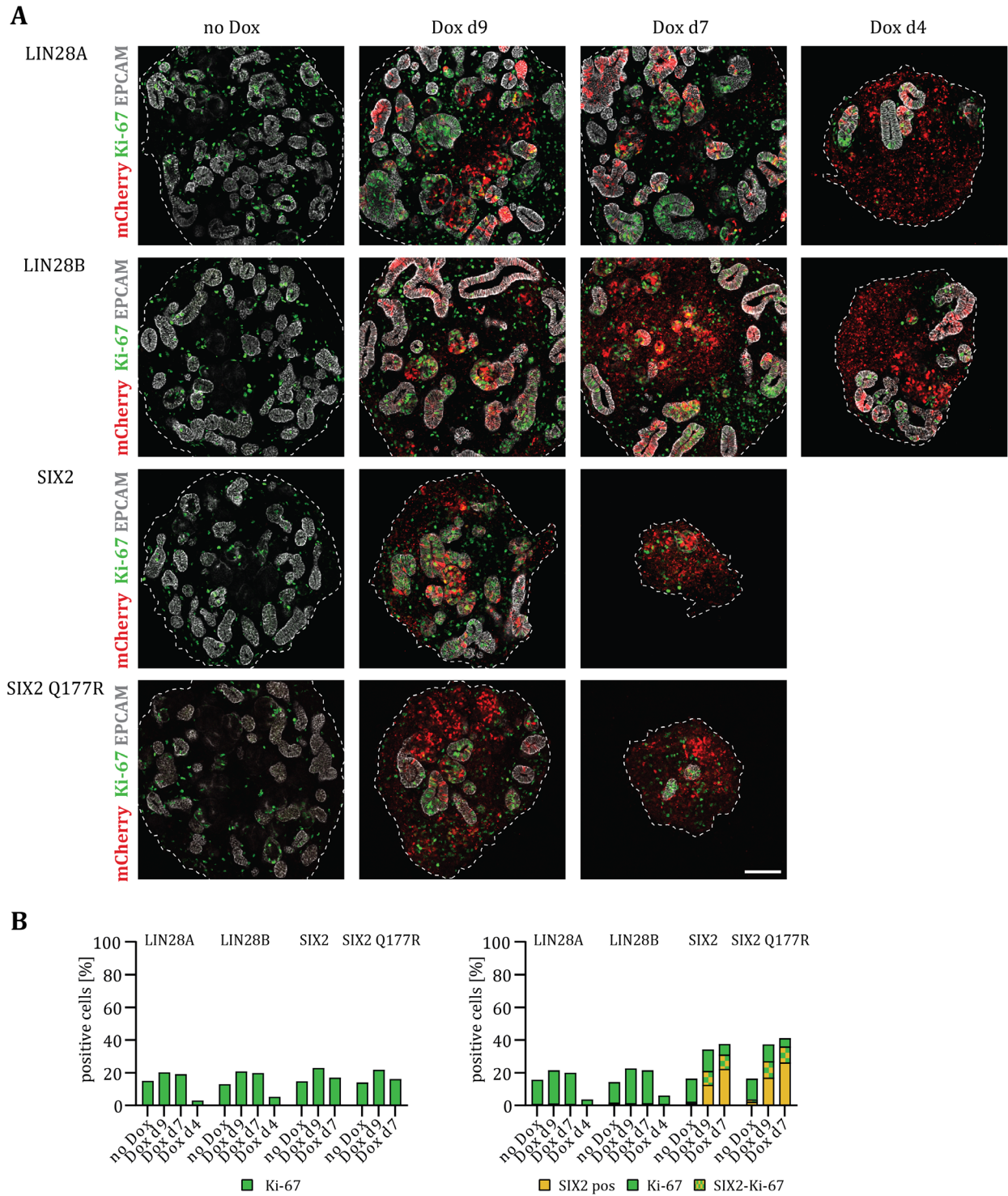


Figure 9. Proliferation is not elevated in Wilms tumor oncogene-expressing kidney organoids.

A: IF staining of Ki-67 and EPCAM in d21 organoids derived from the indicated Wilms tumor oncogene lines that were untreated (no Dox) or treated with Dox starting from the indicated time points. mCherry represents induction of the respective oncogene. Scale bar: 100 μ m

B: Flow cytometry-based quantification of Ki-67 and combined SIX2-Ki-67 in pooled d21 organoids derived from untreated (no Dox) or Dox-treated Wilms tumor oncogene lines as in A. Data is shown as % of cells for one representative experiment.

3.3.3 Additional observations

In order to confirm that our Wilms tumor oncogenes were actually induced, we took advantage of their co-expression with mCherry. Indeed, we found mCherry fluorescence in IF stainings of all Dox-treated organoids, indicating LIN28A, LIN28B, SIX2 and SIX2 Q177R induction under these conditions (Fig. 7B; 8A; 9A). We also stained for LIN28A and LIN28B proteins in the respective organoids and found an overlap between mCherry and LIN28A and LIN28B (Fig. 10A). The same held true for induction of SIX2 and SIX2 Q177R (Fig. 8A). More quantitatively, we measured mCherry in dissociated d21 organoids via flow cytometry and found it to be strongly induced (Fig. 10B). Notably, mCherry levels were highest in the LIN28A line upon Dox d4 treatment.

We also checked for mCherry induction in d9 NPCs, which is a relevant time point for the oncogenes to be effective. Indeed, mCherry was upregulated in all lines upon Dox treatment (Fig. 10C, top). As before, we observed the strongest mCherry signal in LIN28A cells induced from d4 on, while LIN28B induction as well as all inductions from d7 on were weaker. QPCR analysis of LIN28A, LIN28B and SIX2 confirmed their upregulation in d9 NPCs derived from Dox treated cells, compared to no Dox controls (Fig. 10D). Importantly, both mCherry and the respective oncogenes were not expressed in untreated d9 NPCs or d21 organoids (Fig. 10B/C, top and not shown).

Next, we wondered whether oncogene induction from d4 and d7 interfered with earlier differentiation steps. We reasoned that this might impede the specification of NPCs and therefore result in less cells being able to differentiate into mature kidney structures. To this end, we analyzed *SIX2* and *WT1* expression in d9 NPCs via qPCR and flow cytometry.

WT1 mRNA expression was slightly decreased in NPCs from all Dox induced lines, compared to the respective no Dox controls (Fig. 10E). However, *WT1* protein expression was not affected upon induction of SIX2 and SIX2 Q177R and was even elevated upon induction of LIN28A and LIN28B (not shown). Interestingly, we found *SIX2* expression to be reduced in Dox-treated NPCs of the LIN28A and LIN28B lines. This was particularly pronounced in the Dox d4 condition and was detectable on both the mRNA and the protein level (Fig. 10C, bottom; 10E). As expected, we found a strong induction of *SIX2* mRNA in SIX2 and SIX2 Q177R cells upon treatment with Dox, whereas *SIX2* protein levels did not appear to be elevated. This indicates that LIN28A and LIN28B induction from d4 on might interfere with proper NPC differentiation as shown via reduced *SIX2* expression in d9 NPCs. If induction of SIX2 and SIX2 Q177R similarly affected NPC specification requires assessing the expression of additional NPC markers.

Finally, we took a closer look at the mCherry signal in relation to structured parts of the organoids. Indeed, we found numerous EPCAM or LTL-positive tubules and *WT1*-positive glomerular arrangements that were strongly mCherry-positive (Fig. 7B; 8A, blue arrowheads).

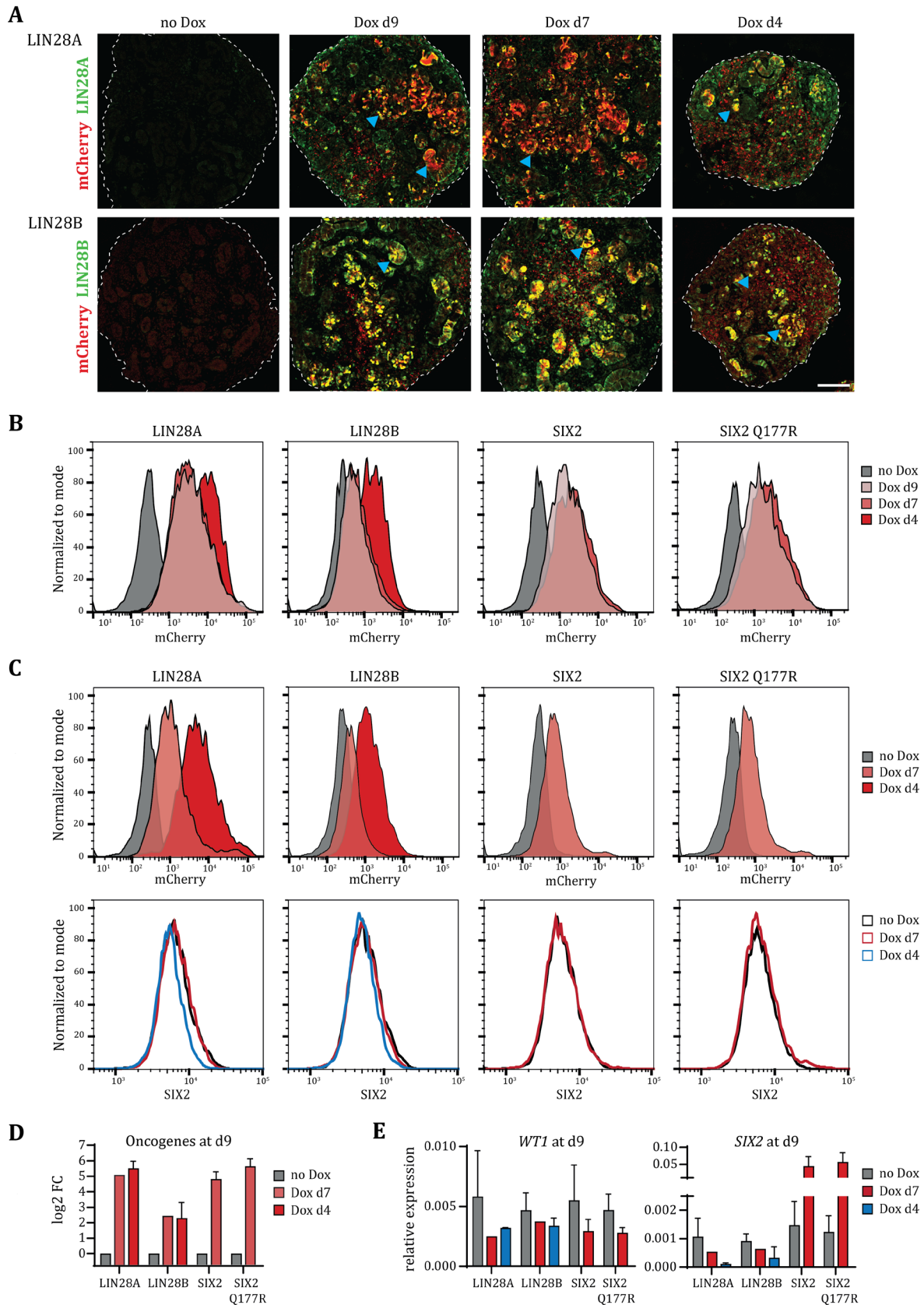


Figure 10. Wilms tumor oncogenes are induced in d21 organoids and d9 NPCs.

A: IF staining of LIN28A and LIN28B in d21 organoids derived from the indicated Wilms tumor oncogene lines that were untreated (no Dox) or treated with Dox starting from the indicated time points. mCherry represents induction of the respective oncogene. Blue arrowheads show mCherry and LIN28A/B signal within morphologically identified structures. Scale bar: 100 μ m

B: Flow cytometry analysis of mCherry in pooled d21 organoids derived from untreated (no Dox) or Dox-treated Wilms tumor oncogene lines as in **A**.

C: Flow cytometry analysis of mCherry (top) and SIX2 (bottom) in d9 NPCs derived from the indicated Wilms tumor oncogene lines that were untreated (no Dox) or treated with Dox starting from the indicated time points. Note that flow cytometry in **B** and **C** was performed at different times, and differing mCherry levels in untreated (no Dox) cell populations reflect changes in laser performance at the respective days.

D: qPCR analysis of oncogene expression in d9 NPCs derived from cell lines and conditions as in **C**. Data is presented as log₂ FC in expression normalized to *GAPDH* and to the untreated control ($\Delta\Delta\text{Ct}$ method). Data is shown as mean \pm SD. LIN28A: n=2 no Dox, Dox d4, n=1 Dox d7; LIN28B: n=3 no Dox, Dox d4, n=1 Dox d7; SIX2 and SIX2 Q177R: n=3 no Dox, Dox d7. Samples correspond to flow cytometry data in **C** (top).

E: qPCR analysis of *WT1* (left) and *SIX2* (right) expression in d9 NPCs derived from the same samples as in **D**. Data is presented as expression relative to *GAPDH* and shown as mean \pm SD. *SIX2* expression corresponds to *SIX2* flow cytometry data in **C** (bottom).

More specifically, we also detected actual SIX2, LIN28A and LIN28B protein staining in these structures (Fig. 8A; 10A, blue arrowheads), demonstrating that overexpression of these proteins alone is not sufficient to block formation of mature nephron structures.

Taken everything together, we found a reduction of mature nephron structures upon early overexpression of LIN28A and LIN28B (Dox d4) as well as of SIX2 and SIX2 Q177R (Dox d7). However, this was not accompanied by a retention of SIX2 in these organoids or by an increase in proliferation. Expression of oncogenes within mature nephron structures showed that oncogene overexpression itself is not sufficient to inhibit differentiation. In contrast, a general impairment of differentiation as seen in these organoids might result from defects in NPC specification, which would have to be investigated further for definitive proof. These results contrast previous findings of LIN28A overexpression resulting in loss of mature structures and expansion of SIX2-expressing cells using the Taguchi/Brown protocol (Section 3.1.2).

3.4 Mimicking β -catenin stabilization by prolonged treatment of organoids with CHIR

One of the most frequently mutated genes in somatic cases of Wilms tumor is *CTNNB1*, which encodes β -catenin, the effector of canonical WNT signaling. In Wilms tumors, β -catenin is very commonly mutated at S45, which is an important target site for phosphorylation that induces its degradation (Amit et al., 2002). Mutations of β -catenin that affect S45 thus lead to its stabilization and accumulation in the nucleus, resulting in an overactivation of canonical WNT signaling (Koesters et al., 2003). WNT signaling plays very important roles in kidney development, during mesoderm specification, NPC maintenance in the MM, induction of MET, as well as proximal-distal nephron patterning (Lindström et al., 2015; Park et al., 2012). In cell culture, activation of WNT signaling can be achieved by treating cells with the GSK-3 β inhibitor CHIR, which prevents phosphorylation and subsequent degradation of β -catenin, allowing it to activate downstream targets. In our kidney organoid protocol, we apply CHIR between d0 and d4 to specify primitive streak, and from d9 to d10 as a 24 h pulse in order to induce NPCs to differentiate and to give rise to mature nephron structures.

In order to mimic continuous WNT pathway activation as caused by mutations in *CTNNB1*, we decided to prolong the 24 h CHIR pulse by culturing the developing organoids in the presence of different concentrations of CHIR from d10 until d21 (Fig. 11A). We observed a strong increase in organoid growth and dramatic morphological phenotypes, especially upon treatment with 0.5 μ M or 1 μ M CHIR (Fig. 11B/C). Organoids grew to huge aggregates that were composed of structured and unstructured areas next to one another. Interestingly, incubation with 3 μ M CHIR only mildly affected organoid size, but gave rise to abnormally shaped organoids, which seemed to lack any structures.

We performed flow cytometry of pooled d21 organoids to assess the observed morphological phenotypes in treated versus untreated organoids quantitatively (Fig. 11D). While untreated organoids contained around 70% WT1-positive cells, this fraction was strongly reduced to 40%, 10% and almost no WT1-positive cells, upon treatment with 0.5 μ M, 1 μ M and 3 μ M CHIR, respectively. Interestingly, incubation with 0.5 μ M CHIR did not affect the frequency of EPCAM-positive cells, whereas this fraction was again strongly diminished and completely lost upon 1 μ M and 3 μ M CHIR, respectively. Notably, we detected a small increase in SIX2- and Ki-67-positive cells, compared to untreated cells. Especially the fraction of SIX2-positive cells detected via flow cytometry varied profoundly between experiments, also in the untreated condition, which we ascribed to technical issues with flow cytometry and gating.

In order to assess organoid composition more closely, we performed IF staining on cryosections of d21 organoids (Fig. 11E). Consistent with the flow cytometry results, we observed a marked

Results

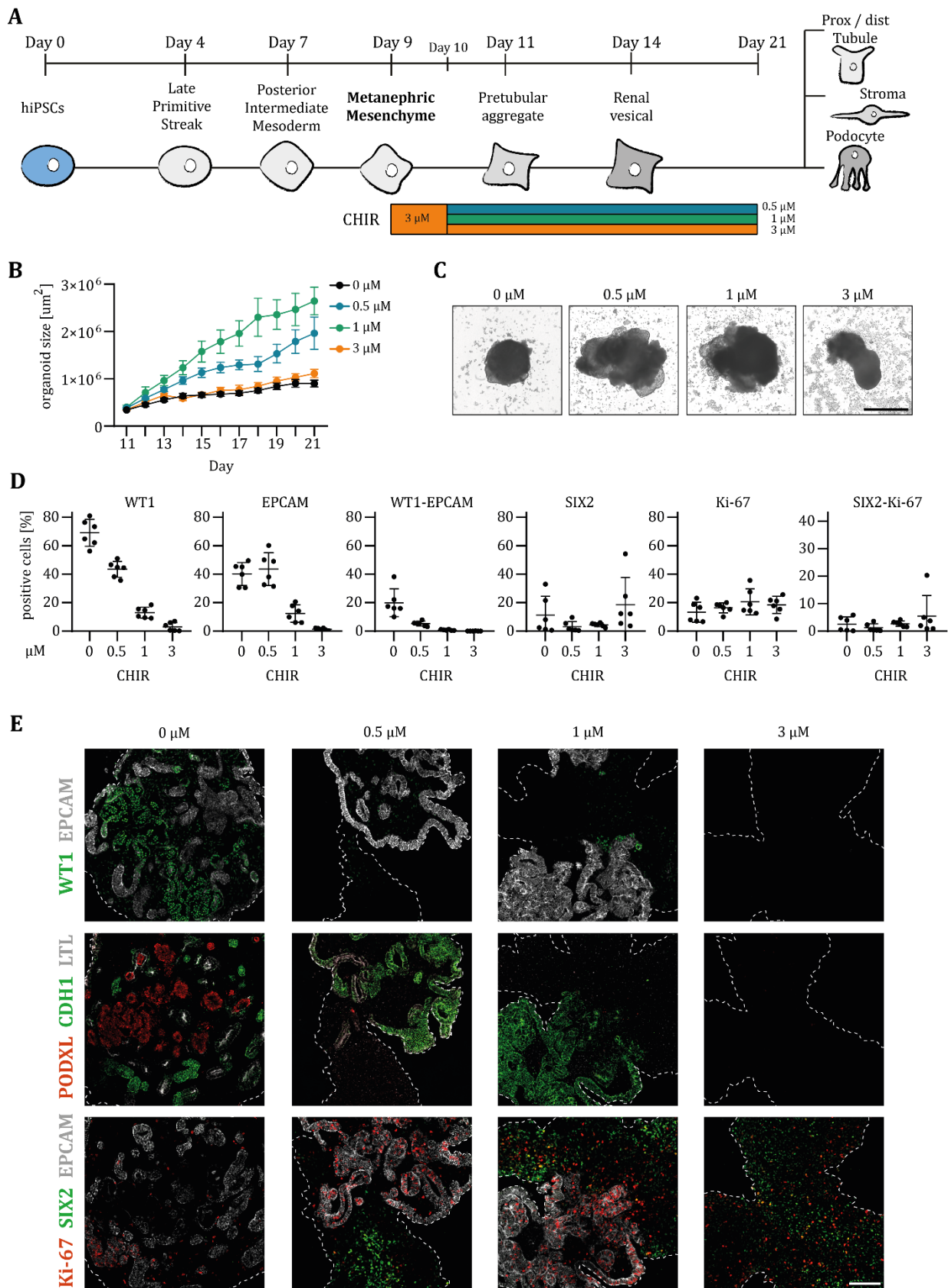


Figure 11. Prolonged activation of WNT signaling in kidney organoids disrupts differentiation.

A: Experimental outline of treatment with CHIR; Prox = proximal; Dist = distal

B: Growth of organoids between d11 and d21 that were treated with the indicated concentrations of CHIR. Values in μm^2 are derived from Incucyte® images (see Methods) and are presented as mean \pm SD for $n=12$ organoids from one representative experiment.

C: Morphology of representative d21 organoids that were treated with the indicated concentrations of CHIR. Brightfield images were acquired using an Incucyte® system. Scale bar: 1 mm

D: Flow cytometry-based quantification of indicated markers in pooled d21 organoids treated with the indicated concentrations of CHIR. Data is presented as individual data points with indicated mean \pm SD from $n=6$ independent experiments.

E: IF staining for the indicated markers in d21 organoids that were treated with the indicated concentrations of CHIR. Scale bar: 100 μm

reduction of WT1 at 0.5 μM and 1 μM CHIR and a complete absence at 3 μM CHIR. Residual WT1-positive cells formed very few PODXL-positive glomerular structures at 0.5 μM CHIR, while we only found scattered WT1-positive cells and no PODXL staining at all at 1 μM CHIR. Likewise, the proximal tubule marker LTL was completely lost at 1 μM and 3 μM CHIR, while there were few LTL-positive tubules left at 0.5 μM CHIR. In contrast, “early” and more general epithelial markers like CDH1 and EPCAM were still present in 0.5 μM and reduced in 1 μM CHIR-treated cells. Those epithelia, although appearing polarized, did not organize into the usual tubular structures, but rather presented as disorganized epithelial bulks, mostly confined to one side of the organoid. As already hinted above, incubation with 3 μM CHIR resulted in a complete loss of all epithelial structures and we therefore did not observe any CDH1 or EPCAM staining within these organoids. Importantly, we found a considerable fraction of SIX2-expressing cells in CHIR treated organoids, particularly at 3 μM CHIR, but not in untreated organoids. Notably, SIX2-expressing cells were confined to unstructured, EPCAM-negative parts of the organoids, and their frequency varied from one organoid to the other. Finally, we stained for Ki-67 as a marker for proliferation, and found it to be increased upon CHIR treatment both in structured and unstructured parts of the organoids.

Taken together, ectopic activation of β -catenin via CHIR treatment resulted in an induction of organoid growth, loss of proximal tubules and glomeruli, disorganization of distal epithelia, as well as persistence of SIX2-expressing cells. Interestingly, these effects appeared to be dose-dependent. Treatment with 3 μM CHIR abrogated all epithelial differentiation and maintained SIX2-positive cells, while treatment with 1 μM allowed epithelial differentiation in general, but prevented generation of most proximal elements including LTL-positive proximal tubules and WT1-expressing glomeruli. Treatment with 0.5 μM CHIR had similar effects, but we found residual LTL-positive proximal tubules and higher fractions of WT1-positive cells. Interestingly, most organoids had structured and unstructured parts, which indicates that, although uniformly supplied, CHIR availability differed in distinct regions of the organoids. Overall, mimicking β -catenin stabilization via treatment with CHIR partially inhibited nephron progenitor differentiation and disrupted kidney organoid development.

3.5 Inducible knockout of *WT1* in developing human kidney organoids

3.5.1 Generation of hiPSC lines with an inducible *WT1* knockout

Aside from oncogene overexpression and chemical manipulation of the WNT signaling pathway, we also decided to mimic the most famous Wilms tumor mutation, which is loss of *WT1*. *WT1* is expressed from the intermediate mesoderm on throughout kidney development until it becomes confined to glomerular podocytes both, *in vivo* and in corresponding stages of kidney organoids. To generate *WT1* knockout (KO) kidney organoids, we utilized a derivative of our WT29 hiPSC line that carries a Dox-inducible clustered regularly interspaced short palindromic repeats (CRISPR) associated protein 9 (Cas9) transgene (WT29-iCas9). We generated three cell lines by performing lentiviral transduction of three different guide RNAs (gRNAs) targeting the *WT1* gene. The gRNA vectors harbor a red fluorescent protein (RFP) sequence and a puromycin resistance gene, which allowed us to select for transduced cells (Fig. 12A). In these cell lines, Dox-mediated Cas9 expression results in the generation of DNA double-strand breaks within the *WT1* coding sequence, which, due to non-homologous end joining, can lead to frameshift mutations and eventually to premature STOP codons in the corresponding mRNA. It is important to consider that we did not derive clones from our Cas9-*WT1* gRNA lines, but instead worked with bulk populations. In addition, we induced *WT1* KO prior to differentiation, introducing some variability with respect to KO efficiency between experiments.

3.5.2 Phenotypic characterization of *WT1* KO organoids

In order to test the three gRNAs for *WT1* KO efficiency and phenotypic strength, we treated our inducible *WT1* KO lines with Dox for three days to induce *WT1* gene editing, and seeded cells for differentiation according to our standard protocol (Fig. 3A). For each gRNA, we differentiated *WT1* KO (KO^{iPSC}) cells and corresponding wildtype (= not-edited) cells.

At the d9 NPC stage, we collected samples for flow cytometry analysis of *WT1* and *SIX2* protein expression. *WT1* was expressed in 78.5%, 70.4% and 92.7% of not-edited NPCs derived from the respective gRNA cell lines (Fig. 12B). In NPCs derived from KO^{iPSC} cells, *WT1*-positive cell fractions were reduced to 16.1%, 43.4%, and 10.6%, respectively. This demonstrated KO of *WT1* in a large fraction of cells, which varied between the three different gRNAs. Considering the extent of *WT1* reduction compared to levels in corresponding not-edited NPCs, we obtained KO efficiencies of around 80%, 40% and 90% for gRNA1, 2 and 3, respectively, in this test. In addition, we also assessed *SIX2* expression and found a shift towards higher *SIX2* intensities in KO^{iPSC} NPCs compared to not-edited NPCs (Fig. 12C). This shift was most pronounced for gRNA3, and thus correlated with *WT1* KO efficiency.

Starting from d11, we recorded the size of the developing organoids over time and observed a reduced growth in KO^{iPSC} versus corresponding not-edited organoids, which was accompanied by visible signs of cell death (Fig. 12D and not shown). Again, we observed the strongest growth phenotypes for gRNA3 and gRNA1.

In order to further characterize our d21 organoids for potential differentiation defects, we applied flow cytometry analysis for WT1 and EPCAM, as well as SIX2 and Ki-67 (Fig. 12E). As explained before, these marker combinations allow us to measure organoid composition, progenitor maintenance and cell proliferation. As expected, fractions of WT1-positive cells were strongly reduced in KO^{iPSC} organoids compared to not-edited counterparts. This correlated with the respective fractions in d9 NPCs and thus with the KO efficiencies of the corresponding gRNAs. In contrast, EPCAM staining was barely affected, and we observed very similar fractions of WT1-EPCAM double-positive cells, despite the overall reduction of WT1. This indicates that EPCAM-positive tubules mostly developed normally, while *WT1* KO preferentially affected the generation of glomerular podocytes and to a lesser extent the WT1-EPCAM double-positive subtype.

We measured an increase in Ki-67-positive cells upon *WT1* KO, as well as large fractions of SIX2-positive cells in KO^{iPSC} organoids, whereas SIX2 was absent from not-edited controls. This indicates that *WT1* KO leads to a retention of SIX2-positive, undifferentiated NPCs in d21 organoids. Notably, the percentage of SIX2-positive cells in KO^{iPSC} organoids correlated with *WT1* KO efficiency. Consequently, *WT1* KO using gRNA3 yielded the greatest SIX2-positive fraction with 30% of SIX2-positive cells (Fig. 12E). Intriguingly, a substantial fraction of SIX2-positive cells co-stained for Ki-67, and might therefore represent a proliferating progenitor population that persisted during kidney organoid formation in KO^{iPSC} organoids.

We decided to confirm the maintenance of SIX2-positive cells upon *WT1* KO by performing IF staining for SIX2 and EPCAM in cryosections derived from d21 organoids of all three gRNA lines (Fig. 12F). In agreement with our flow cytometry data, not-edited organoids from all three lines were nicely structured and completely devoid of SIX2. In contrast, we detected many SIX2-positive cells in *WT1* KO organoids that were exclusive to unstructured parts of the organoids, thus confirming our flow cytometry data.

Taken together, KO of *WT1* interferes with proper organoid development and appears to prevent the differentiation of SIX2-expressing nephron progenitors into mature nephron structures.

Due to the general reproducibility of the aforementioned phenotypes across three gRNAs and the scaling of phenotypic strength with KO efficiency, we considered our observations as *WT1* KO-specific and not as off-target effects. Taking into account differences in KO efficiencies, growth behavior and flow cytometry results, we decided to select gRNA3 for future experiments.

Results

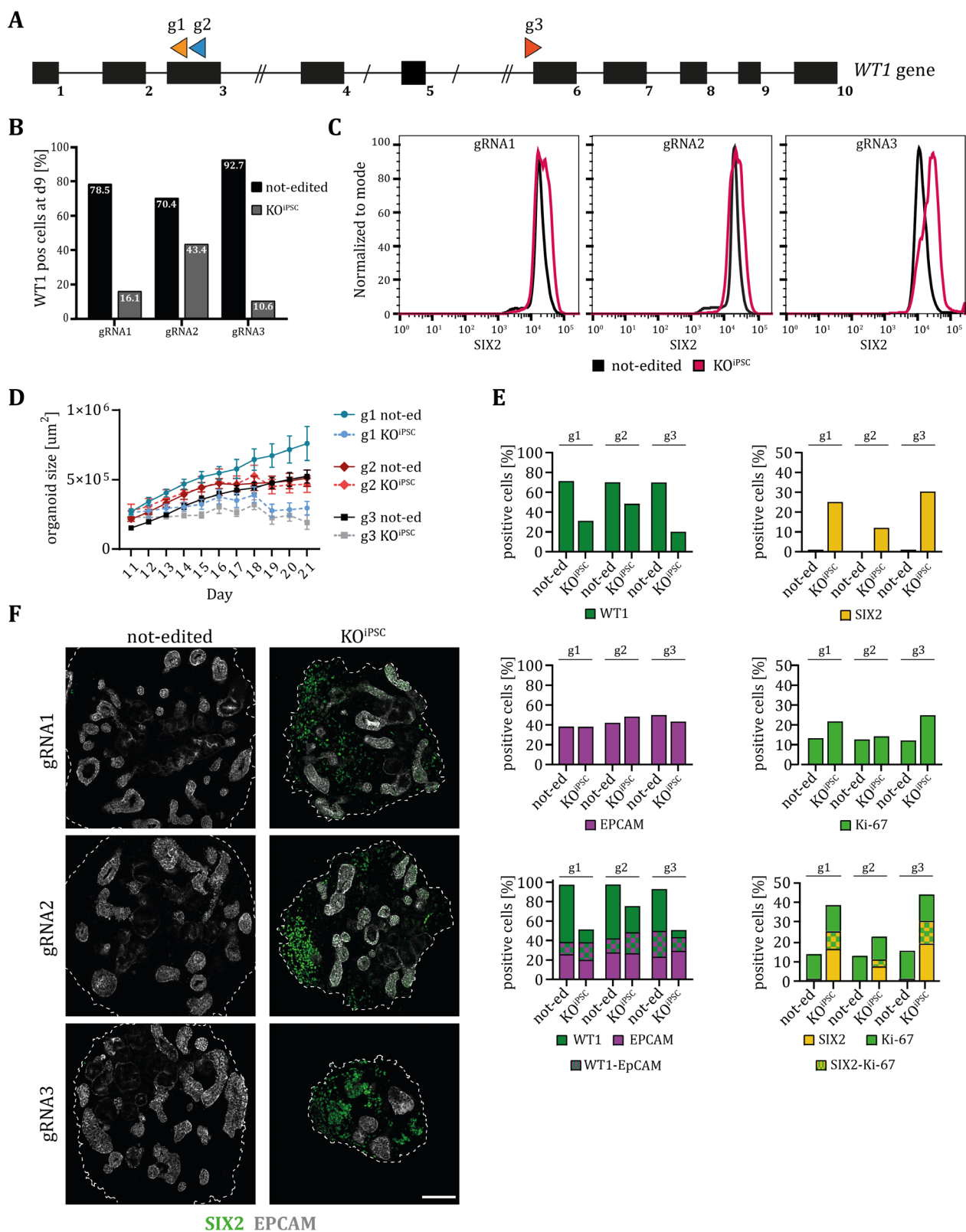


Figure 12. Inducible KO of *WT1* results in maintenance of *SIX2*-expressing cells in d21 organoids.

A: Scheme of *WT1* gene and position of gRNAs. Numbers refer to exon numbers of the *WT1* gene.
B: Flow cytometry analysis of *WT1* in d9 NPCs derived from WT29-iCas9 cells transduced with distinct gRNAs. Values are presented in % for not-edited and KO^{iPSC} NPCs for three distinct gRNAs. Data is derived from one test. Values in the bars represent respective percentages.

C: Flow cytometry histograms show SIX2 staining in d9 NPCs from the same conditions as in **B**.

D: Growth of organoids derived from not-edited and corresponding KO^{iPSC} cells of the three gRNA lines from d11 to d21. Values in μm^2 are derived from Incucyte® images and are presented as mean +/- SD for a minimum of n=24 organoids per condition from one test.

E: Flow cytometry analysis of the indicated markers in pooled d21 organoids derived from not-edited and corresponding KO^{iPSC} cells of the three gRNA lines. Data from one test is shown.

F: IF staining for SIX2 and EPCAM in d21 organoids from the same conditions as in **E**. Scale bar: 100 μm
g1/2/3 = gRNA1/2/3; not-ed = not-edited

3.5.3 *WT1* KO time course

WT1 is expressed throughout kidney development and plays a role at different developmental stages. In order to decipher more stage-specific roles of *WT1* in kidney organoid development, we performed a *WT1* KO time course by inducing Cas9 expression at different time points in the protocol. Besides KO in iPSCs prior to differentiation (KO^{iPSC}), we induced Cas9 expression from d4-7 (KO^{d4-7}), d9-11 (KO^{d9-11}) and d11-14 (KO^{d11-14}) (Fig. 13A). We assessed *WT1* expression in d9 NPCs derived from not-edited, KO^{iPSC} and KO^{d4-7} cells, and measured an average of 85.3%, 15.4% and 28.7% *WT1*-positive cells, respectively. This means that KO efficiency was slightly reduced in KO^{d4-7} NPCs (66%) compared to KO^{iPSC} NPCs (82%) (Fig. 13B). To analyze potential *WT1* KO phenotypes, we recorded organoid growth and collected organoids at d21 for flow cytometry and IF.

Following up on the growth phenotype observed for KO^{iPSC} organoids (Fig. 12D), we recorded organoid growth during our KO time course (Fig. 13D). In contrast to KO^{iPSC} organoids, which again were much smaller than not-edited organoids, KO at later time points did not inhibit organoid growth to such an extent. In contrast, KO^{d4-7} and KO^{d9-11} cells even gave rise to bigger organoids at d21 compared to wildtype. Since we found a general increase in Ki-67-positive cells and detected a Ki-67-SIX2 double-positive population in *WT1* KO organoids (Fig. 12E), we wondered whether this cycling cell population could drive organoid growth beyond d21. Therefore, we continued our growth measurements for another two weeks. Strikingly, we observed a massive overgrowth of KO^{d4-7} and KO^{d9-11} organoids compared to the not-edited control. KO^{d11-14} organoids also grew bigger than the control, despite the absence of SIX2. Notably, KO^{iPSC} organoids increased in size upon prolonged culture, but they remained smaller than not-edited organoids (Fig. 13D).

We were particularly surprised by the difference in growth behavior between KO^{iPSC} and KO^{d4-7} organoids. In both cases, *WT1* KO was induced at early time points and resulted in a strong reduction of *WT1* protein expression (Fig. 13B). However, KO^{iPSC} organoids stayed small and morphologically showed signs of cell death, whereas KO^{d4-7} organoids grew very large. We therefore wondered whether cell death pathways were activated in KO^{iPSC} organoids as opposed

to not-edited and KO^{d4-7} organoids. To address this, we performed a cleaved caspase assay on growing organoids as a measure for apoptosis (Fig. 13E). Compared to not-edited organoids, we found a strong increase in caspase activation in KO^{iPSC} organoids, after adding the detection reagent at d14. To our surprise, caspase activation was also strongly induced in KO^{d4-7} organoids, albeit to a lesser extent than in KO^{iPSC} organoids. This indicates that in both KO situations, loss of WT1 induces increased cell death, which was balanced against a concomitant increase in proliferation.

As expected, flow cytometry and IF staining revealed a strong decrease in WT1-positive cells in d21 organoids across all KO time points (Fig. 13C; 14A). Similarly, and in contrast to our test using all three gRNAs (Fig. 12E), we found less WT1-EPCAM double-positive cells, which was statistically significant for KO^{iPSC} , KO^{d4-7} and KO^{d11-14} organoids (Fig. 13C, top right). Residual WT1-positive cells mostly organized into PODXL-positive glomerular structures. Likewise, we observed few remaining NPHS1-positive glomeruli, directly adjacent to residual LTL-positive proximal tubules, which indicates correct arrangement of such proximal nephron structures (Fig. 14A).

In contrast, the frequency of EPCAM-positive cells, representing tubules, was higher in KO^{iPSC} , KO^{d4-7} and KO^{d9-11} d21 organoids, whereas it appeared slightly reduced in affected in KO^{d11-14} organoids (Fig. 13C, top). To our surprise, in IF stainings, EPCAM-positive tubules seemed reduced in all *WT1* KO organoids compared to not-edited organoids, which contrasts our flow cytometry results.

In addition to quantifying nephron composition, we also analyzed Ki-67 and SIX2 (Fig. 13C, bottom; 14A). As expected, we found Ki-67 staining strongly increased in KO^{d4-7} and KO^{d9-11} , and slightly increased in KO^{d11-14} organoids, compared to not-edited controls. Notably, in this specific experiment, Ki-67 did not appear elevated in KO^{iPSC} organoids. However, flow cytometry analysis across several experiments confirmed a statistically significant increase in the frequency of Ki-67-positive cells in KO^{iPSC} , KO^{d4-7} and KO^{d9-11} organoids (Fig. 13C), which indicates that *WT1* KO leads to elevated proliferation. Notably, the increase in Ki-67-positive cells was very similar in KO^{iPSC} and KO^{d4-7} cells despite their different growth behaviors. However, Ki-67 only indicates the fraction of cycling cells but does not inform about how fast cells progress through the cell cycle, which could be assessed using bromodeoxyuridine (BrdU) pulse chase experiments.

More strikingly, we detected many patches of SIX2-positive cells upon *WT1* KO (Fig. 14A). These amounted to an average of 50%, 38% and 17% of SIX2-positive cells in KO^{iPSC} , KO^{d4-7} and KO^{d9-11} organoids, respectively (Fig. 13C). Notably, SIX2-expressing cells were completely absent from both not-edited and KO^{d11-14} d21 organoids (Fig. 13C; 14A). Around 40-50% of SIX2-positive cells co-stained for Ki-67, which as before, suggests that *WT1* KO organoids retain a proliferating nephron progenitor population (Fig. 13C).

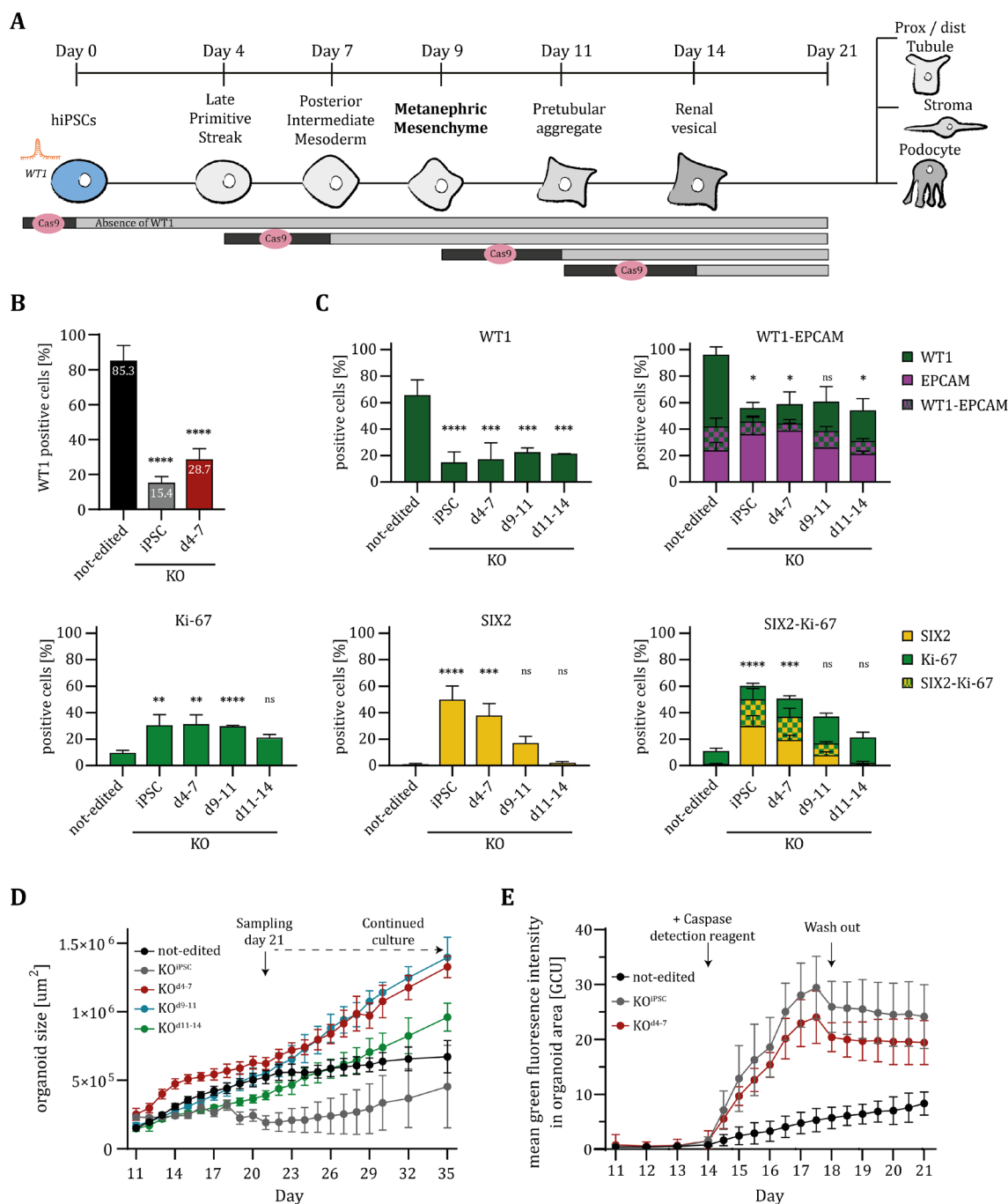


Figure 13. *WT1* KO at different time points elicits distinct phenotypes in *WT1* KO organoids.

A: Schematic outline of the protocol. Periods of Cas9 induction and absence of WT1 are indicated. Note that WT1 becomes depleted during the Cas9 induction period. Prox = proximal; Dist = distal

B: Flow cytometry analysis of WT1 in d9 NPCs derived from not-edited, KO^{iPSC} or KO^{d4-7} cells. Data is presented as mean \pm SD from $n=7$ independent experiments. Values in bars represent mean percentages.

C: Flow cytometry analysis of pooled d21 organoids derived from not-edited, KO^{iPSC}, KO^{d4-7}, KO^{d9-11} and KO^{d11-14} cells. Data is presented as mean \pm SD derived from $n=5$ (not edited, KO^{iPSC}, KO^{d4-7}) or $n=2$ (KO^{d9-11}, KO^{d11-14}) independent experiments. Two-sided student's t-test; p -value: ns >0.05 ; * ≤ 0.05 ; ** ≤ 0.01 ; *** ≤ 0.001 ; **** ≤ 0.0001 ; WT1-EPCAM / SIX2-Ki-67: asterisks correspond to the WT1-EPCAM and SIX2-Ki-67 populations.

D: Growth of organoids derived from the same conditions as in **C** between d11 and d35. Values in μm^2 are derived from Incucyte® images and are presented as mean \pm SD for a minimum of $n=10$ organoids across all time points from one representative experiment.

E: Cleaved caspase assay in not-edited, KO^{iPSC} and KO^{d4-7} organoids. Caspase reagent was added at d14 and washed out from d18. Values were extracted from Incucyte® images and are presented as mean green fluorescence intensity in organoid area (GCU = green calibrated unit) +/- SD for n=16 organoids per condition, derived from one of three representative experiments.

In addition, these findings indicate that *WT1* KO from d11-14 does not affect the differentiation of SIX2-expressing cells anymore.

Intriguingly, we found that SIX2-positive nuclei in *WT1* KO organoids were frequently surrounded by a weakly EPCAM-positive mesh (Fig. 14B). In contrast to EPCAM-positive tubules, these cells were not particularly organized. In order to exclude an IF-specific staining artifact, we performed flow cytometry analysis of combined SIX2 and EPCAM staining on not-edited and KO^{d4-7} d21 organoids (Fig. 14C). Not-edited organoids were negative for SIX2 and displayed a range of EPCAM intensities that were particularly concentrated into a negative and a highly positive population. Based on this pattern, we categorized the EPCAM staining into EPCAM^{high}, EPCAM^{mid} and EPCAM^{low} (Fig. 14C, left). When we applied this categorization to a representative KO^{d4-7} sample, we found that a large fraction of SIX2-positive cells displayed EPCAM^{mid} staining. The remaining SIX2-expressing cells were EPCAM^{low} and only very few were EPCAM^{high}. We reasoned that in a classical gating strategy of EPCAM-positive versus EPCAM-negative cells, a fraction of SIX2-EPCAM^{mid} cells are counted as EPCAM-positive, resulting in unchanged or even elevated frequencies of EPCAM-positive cells, as seen above, even though this does not reflect actual tubules (Fig. 12E; 13C). Therefore, we instead quantified EPCAM^{high}, EPCAM^{mid} and EPCAM^{low} cells in our different KO conditions (Fig. 14D). Indeed, we observed significantly reduced fractions of EPCAM^{high} cells in all KO organoids, compared to not-edited controls, which is in agreement with fewer EPCAM-positive tubules present in IF stainings of *WT1* KO organoids (Fig. 14A). At the same time, fractions of EPCAM^{mid} cells were significantly increased in KO^{iPSC} and KO^{d4-7} organoids, slightly, but not significantly, elevated in KO^{d9-11} organoids, and almost unchanged in KO^{d11-14} organoids, compared to not-edited organoids.

Two studies from the 1990s showed that *WT1* represses the expression of *IGF2* potentially by directly binding to its mRNA (Caricasole et al., 1996; Drummond et al., 1992). Due to its well-described role in Wilms tumor, we decided to check for this potential connection by staining for IGF2 in *WT1* KO organoids. Interestingly, we indeed found a strong induction of IGF2 upon *WT1* KO (Fig. 14A). IGF2 staining was present in a subset of cells and appeared strictly confined to unstructured regions of the respective organoids. We hypothesized that upregulation of IGF2 could serve as a surrogate marker for actual *WT1* KO cells within a heterogeneous pool of wildtype, heterozygous and KO cells. However, such a conclusion would require more elaborate experiments.

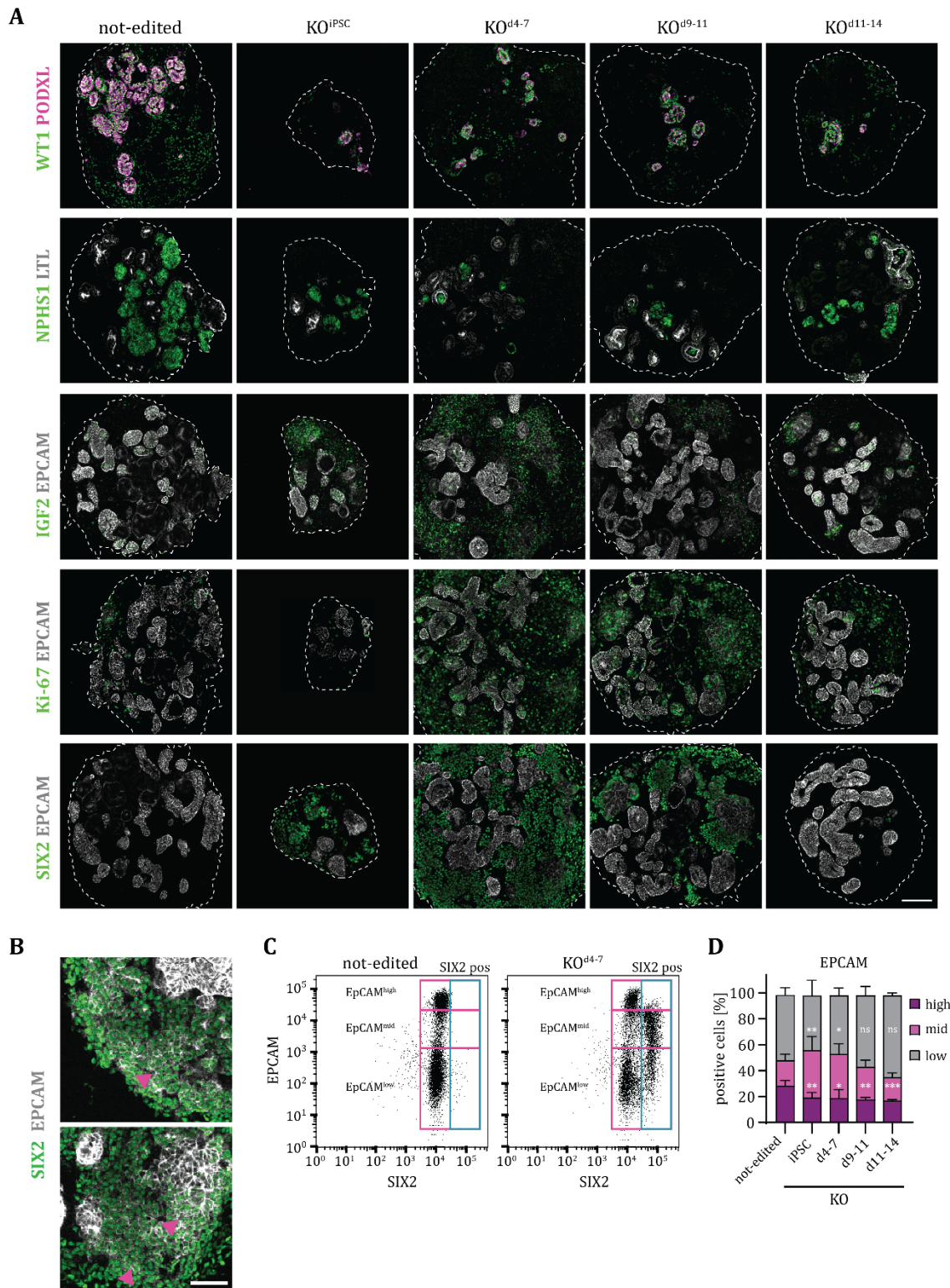


Figure 14. *WT1* KO organoids contain fewer nephron structures, upregulate IGF2 and harbor novel SIX2-EPCAM double-positive cells.

A: IF staining for the indicated markers in representative d21 organoids derived from not-edited, KO^{iPSC}, KO^{d4-7}, KO^{d9-11} and KO^{d11-14} cells. Scale bar: 100 μ m

B: Detail image of a d21 organoid from KO^{d4-7} stained for SIX2 and EPCAM. The image is overexposed to visualize EPCAM staining surrounding SIX2-positive cells (pink arrowheads). Scale bar: 500 μ m

C: Representative flow cytometry plots showing SIX2-EPCAM staining in pooled d21 organoids derived from not-edited and KO^{d4-7} cells. Pink boxes show categorization of EpCAM^{high}, EPCAM^{mid} and EpCAM^{low} used to quantify populations in **D**. Blue box indicates SIX2-positive cells. pos = positive

D: Flow cytometry analysis of EpCAM^{high}, EPCAM^{mid} and EpCAM^{low} populations in pooled d21 organoids derived from the same conditions as in **A**. Data is presented as mean +/- SD derived from n=5 (not-edited, KO^{iPSC}, KO^{d4-7}) or n=2 (KO^{d9-11}, KO^{d11-14}) independent differentiation experiments.

Two-sided student's t-test; *p*-value: ns > 0.05; * ≤ 0.05; ** ≤ 0.01; *** ≤ 0.001; asterisks are placed above the respective populations (EPCAM^{high} and EPCAM^{mid}).

Taken together, our data suggest that nephron structures like glomeruli and tubules are reduced in *WT1* KO organoids across all KO time points. A balance between increased cell death and elevated proliferation determines the growth behavior of *WT1* KO organoids. Upregulation of IGF2 upon *WT1* KO points to a regulatory relationship between these two Wilms tumor loci. Finally, loss of *WT1* no later than d9-11 prevents proper differentiation of SIX2-expressing NPCs and gives rise to abnormal SIX2-EPCAM double-positive cells.

3.5.4 Influence of *WT1* KO on different processes during organoid development

In addition to analyzing d21 organoids, we wondered how different time points of *WT1* KO might influence distinct stages of organoid development. We were mainly interested in the following questions: From which stage on is *WT1* expressed? How quickly is *WT1* depleted upon Cas9 induction? When is SIX2 downregulated in wildtype and maintained in KO organoids? Are additional progenitor markers maintained? How is the generation of more mature structures like tubules or glomeruli affected? Can we determine when the novel SIX2-EPCAM double-positive population arises? At what stages is cell proliferation mainly affected? To address these, we induced Cas9 expression during the aforementioned time spans (Fig. 13A), and collected samples for qPCR and flow cytometry at different time points throughout our differentiation protocol.

As expected, *WT1* mRNA expression patterns were very similar in all not-edited and KO conditions. *WT1* mRNA was first detectable at d6, peaked at d9, went into a trough at d10 and came up again from d11 until d21 (Fig. 15A). However, throughout kidney organoid development, *WT1* mRNA levels were higher in not-edited compared to all KO samples, suggesting either a self-regulatory feedback loop of *WT1* on its own transcription or decreased half-life of the mRNA transcribed from mutant *WT1*. Not-edited cells acquired *WT1* protein expression between d5 and d6 when around 50% of cells were *WT1*-positive, whereas this percentage stayed low in KO^{iPSC} and KO^{d4-7} cells, indicating that Cas9 induction between d4-7 already affected protein expression by d6 (Fig. 15B). *WT1*-positive cell fractions peaked at d9, with more than 80% of not-edited but only around 15% and 20% of KO^{iPSC} and KO^{d4-7} cells expressing *WT1* protein, respectively. Consistent with our previous results, large fractions of not-edited cells retained *WT1* expression, resulting in around 70% of *WT1*-positive cells in d21 organoids, whereas KO^{iPSC} and KO^{d4-7} as well

as KO^{d9-11} and KO^{d11-14} d21 organoids contained around 20% and 35% of WT1-positive cells, respectively. Notably, fractions of WT1-positive cells dropped strongly between d12 and d14 in KO^{d11-14} organoids, which suggests that the induction of double-strand breaks and degradation of WT1 protein takes around two days to be completed.

Overall, this analysis shows that throughout kidney organoid development, a large fraction of cells is WT1-positive. A drop in *WT1* mRNA and protein expression detected in d10 samples may be attributed to the effects of CHIR treatment between d9 and d10.

One of the most interesting phenotypes of *WT1* KO is the maintenance of *SIX2* in organoids of KO^{iPSC} , KO^{d4-7} and KO^{d9-11} cells. *SIX2* mRNA started being expressed at around d6, and peaked around d7 and d9 (Fig. 15A). Notably, *SIX2* mRNA expression was considerably higher in KO^{iPSC} and KO^{d4-7} cells, compared to not-edited cells. This directly translated into a higher percentage of *SIX2*-positive cells in *WT1* KO compared to not-edited cells at this stage, which we also observed previously in NPCs (Fig. 15B; 12C). In not-edited cells, *SIX2* mRNA expression sharply declined starting at d10. Likewise, the percentage of *SIX2*-positive cells dropped to zero by d12. In contrast, both *SIX2* mRNA and the percentage of *SIX2*-positive cells stayed high in KO^{d4-7} and even more so in KO^{iPSC} organoids, resulting in 50% and 55% of *SIX2*-positive cells in d21 organoids, respectively. For KO^{d9-11} cells, the general trend of *SIX2* mRNA expression was similar, but expression levels were much lower, which resulted in smaller fractions of *SIX2*-positive cells at a given time point. Notably, we did not detect any *SIX2*-positive cells in KO^{d11-14} organoids, except for a small fraction at d21, even though *SIX2* mRNA expression was higher than in not-edited cells throughout. Considering the complete loss of *SIX2*-expressing cells in not-edited organoids at d12, this indicates that in KO^{d11-14} organoids *WT1* was sufficiently depleted only after *SIX2* had been downregulated, suggesting that KO of *WT1* results in a maintenance but not a reacquisition of *SIX2* expression.

Similar to *SIX2*, we assessed mRNA expression of an additional nephron progenitor marker, *SALL1* (Fig. 15C). Irrespective of *WT1* KO, we detected *SALL1* mRNA expression already in iPSCs. In all conditions, its expression peaked at d6/d7, and then decreased to very similar levels until d11. While *SALL1* mRNA expression stayed steady in not-edited and late KO conditions, its expression increased slightly in KO^{iPSC} and KO^{d4-7} cells, and stayed at this elevated level until d21. This indicates that additional NPC markers might be maintained during kidney organoid differentiation upon *WT1* KO.

Next, we analyzed how KO of *WT1* influenced kidney organoid formation beyond the NPC stage. To this end, we measured mRNA expression of *LHX1* and *NPHS1*, which are expressed in renal vesicles and glomeruli, respectively (Fig. 15C). In not-edited cells, *LHX1* mRNA was first expressed at around d6, got further upregulated towards d11, and stayed at high levels until d21. Notably,

in KO^{iPSC} and KO^{d4-7} cells *LHX1* expression was considerably lower between d6 and d14 but reached levels similar to not-edited organoids by d18 and d21. In contrast, *NPHS1* mRNA expression was roughly ten-fold lower in KO^{iPSC} and KO^{d4-7} cells at all time points and a little less reduced in KO^{d9-11} and KO^{d11-14} cells. After a local peak at d9, *NPHS1* transcript levels started rising from d12 onwards until d21, indicating the period of glomerulus development.

In addition, we measured the frequency of EPCAM- and WT1-EPCAM double-positive cells via flow cytometry (Fig. 15D). In order to analyze epithelialized glomerular cells, we first gated for WT1-EPCAM double-positive cells, and subsequently divided all remaining cells into EPCAM^{high}, EPCAM^{mid} and EPCAM^{low} cells in order to deduce information on the generation of tubules. Almost 100% of iPSCs expressed high levels of EPCAM. In not-edited cells, EPCAM was downregulated towards d6 via an interim EPCAM^{mid} state. EPCAM levels rose again starting at d7. In all conditions, EPCAM^{high} cells re-appeared at d14 and their frequency steadily increased to 40% in not-edited d21 organoids, indicating the emergence of first tubular structures by d14. As expected, *WT1* KO reduced the fraction of EPCAM^{high} cells that developed from d14, particularly in KO^{iPSC} and KO^{d4-7} cells. The first WT1-EPCAM double-positive cells appeared slightly earlier at d12. This population expanded in not-edited organoids until up to 18% double-positive cells at d21, whereas KO organoids only contained around 5-10%, depending on the KO condition.

The fraction of EPCAM^{mid} cells was very similar in all conditions until d14. In not-edited, KO^{d9-11} and KO^{d11-14} cells, the percentage of EPCAM^{mid} cells stayed at very steady levels until d21 and ranged at around 10-15%. In contrast, this population expanded considerably in KO^{iPSC} and KO^{d4-7} organoids to around 40% at d21, which is consistent with our previous results (Fig. 15D; 14D).

As described before, a large fraction of EPCAM^{mid} cells was positive for SIX2 in KO^{iPSC}, KO^{d4-7} and KO^{d9-11} organoids. We therefore assessed the frequency of SIX2-positive cells within EPCAM^{high}, EPCAM^{mid} and EPCAM^{low} cell populations in these KO conditions (Fig. 15E). As expected, we did not detect any SIX-positive cells within the EPCAM^{high} population, suggesting that maintenance of SIX2 and differentiation into EPCAM^{high} tubules are mutually exclusive fates. In contrast, we observed a high frequency of SIX2-positive cells in both, the EPCAM^{low} and EPCAM^{mid} populations. The frequencies of SIX2-EPCAM^{low} cells were rather steady between d10 and d21 after they peaked at d9, and ranged around 20% and 15% in KO^{iPSC} and KO^{d4-7} organoids, respectively. We also found very few SIX2-EPCAM^{low} cells in KO^{d9-11} organoids. In contrast, the frequencies of SIX2-EPCAM^{mid} cells increased considerably within the same time interval and reached up to 35% of cells in KO^{iPSC} and KO^{d4-7} organoids, and up to 10% of cells in KO^{d9-11} organoids. This identifies SIX2-EPCAM^{mid} cells to be particularly proliferative, whereas SIX2-EPCAM^{low} cells did not expand over time.

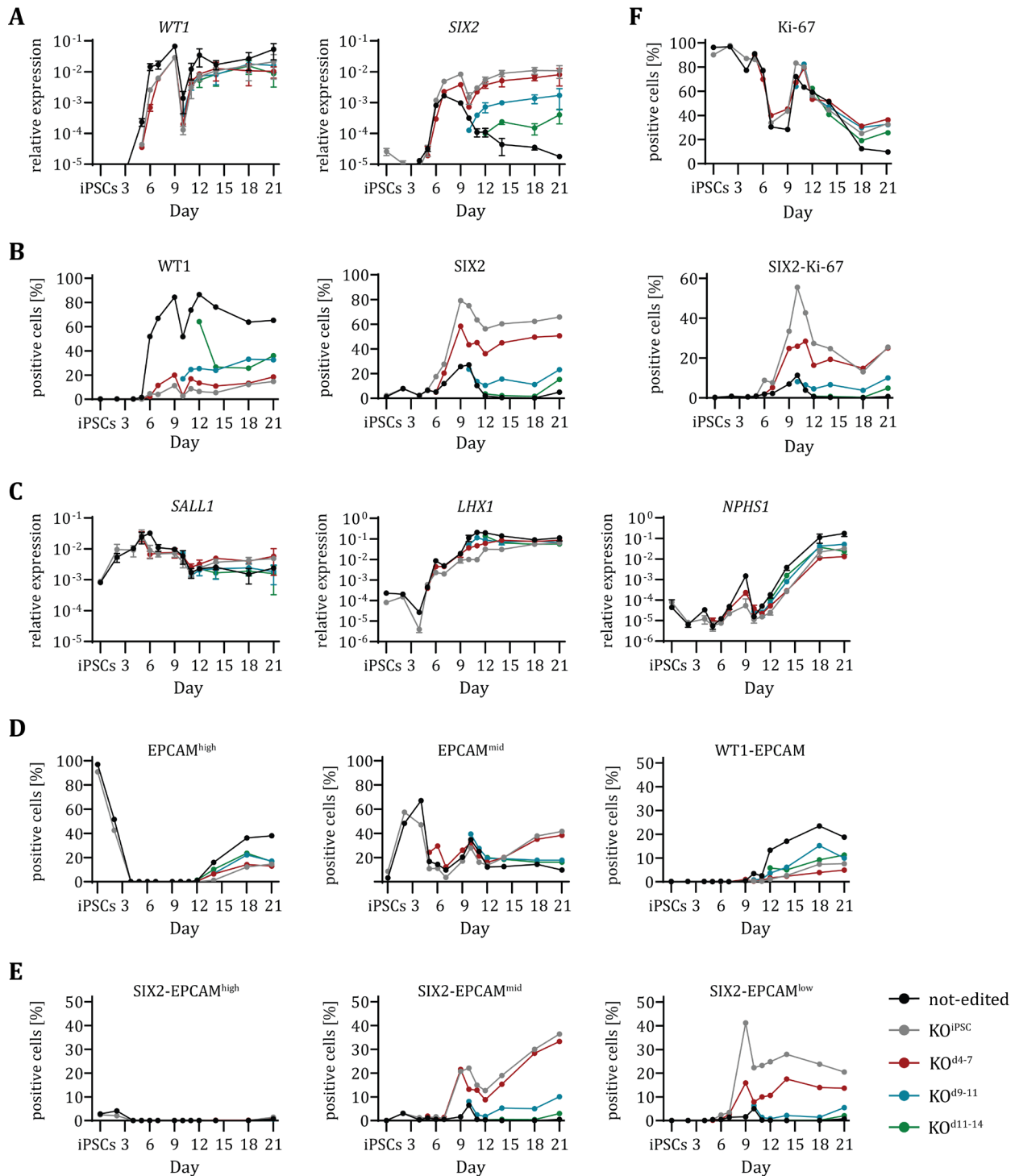


Figure 15. Influence of *WT1* KO on different processes during organoid development.

A: qPCR analysis of *WT1* and *SIX2* expression in not-edited, KO^{iPSC}, KO^{d4-7}, KO^{d9-11} and KO^{d11-14} cells at the indicated time points (see bottom right in Figure).

B: Flow cytometry analysis of *WT1* and *SIX2* in the same conditions as in **A**.

C: qPCR analysis of *SALL1*, *LHX1* and *NPHS1* expression in the same conditions as in **A**.

D-E: Flow cytometry analysis of *EPCAM*^{high}, *EPCAM*^{mid} and *WT1-EPCAM* double-positive cells (**D**) and of *SIX2-EPCAM*^{high}, *SIX2-EPCAM*^{mid} and *SIX2-EPCAM*^{low} cells (**E**) in the same conditions as in **A**.

F: Flow cytometry analysis of *Ki-67* and *SIX2-Ki-67* double-positive cells in the same conditions as in **A**.

Results

To B+F: Note the low fraction of SIX2-positive cells in not-edited samples at d9 compared to **Fig. 12C**. We ascribe this to technical issues with gating and assume that the SIX2 antibody may be limiting. Flow cytometry data is presented as % of cells; qPCR data is presented as expression relative to *GAPDH* shown as mean +/- SD from technical duplicates.

Finally, we measured proliferation during kidney organoid differentiation by detecting Ki-67-positive cells (Fig. 15F). While almost 100% of cells proliferated during the first six days of differentiation, the frequency of Ki-67-positive cells abruptly declined around the NPC stage and went back up sharply towards d10/d11, irrespective of the condition, and reached levels between 72% and 83% of Ki-67-positive cells. Notably, we detected more Ki-67-positive cells in KO compared to not-edited cells between d9 and d11. In not-edited organoids percentages of Ki-67-positive cells decreased strongly as of d14 and reached 10% at d21, indicating that a great majority of cells stopped proliferating in d21 organoids. KO^{iPSC} and KO^{d4-7} retained much more Ki-67-positive cells and their frequency even increased again to 40% at d21. As expected, from d9 onwards, we found Ki-67-SIX2 double-positive cells in KO^{iPSC} and KO^{d4-7} and to a lesser extent in KO^{d9-11} organoids. Interestingly, after a short decline towards d18, frequencies started to rise again until d21 similar to total Ki-67. This indicates that proliferation was elevated in *WT1* KO compared to not-edited organoids especially around the NPC stage and in d21 organoids. A large fraction of SIX2-positive cells proliferated; however, it seemed that this fraction was not constant throughout organoid development.

Considering all qPCR and flow cytometry data explained above, we can deduce the following observations: In not-edited organoids, mature nephron structures first emerge between d12 and d14, as shown by expression of *NPHS1* as well as increase in both EPCAM^{high} and EPCAM-*WT1* double-positive cells, representing the development of tubules and glomeruli. Consistent with this, SIX2 gets downregulated and is completely lost from not-edited organoids by d12. A large fraction of cells proliferates throughout kidney organoid differentiation, except the NPC stage, and proliferation ceases in d21 organoids. Upon *WT1* KO, acquisition of mature nephron structures is impeded, expression of SIX2 and *SALL1* are maintained and proliferation is stalled to a lesser extent.

Notably, most of these phenotypes occurred in all KO organoids, irrespective of *WT1* KO before or after the NPC stage. The failure to maintain SIX2 expression in KO^{d11-14} organoids is one exception, which suggests that a reduction of mature structures in KO^{d11-14} organoids is due to specific effects of *WT1* loss later in kidney organoid development. The great majority of phenotypes was stronger upon early KO and weaker upon late KO. This may also be explained by a decrease in KO efficiency towards later editing time points that had been observed before (R. Ungricht, personal communication). Importantly, SIX2 and high levels of EPCAM were mutually exclusive, which is in agreement with SIX2 and high EPCAM being present in

mesenchymal NPCs and epithelial tubules, respectively. Importantly, we observed a differentiation-resistant SIX2-EPCAM^{mid} cell population, which considerably expanded between d12 and d21. This points to an intermediate cell state of NPC identity prior to fully committing to epithelial differentiation.

3.6 RNA-seq of *WT1* KO and wildtype samples

3.6.1 Quality control experiments

In order to define molecular changes imposed by loss of *WT1* we performed RNA-seq of not-edited, KO^{iPSC} and KO^{d4-7} samples collected at d5, d7, d9, d11, d12 and d21 (Fig. 16A).

We assessed the frequency of *WT1*-positive cells in not-edited and both KO conditions as a measure for KO efficiency, and found very reproducible *WT1* expression across three replicates (Fig. 16B). Wildtype NPCs had around 91% *WT1*-positive cells, and this fraction was reduced to around 18% and 34% in KO^{iPSC} and KO^{d4-7} NPCs, respectively, confirming successful *WT1* KO.

In addition, we measured organoid size at d21 (Fig. 16C). As expected, KO^{iPSC} organoids were smaller than not-edited counterparts. However, the same held true for KO^{d4-7} organoids, which contrasts previous experiments, where KO^{d4-7} organoids tended to be larger than not-edited ones. Considering our findings that KO^{d4-7} organoids particularly grow after d21 (Fig. 13D), we assumed that increased growth of KO^{d4-7} organoids in these experiments would manifest upon prolonged culture as well.

We also performed flow cytometry on d21 organoids (Fig. 16D) and measured a reduction of *WT1*-positive cells in both KO conditions, albeit to different extents. Consequently, we also observed a reduction of *WT1*-EPCAM double-positive cells except for KO^{iPSC} organoids of replicate 3. As an additional characteristic of *WT* KO organoids, the EPCAM^{mid} population expanded in both KO conditions, compared to not-edited organoids, whereas the EPCAM^{high} population was mildly reduced. Most importantly, we detected around 50% and 30% of SIX2-positive cells in d21 organoids from KO^{iPSC} and KO^{d4-7} cells, respectively. Likewise, we found a higher frequency of Ki-67-positive cells upon *WT1* KO, and consequently also an increase in Ki-67-SIX2 double-positive cells.

In addition, we performed IF staining for the abovementioned markers on cryosections derived from d21 organoids and obtained very similar results as in previous experiments (not shown).

Overall, these control experiments confirmed that our collected samples reflected our established phenotypes and were therefore suitable for RNA-seq analysis.

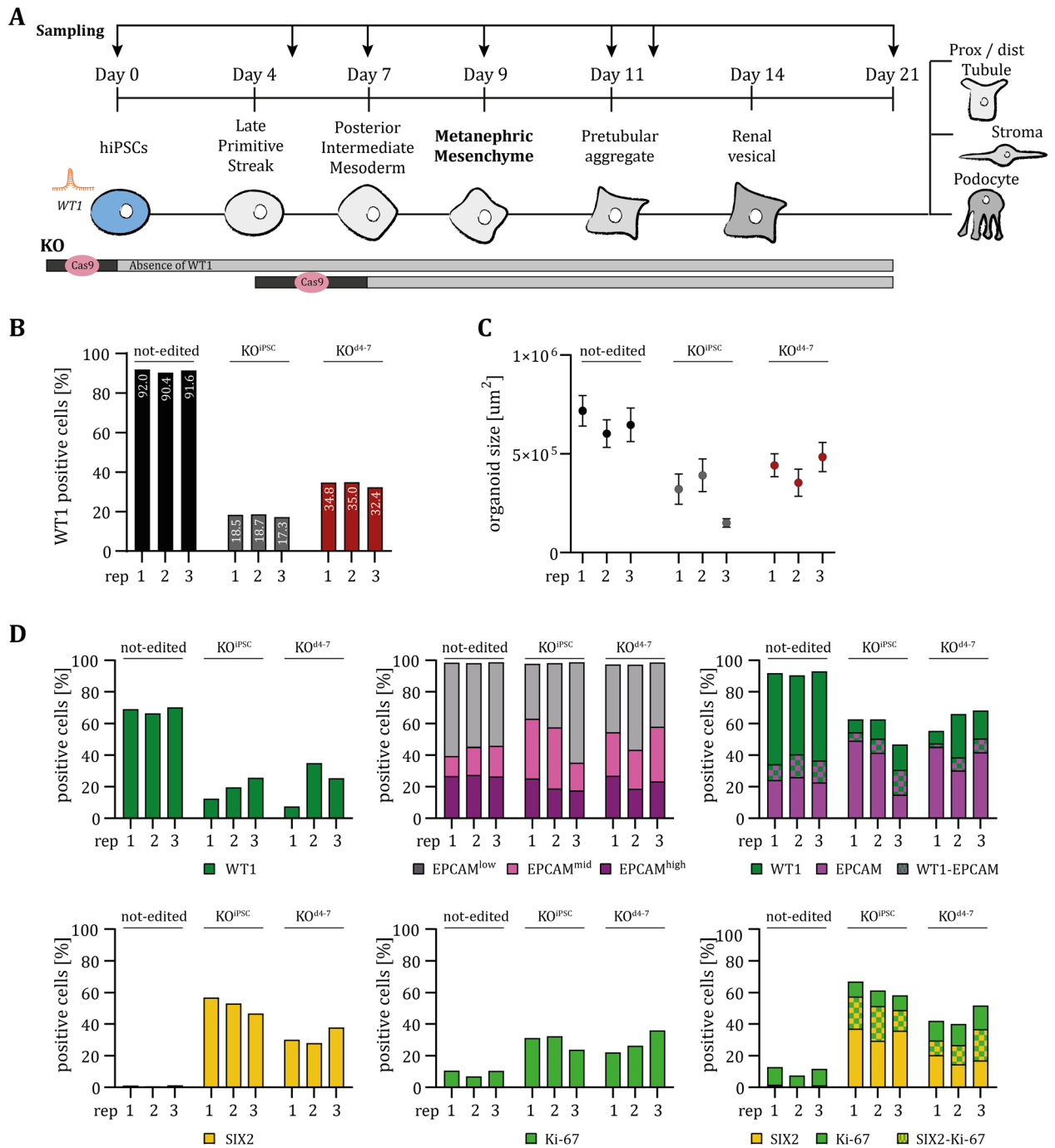


Figure 16. Set-up and quality controls of RNA-seq experiments.

A: Schematic outline of RNA-seq experiments. Periods of Cas9 induction and time points of sampling are indicated. Prox = proximal; Dist = distal

B: Percentage of WT1-positive cells in d9 NPCs derived from not-edited, KO^{iPSC} and KO^{d4-7} cells is shown for each of the three RNA-seq replicates. Values in the bars represent respective percentages.

C: Sizes of d21 endpoint organoids derived from not-edited, KO^{iPSC} and KO^{d4-7} cells are shown for each of the three RNA-seq replicates. Values in μm^2 are extracted from Incucyte® images and are presented as mean \pm SD for a minimum of n=40 organoids per condition.

D: Flow cytometry analysis of the indicated markers in pooled d21 organoids derived from not-edited, KO^{iPSC} and KO^{d4-7} cells. Data is presented as % of cells for each of the three RNA-seq replicates. rep = replicate

3.6.2 Transcriptional changes upon *WT1* KO reflect impaired differentiation and maintenance of progenitor cells

As a quality check, we first confirmed that transcriptional changes in our not-edited d21 organoids relative to iPSCs correlated well with those reported in d26 organoids using the same (Morizane; Pearson's correlation coefficient $R=0.7$) and a different (Little; $R=0.7$) kidney organoid differentiation protocol (Wu et al., 2018) (Fig. 17A).

Next, we employed principle component analysis (PCA) to characterize general organoid development defects upon KO of *WT1* (Fig. 17B). HiPSCs clustered together and away from all other samples on principle component (PC) 2 (explaining 29.1% of the transcriptional variance), while the remaining samples were arranged along PC1 (explaining 30.3% of the transcriptional variance). PC2 is therefore associated with changes underlying mesoderm specification from iPSCs, and PC1 with further organoid development. Control and KO samples were indistinguishable up to d12, but segregated along PC1 at d21. Notably, KO^{iPSC} and KO^{d4-7} d21 organoids did not overlap with d9 NPCs, or cells at d11 or d12. It remains to be determined if this is because of a developmental delay or a block in differentiation that is masked by the approximately 20-30% of unedited cells that form differentiated structures in KO organoids (Fig. 16B; 14A).

To examine the developmental defects in *WT1* KO organoids in more depth, we performed k-means clustering. By focusing on 7,653 significantly changing transcripts, we determined 17 gene clusters that were dynamically regulated during organoid development (Fig. 17C/D, left) and/or dysregulated upon *WT1* KO (Fig. 17C/D, right).

Clusters 5, 11 and 14 were either up- or downregulated relative to iPSCs during the differentiation of not-edited cells, but unchanged in *WT1* KO cells. Other clusters, in contrast, were deregulated in KO cells: Relative to not-edited samples, cluster 1 was mildly upregulated from d9 onwards and strongly at d21, thus antagonizing the downregulation of these genes observed in control d21 organoids. Similarly, cluster 8, which is continuously downregulated during organoid development, was unchanged in *WT1* mutants up to d12 but ectopically expressed at d21. Vice versa, induction of gene cluster 13 at d21 of organoid development was impaired in *WT1* KO d21 organoids. In addition, we found some clusters (15 and 17) that were temporarily suppressed relative to not-edited samples between d7 and d12, but unchanged at d21. Conversely, clusters 9 and 4 were upregulated at d5 and d9, respectively, but similarly compensated for at d21. Notably, we did not identify gene clusters that were consistently deregulated across the time span of *WT1* expression (d7-d21; see Fig. 15A/B), which indicates that *WT1* target genes are specific to different developmental stages. In addition, we did not observe drastic differences between KO^{iPSC} and KO^{d4-7} samples, particularly at d21.

Results

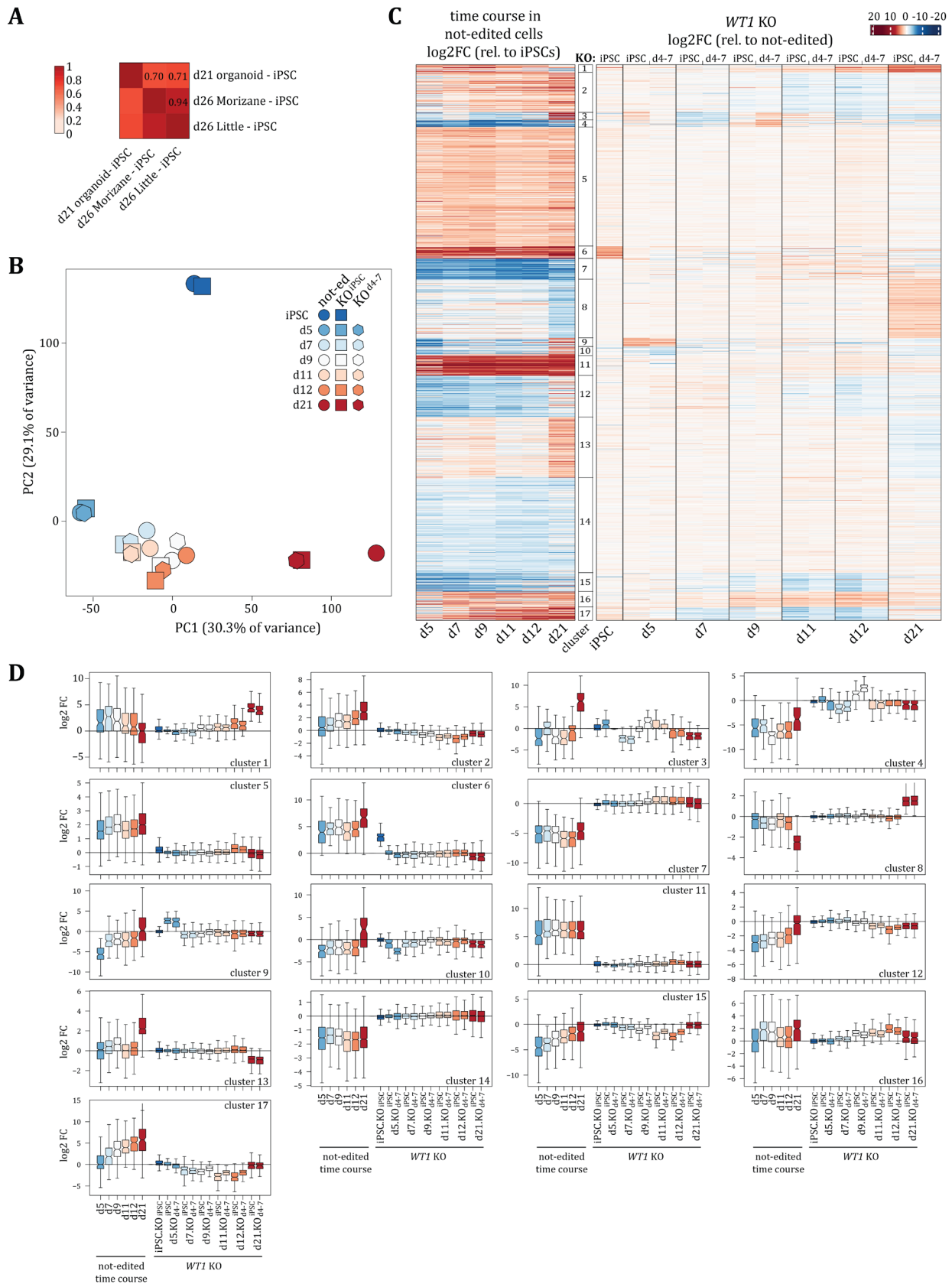


Figure 17. *WT1* KO organoids are developmentally delayed.

A: Pearson's correlation coefficients of pairwise comparisons between log2 FCs of indicated organoid samples relative to corresponding iPSC samples. "d21 organoid - iPSC" reflects our d21 not-edited organoids. Data for "d26 Morizane - iPSC" and "d26 Little - iPSC" is derived from Wu et al., 2018.

B: PCA of not-edited (control), KO^{iPSC} and KO^{d4-7} samples at the indicated time points. not-ed = not-edited

C: k-means clustering of 7,653 significantly changed genes (see Methods) in any of the shown contrasts. Left: differentiation time course in not-edited control cells: log₂ FC relative to iPSCs; Right: cell state differences in *WT1* KO samples: log₂ FC relative to respective not-edited control for each time point; rel = relative

D: Quantification of log₂ FC of gene clusters 1-17 in contrasts shown in **C**. Left: differentiation time course; Right: cell state differences of *WT1* KO relative to not-edited samples.

In some instances, changes seemed to be more pronounced in KO^{iPSC} samples, like downregulation of clusters 15 and 17 between d9-12. Vice versa, other changes were more pronounced in KO^{d4-7} samples, like upregulation of clusters 3 and 4 at d9. In general, however, these differences concerned the magnitude but not the direction of transcriptional changes.

Taken together, we found that KO of *WT1* antagonizes some of the developmental changes (in particular of clusters 1, 8 and 13) that are associated with kidney organoid differentiation of not-edited cells.

3.6.3 Deregulated gene clusters overlap with gene sets that define fetal kidney cell types

Since *WT1* KO strongly affects the cellular composition of kidney organoids as shown above, we wondered if any of the gene clusters were specific to individual kidney cell types. We therefore took advantage of a published gene set that discriminates human fetal kidney cell types (Lindström et al., 2018b), and calculated gene set overlap enrichments (see Methods). This revealed that particularly gene clusters 1, 8, 13 and 17 were enriched for marker genes that define cell types in the developing kidney (Fig. 18A).

Interestingly, cluster 1 strongly overlapped with genes defining NPCs (M1 NPCs) and to a lesser extent with a more advanced progenitor cell type (M2 NPCs primed to diff.). It indeed contained *bona fide* nephron progenitor markers like *SIX2*, *SIX1*, *EYA1* and *MEOX1*, which are specific to fetal kidney progenitor cells. Notably, cluster 1, similar to the M1 NPCs gene set, was transiently up- and then downregulated towards d21 during wildtype differentiation, which is consistent with the specification and subsequent differentiation of a kidney progenitor (Fig. 17D; 18C). In KO samples, cluster 1 was upregulated relative to not-edited samples starting from d9 and even more so at d21, indicating maintenance of progenitor programs in *WT1* KO organoids that are shut off in control kidney organoids (Fig. 17C/D). However, cluster 1 was strongly enriched for processes related to skeletal muscle development by gene ontology (GO) analysis (Fig. 18B), and included muscle-related genes like the muscle transcription factors *MYOD1* and *MYOG*. Therefore, despite containing canonical NPC markers, cluster 1 did not appear to represent a canonical nephron progenitor cluster.

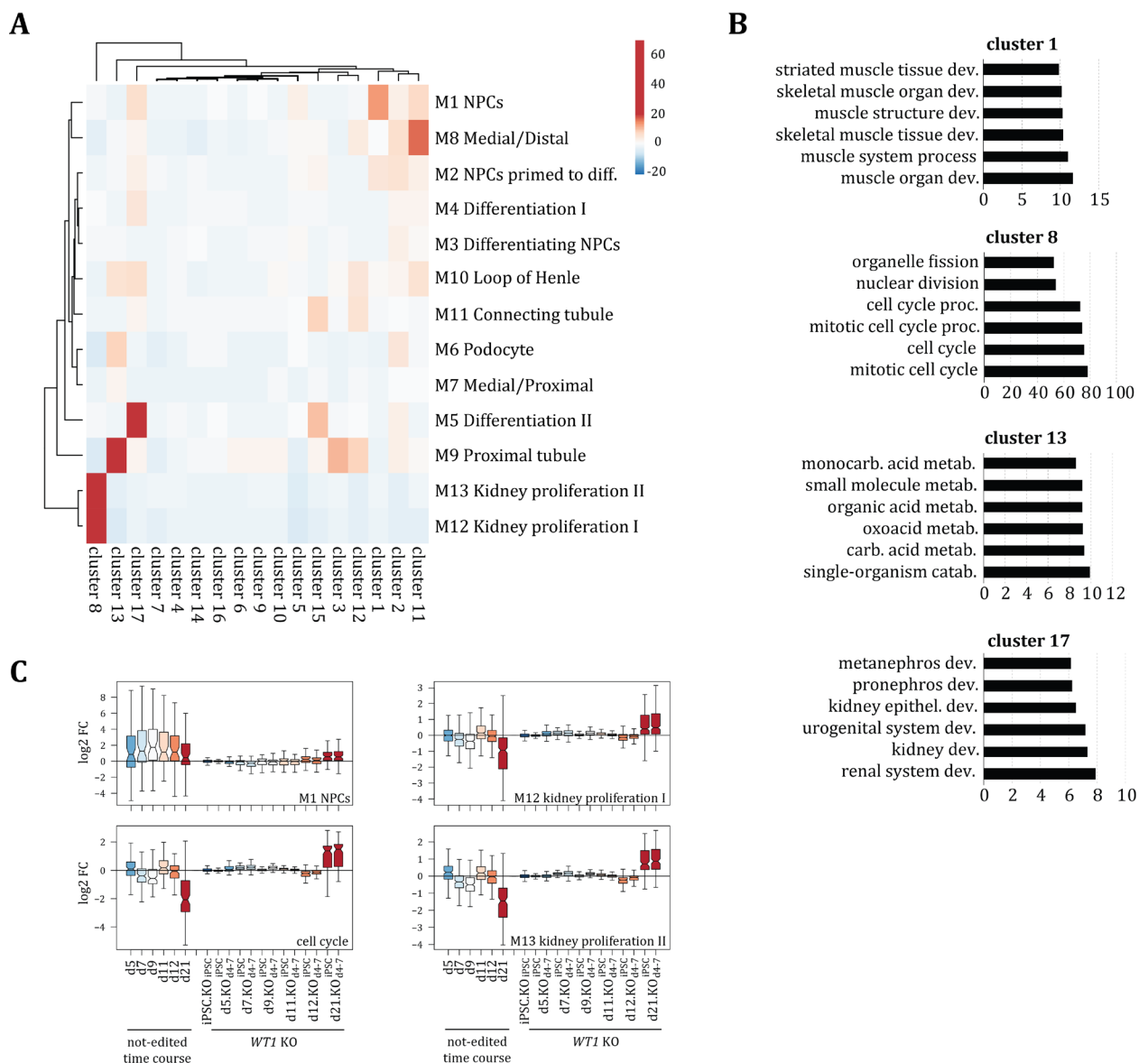


Figure 18. Deregulated genes upon *WT1* KO overlap with gene sets that define fetal kidney cell types.

A: Gene set overlap significance scores (see Methods for details) of our gene clusters with fetal kidney cell types defined in Lindström et al. (2018b). Shown are z-scores. diff = differentiate

B: Top six GO term enrichments of gene clusters 1, 8, 13 and 17 are shown.

Dev. = development; proc. = process; metab. = metabolism; catab. = catabolism

C: Quantification of log₂ FCs of indicated gene sets in contrasts shown in Fig. 17C. Left: differentiation time course; Right: cell state differences *WT1* KO relative to not-edited samples. “cell cycle” combines G₁S and G₂M data derived from Liu et al. (2017), also see Fig. 19.

Cluster 8 strongly overlapped with gene sets associated with kidney proliferation (M12 Kidney proliferation I and M13 Kidney proliferation II), and GO terms associated with cluster 8 were strongly enriched for processes implicated in cell cycle and nuclear division (Fig. 18A/B). Since cluster 8 was unchanged until d12 and got downregulated by d21 upon differentiation of not-edited cells, we suppose that this may correspond to a halt in proliferation at the onset of terminal differentiation. In contrast, both, genes associated with cluster 8 and with M12 and M13 were

strongly upregulated in *WT1* KO relative to not-edited d21 organoids (Fig. 17D; 18C). Of note, cluster 8 contained *Mki-67*, the gene encoding Ki-67. Since we detected a large proportion of SIX2-Ki-67 double-positive cells (Fig. 13C), we surmise that upregulation of cluster 8 genes in d21 *WT1* KO organoids is linked to NPC over proliferation.

In contrast, cluster 13 overlapped with gene sets associated with kidney differentiation (M9 Proximal tubule, M6 Podocyte and M10 Loop of Henle cell types), and was enriched for processes related to tubular transport in GO analysis (Fig. 18A/B). Finally, cluster 17 genes overlapped with gene sets associated with broader proximal and distal differentiation (M4 Differentiation I and M5 Differentiation II) and weakly with M1 NPCs and M10 Loop of Henle. GO terms of cluster 17 were highly enriched in processes related to embryonic kidney development, suggesting that it contains genes specific to intermediate kidney development (Fig. 18A/B). Indeed, cluster 17 was temporarily downregulated in *WT1* KO relative to not-edited samples, but unchanged at d21 (Fig. 17C/D). Notably, it contained *LHX1*, for which we detected a similar delayed expression pattern via qPCR (Fig. 15C).

Overall, these findings are consistent with the PCA results and suggest that *WT1* KO organoids at d21 are developmentally delayed compared to wildtype (not-edited). Likewise, they support our primary characterization of *WT1* KO organoids that showed loss of mature kidney structures, maintenance of SIX2 expression and increased cell proliferation (Fig. 13; 14). We can therefore conclude that loss of *WT1* leads to an overgrowth of progenitor cells at the expense of differentiation in kidney organoids.

We decided to further validate the cell type-specificity of our gene clusters by visualizing their expression in t-distributed stochastic neighbor embedding (t-SNE) maps of scRNA-seq data of week 16 human fetal kidney by Hochane et al. (2019) (Fig. 19A).

Like this, we confirmed expression of cluster 13 in a cluster of cells that co-expressed the M9 Proximal tubule gene set, and to a lesser extent in cells co-expressing the M6 Podocyte and M10 Loop of Henle gene sets. Cluster 17 genes were co-expressed in a cell cluster with the M5 Differentiation II gene set, which comprises genes involved in early proximal tubule differentiation.

As described before, cluster 8 genes overlapped with a gene set connected to proliferation, and GO terms of cluster 8 genes were enriched for processes related to cell division (Fig. 18A/B). Notably, we found a striking co-expression of M13 Kidney proliferation II and M12 Kidney proliferation I genes with G_1S and G_2M genes (Liu et al., 2017), respectively. Indeed, when combined as “cell cycle” genes they showed very similar expression patterns as M13 and M12 gene sets and were upregulated in *WT1* KO d21 organoids, further supporting the association of cluster 8 with proliferation (Fig. 18C).

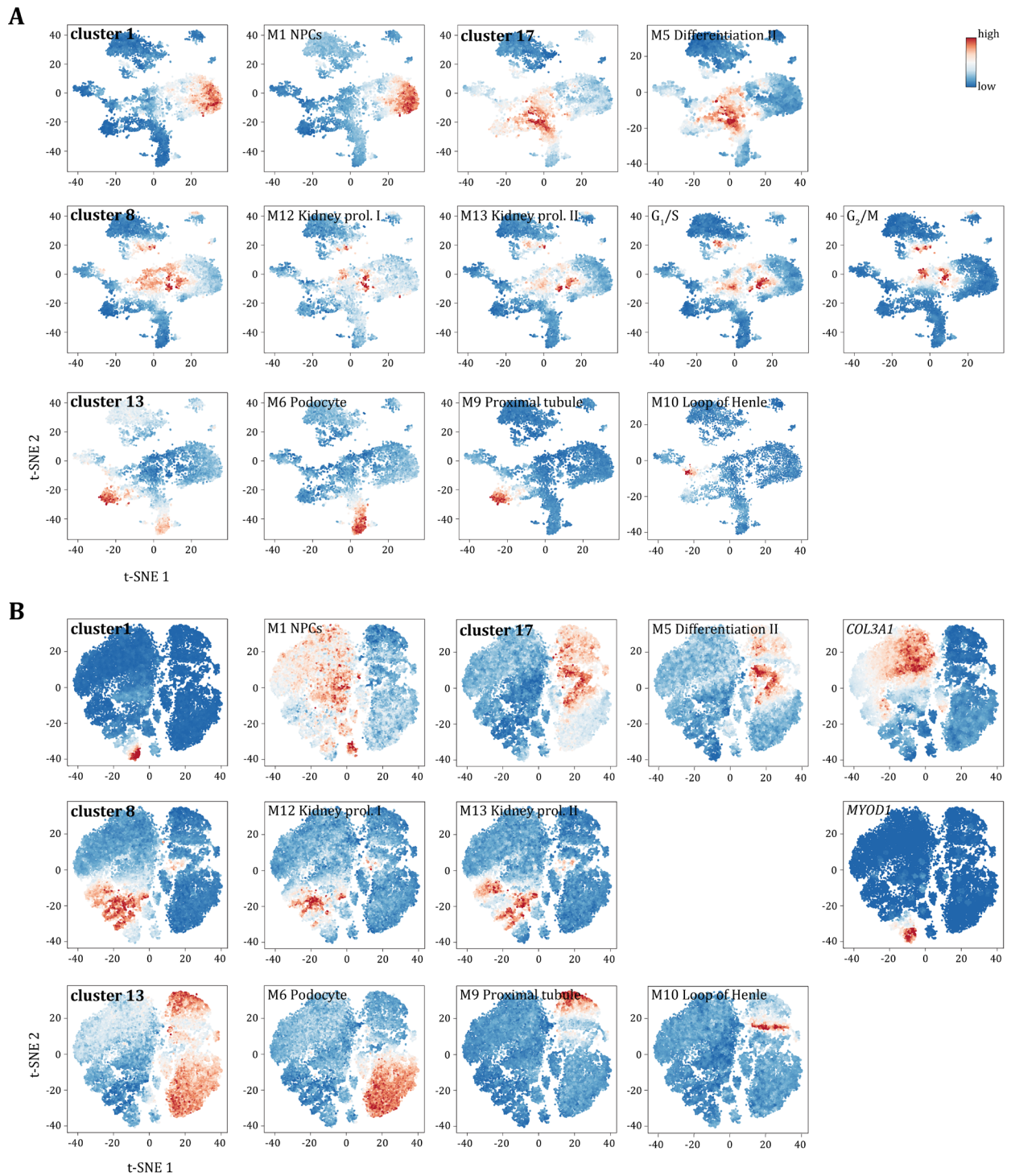


Figure 19. Gene clusters 1, 8, 13, and 17 are linked to NPCs, proliferation and kidney differentiation.

A+B: t-SNE maps of scRNA-seq data from week 16 human fetal kidney by Hochane et al. (2019) **(A)**, and d26 organoids generated with the Morizane protocol by Wu et al. (2018) **(B)**. Expression levels of indicated gene sets or genes are color-coded. G₁S and G₂M data is derived from Liu et al. (2017).

M12 Kidney prol. I = M12 Kidney proliferation I; M13 Kidney prol. II = M13 Kidney proliferation II

As expected, cluster 1 was enriched in a cell cluster also expressing the M1 NPCs gene set. As mentioned above, cluster 1 contained both, key NPC transcription factors (*SIX1*, *SIX2*, *EYA1* or *MEOX1*) and muscle-specifying transcription factors (*MYOD1* and *MYOG*). Kidney and skeletal muscle are derived from intermediate and paraxial mesoderm, respectively, which are specified in close proximity during embryonic development. Therefore, it is possible, that directed differentiation from iPSCs into NPCs produces muscle cells as a byproduct. Indeed, scRNA-seq of d26 organoids generated with our protocol identified off-target cell populations expressing muscle and neuronal genes (Wu et al., 2018).

To further elucidate this, we visualized our gene clusters in t-SNE maps derived from scRNA-seq of the aforementioned d26 organoids (Fig. 19B). We found co-expression of cluster 8 with M12 and M13, and of cluster 13 with M6 and M9 gene sets. However, the M1 NPCs signature was diffusely spread and not confined to precise cell populations in this data set. In fact, these genes were co-expressed with *COL3A1*, a marker for mesenchymal cells. In addition, we were unable to detect *SIX2* expression in this data set. Collectively, this indicates, that d26 kidney organoids are devoid of progenitor cells with canonical NPC transcription programs. This is consistent with our own IF and flow cytometry results which showed the absence of *SIX2*-positive cells in not-edited d21 organoids (Fig. 12D/E; 13C; 14A). In the absence of NPC-specific expression we now found that cluster 1 genes are enriched in a cluster of cells that also expressed *MYOD1*, confirming the aforementioned GO terms (Fig. 19B).

Taken together, *WT1* KO cells failed to upregulate podocyte and proximal tubule-specific genes (cluster 13), while they maintained progenitor programs (cluster 1) and elevated proliferation (cluster 8). Cluster 1 was transiently up- and then downregulated in not-edited differentiation, contained canonical NPC genes, and overlapped with NPC populations in fetal kidney data sets. However, its expression peaked at d7, whereas canonical M1 NPCs genes tended to peak at d9, and relative to not-edited cells, cluster 1 was upregulated upon *WT1* KO already from d9 onwards. Since these observations were not statistically significant, it remains to be determined whether cluster 1 represents genes that operate earlier than canonical NPC regulators.

3.6.4 Transcriptional changes in *WT1* KO organoids are conserved in Wilms tumor patients

Finally, we sought to clarify whether upregulation of muscle markers and the general transcriptional changes in *WT1* KO organoids were artifacts of *in vitro* organoid differentiation or recapitulated Wilms tumorigenesis. We therefore compared transcriptional changes in d21 KO organoids with alterations in patient tumors.

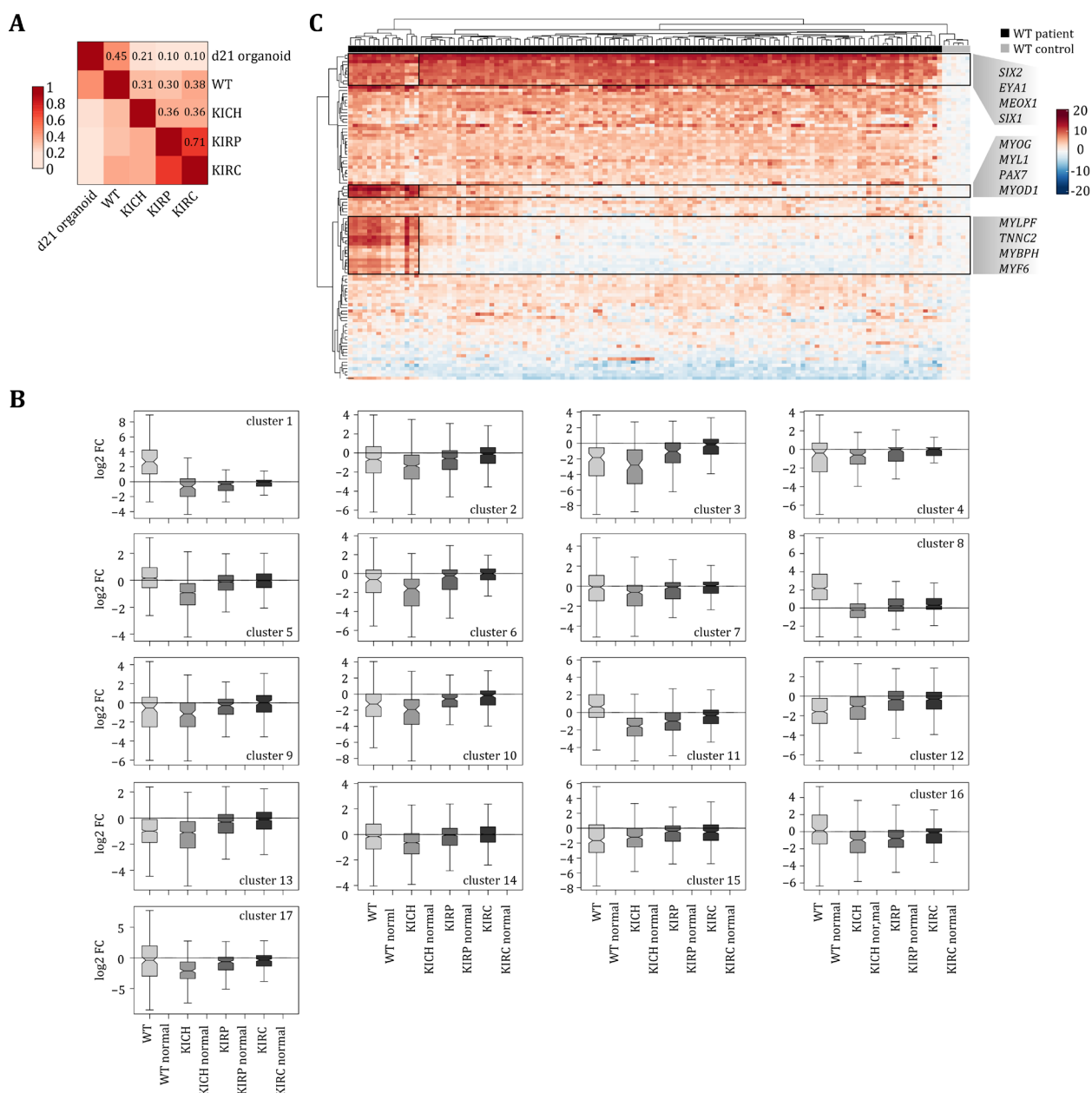


Figure 20. WT1 KO organoids resemble human Wilms tumor.

A: Pearson’s correlation coefficients of pairwise comparisons between mean log₂ FCs of KO^{iPSC} and KO^{d4-7} d21 organoids relative to not-edited d21 organoids (=d21 organoid), and kidney cancer patient samples relative to corresponding normal tissue, for 7,653 transcripts shown in **Fig. 17B**. WT = Wilms tumor; KICH = kidney chromophobe carcinoma; KIRP = kidney papillary carcinoma; KIRC = kidney clear cell carcinoma

B: Quantification of log₂ FCs of genes in clusters 1-17 in patient samples derived from WT, KICH, KIRP and KIRC, each relative to corresponding normal tissue.

C: Unsupervised clustering of cluster 1 gene log₂ FCs in Wilms tumor patient samples relative to normal tissue. Clusters containing nephron progenitor genes or muscle genes are highlighted. WT = Wilms tumor “normal” refers to corresponding normal tissue for each of the tumors

For this, we used profiling of Wilms tumors and corresponding normal tissues, and included kidney chromophobe carcinomas (KICH; Davis et al., 2014), kidney papillary cell carcinomas (KIRP; The Cancer Genome Atlas Research Network, 2016), as well as kidney clear cell carcinomas (KIRC; Creighton et al., 2013) as controls (Fig. 20A/B).

Pairwise comparisons of transcriptional changes in our 7,653 selected genes (Fig. 17C) revealed that differences in d21 *WT1* KO organoids correlated strongest with alterations in Wilms tumor ($R=0.45$), but less with KICH ($R=0.21$) and KIRP and KIRC ($R=0.1$) patients. This indicates that *WT1* KO organoids most closely resembled Wilms tumor samples within the given set of kidney cancers. More specifically, deregulation of clusters 1 and 8 was conserved specifically in Wilms tumor patient samples with respect to both, directionality and magnitude, which indicates that these alterations are Wilms tumor-specific (Fig. 20B). In contrast, we observed downregulation of cluster 13 in all four kidney cancer types, particularly in KICH samples. Together, this indicates that *WT1* KO organoids recapitulate features common to kidney cancers, including a reduction of mature kidney cell types, and features specific to Wilms tumor, including the ectopic expression of NPC- and proliferation-specific genes.

We next performed unsupervised clustering of cluster 1 genes in Wilms tumor patient samples, and identified a group of genes containing progenitor markers like *SIX2*, *SIX1*, *EYA1*, and *MEOX1* that was upregulated in all samples. In addition, we found two groups of genes containing muscle-specific transcription factors and structural muscle genes like *MYOD1*, *MYOG*, *MYL1*, *TNNC2* and *PAX7* that were upregulated in only a subset of Wilms tumor patients (Fig. 20C). This suggests that acquisition or upregulation of muscle programs accompanies Wilms tumorigenesis in a subset of patients and that the elevation of muscle transcription in *WT1* KO kidney organoids recapitulates a Wilms tumor patient phenotype and not an organoid-specific phenomenon.

Collectively, transcriptional changes in *WT1* KO organoids reflect maintenance of NPCs at the expense of mature nephron cell types, elevated proliferation and upregulation of muscle-related transcription. These changes are conserved in Wilms tumor patients and support our phenotypic characterization by IF and flow cytometry.

3.7 Competition between *WT1* KO d9 NPCs and wildtype NPCs

Even though KO^{iPSC} and $\text{KO}^{\text{d4-7}}$ cells showed very similar phenotypes in our KO time course experiment (Fig. 13; 14) and similar changes in gene expression by RNA-seq (Fig. 17C/D), we still wondered why they displayed such profound differences in organoid growth behaviors (Fig. 13D). We hypothesized that maybe the difference in *WT1* KO efficiency and thus the frequency of residual wildtype or heterozygous cells in the bulk population might influence the prevalence of cell death versus proliferation. At the same time, we wondered whether such highly proliferative cells like the $\text{KO}^{\text{d4-7}}$ cells could outcompete wildtype cells in a mixing experiment.

To answer both questions, we mixed RFP-expressing KO^{iPSC} and $\text{KO}^{\text{d4-7}}$ d9 NPCs with d9 NPCs generated from a green fluorescent protein (GFP)-expressing wildtype iPSC line in different ratios to obtain chimeric organoids (Fig. 21A). A mix of 90% KO^{iPSC} NPCs with 10% wildtype NPCs (=90% input) would roughly mimic the frequency of unedited cells in $\text{KO}^{\text{d4-7}}$ organoids. On the other hand, if we mixed 10% of $\text{KO}^{\text{d4-7}}$ NPCs with 90% of wildtype NPCs, we could investigate if small fractions of *WT1* KO cells were able to outgrow their wildtype counterparts.

First, we recorded organoid growth. As before, KO^{iPSC} -only organoids stayed very small, whereas GFP-only organoids grew as expected (Fig. 21B, left). Chimeric KO^{iPSC} /wildtype organoids grew bigger with increasing input of GFP-expressing wildtype NPCs. However, only addition of 90% wildtype cells could rescue the growth phenotype of KO^{iPSC} organoids towards GFP-only levels. This indicates that increased cell death and reduced growth in KO^{iPSC} organoids is intrinsic and cannot be rescued by simply increasing the fraction of *WT1* wildtype or heterozygous cells in a given organoid.

In contrast, when we mixed as little as 10% $\text{KO}^{\text{d4-7}}$ cells with 90% GFP-expressing wildtype cells, organoids grew larger than GFP-only organoids (Fig. 21B, right). In fact, organoid growth was very similar for all input fractions of $\text{KO}^{\text{d4-7}}$ cells, and did not increase much further with increasing $\text{KO}^{\text{d4-7}}$ input fractions. This indicates that $\text{KO}^{\text{d4-7}}$ cells have a growth advantage within a chimeric organoid.

We next quantified fractions of KO^{iPSC} and $\text{KO}^{\text{d4-7}}$ cells in single chimeric organoids at d21 and at d11 as our reference point (Fig. 21C). If KO cells and wildtype cells grew equally, we would expect equal fractions of KO cells at d11 and d21 (Fig. 21C; pink line). As expected this was the case for control not-edited cells, and surprisingly also for KO^{iPSC} cells, considering the reduced size of KO^{iPSC} /wildtype organoids. In contrast, fractions of $\text{KO}^{\text{d4-7}}$ cells increased strongly between d11 and d21. For the 10% input, the percentage of $\text{KO}^{\text{d4-7}}$ cells increased from 7% measured in d11 organoids to 30.5% measured in d21 organoids, indicating a proliferative advantage of $\text{KO}^{\text{d4-7}}$ cells compared to wildtype cells during organoid culture (Fig. 21C).

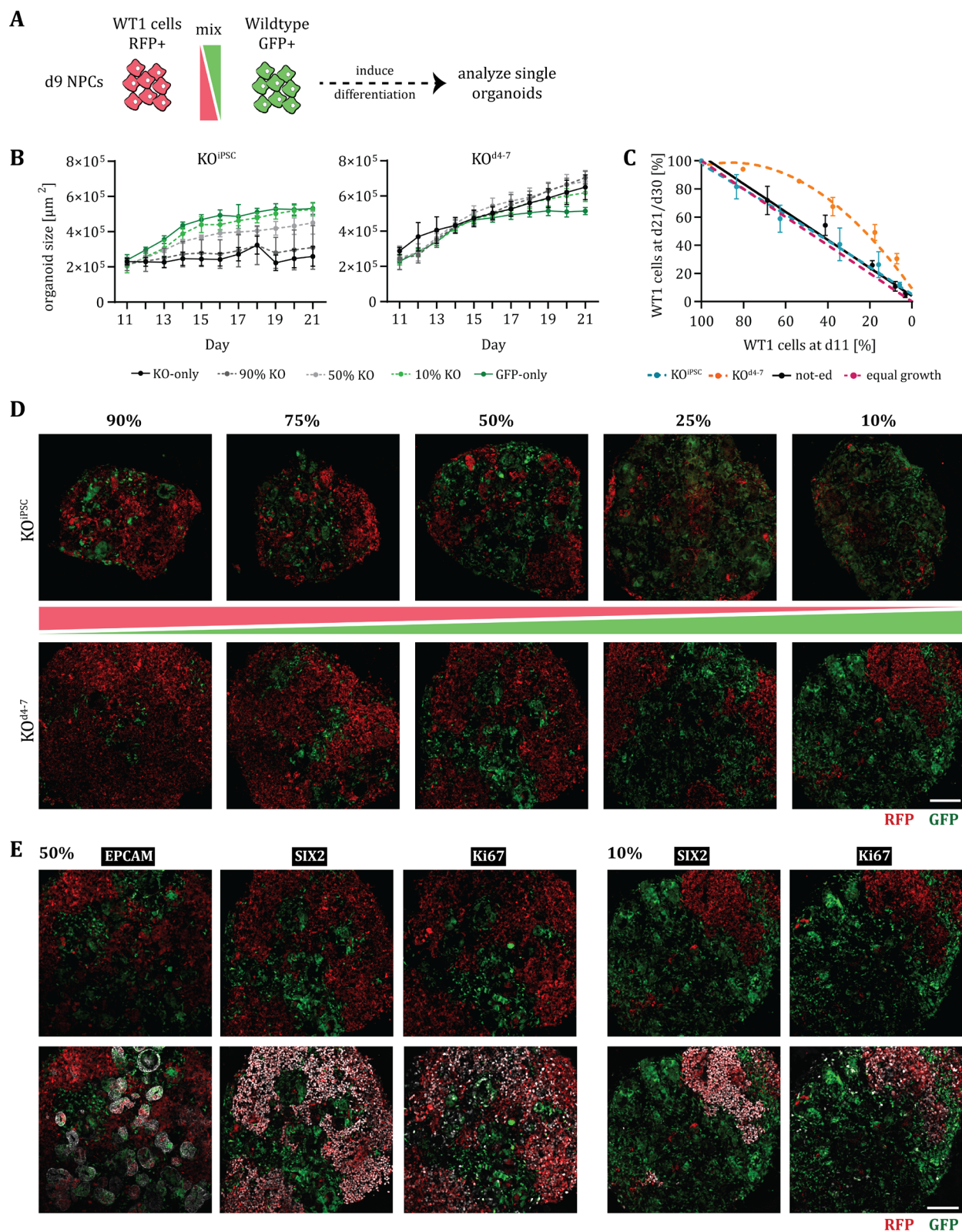


Figure 21. NPCs derived from KO^{d4-7} cells outcompete wildtype NPCs during organoid growth.

A: Experimental procedure.

B: Growth of chimeric organoids obtained from mixing different ratios of d9 NPCs from WT1 cells (KO^{iPSC} (left) and KO^{d4-7} (right)) with d9 NPCs from GFP-expressing wildtype cells. Values in μm^2 are derived from Incucyte® images and are presented as mean \pm SD for each n=12 organoids.

Results

C: Flow cytometry-based quantification of WT1 cells in single chimeric d21 organoids as in **B**. Percentages of KO^{iPSC} and KO^{d4-7} cells at d21 are plotted against respective values at d11. Values derived from not-edited cells at d30 were plotted as a control. For easier visualization, we used a linear fit for not-edited and KO^{iPSC} samples and a quadratic fit for KO^{d4-7} samples. Pink line = theoretical outcome assuming equal growth. Data is shown as mean % +/- SD for a minimum of n=3 organoids per mixing ratio from one experiment.

D: Confocal microscopy of chimeric d21 organoids as in **B**. WT1 cells are represented by RFP, wildtype cells are represented by GFP. Percentage values reflect % of WT1 cells as input. Scale bar: 100 μ m

E: IF staining for the indicated markers in d21 organoids derived from mixing 50% (left) and 10% (right) KO^{d4-7} NPCs (represented by RFP) with GFP expressing wildtype NPCs. Scale bar: 100 μ m

Note that "WT1 cells" refers to WT1 not-edited, KO^{iPSC} and KO^{d4-7} cells (see Methods for details) as indicated.

We also performed confocal microscopy on cryosections of d21 organoids. In agreement with our single-organoid flow cytometry results, we found a striking expansion of KO^{d4-7} but not of KO^{iPSC} cells (shown by RFP signal) in organoids of the same input ratio (Fig. 21D). We also stained sections from KO^{d4-7} chimeric organoids for SIX2, Ki-67 and EPCAM. Similar to what we saw in KO organoids beforehand, both *WT1* KO cells and GFP expressing wildtype cells contributed to EPCAM-positive structures of the organoid. In contrast, we found a large fraction of SIX2 expressing cells confined to RFP expressing *WT1* KO cells and absent from GFP expressing cells (Fig. 21E). This together with the EPCAM staining, suggests, that wildtype GFP NPCs were not compromised in their ability to differentiate despite the presence of *WT1* KO cells in their immediate proximity. Finally, both cell populations contained Ki-67-positive cells, which, however, were enriched in *WT1* KO cells.

Collectively, these results show that addition of wildtype cells to KO^{iPSC} cells, which mimics a lower KO efficiency, did not rescue the observed growth phenotype of KO^{iPSC} organoids. This suggests that KO^{iPSC} cells might be intrinsically distinct from KO^{d4-7} cells, which generate much bigger organoids. However, further experiments are required to solve the discrepancy between reduced organoid growth and stable fractions of KO^{iPSC} and wildtype cells over time during organoid formation. Nevertheless, it is clear that KO^{d4-7} cells were able to outgrow wildtype cells in this competition experiment, presumably due to their differentiation arrest in a SIX2-expressing, proliferative cell state. Notably, *WT1* KO cells did not affect the differentiation capacity of wildtype NPCs within a given organoid.

3.8 Functional properties of *WT1* KO organoid-derived cells

Until this point, we have shown that *WT1* KO results in loss of nephron structures, maintenance of SIX2-expressing cells and elevated proliferation. KO^{d4-7} cells can also outgrow wildtype cells when mixed during organoid formation. In addition, transcriptional changes found in *WT1* KO organoids are conserved in Wilms tumor patient samples.

However, these descriptive analyses do not exclude the possibility that SIX2-expressing *WT1* KO cells persisted due to a developmental delay in the organoid system and not due to malignant transformation. Functional properties of tumor cells include their ability to self-renew and to propagate when transplanted into physiological environments, which can be demonstrated by unrestricted growth in PDTX models. We therefore decided to evaluate these features in KO^{d4-7} cells using our kidney organoid system as an *in vitro* surrogate for tumor cell passaging and for tumor transplantation into mice.

3.8.1 Serial passaging of KO^{d4-7} cells derived from d21 organoids with wildtype d9 NPCs

First, we sought to assess whether cells of a “mature” KO^{d4-7} d21 organoid could be maintained and propagated for several passages when mixed with wildtype d9 NPCs in a developmental context. For this, we dissociated KO^{d4-7} d21 organoids into single cells, aggregated them with wildtype GFP-expressing d9 NPCs at different ratios, and induced organoid formation according to the original protocol, including supplementation of CHIR and FGF9 (Fig. 22A; 3A). We repeated this for up to four passages (60 days). After each passage, we harvested a subset of organoids for flow cytometry analysis and IF staining, and dissociated the remaining organoids for the next passage.

To begin with, we quantified KO^{d4-7} and control not-edited cells derived from d21 organoids (together named WT1 cells, see Methods) after one passage (p) with wildtype d9 NPCs (p1). As expected, cells derived from not-edited d21 organoids were diminished compared the respective input fractions, while cells from KO^{d4-7} d21 organoids expanded (Fig. 22B, top). In addition, we measured SIX2-expressing cells and detected only minor fractions of SIX2-expressing cells within the not-edited population of chimeric organoids (Fig. 22B, bottom). This is consistent with only 1.6% SIX2-positive cells present in the original not-edited d21 organoids (p0), which were maintained in p1. This indicates that loss of SIX2 and downregulation of cell proliferation in not-edited organoids are largely irreversible.

In contrast, original KO^{d4-7} d21 organoids (p0) contained 31% SIX2-positive cells and we found large fractions of SIX2-positive KO^{d4-7} cells in chimeric organoids after p1 (Fig. 22B, bottom). For

high input ratios (100%, 90% and 75%), percentages of SIX2-positive cells increased to around 55% in all three cases. On the one hand, this suggests that SIX2-positive cells expanded more within the 75% input condition compared to the 90% and 100% conditions. On the other hand, this also implies a maximum fraction of SIX2-positive cells that can be tolerated within a chimeric organoid, at least under the present conditions. For low input ratios of 10% and 5%, SIX2-positive KO^{d4-7} cells dropped to around 15% and 8.5%, respectively. Considering the dilution factors, this still represented a strong expansion of SIX2-positive cells from 3.1% to 15% (10% of p0) and from 1.55% to 8.5% (5% of p0) in these conditions. This indicates that SIX2-positive cells from KO^{d4-7} d21 organoids expanded upon passaging with wildtype NPCs in growth-promoting, developmental conditions.

Next, we performed serial passaging of KO^{d4-7} cells with wildtype GFP-expressing d9 NPCs (derived from a single differentiation batch) at different ratios. We found surprisingly stable fractions of KO^{d4-7} cells over four passages which correlated with the respective input ratios: For 90% input of KO^{d4-7} cells we detected around 90% of KO^{d4-7} cells after p1, p2, p3 and p4 (Fig. 22C, left). With some fluctuations, this was true for all input ratios, except the 10% input, where KO^{d4-7} cells seemed to expand further in p3 and p4. Stable fractions indicate that the respective KO^{d4-7}-derived input population from the previous passage and differentiating wildtype NPCs proliferated at a similar rate. Notably, due to passaging of entire chimeric organoids, we inevitably co-passaged wildtype cells.

Interestingly, when we measured SIX2-expressing cells within the KO^{d4-7} population, we found dynamics that were dependent on the input ratios: in organoids formed predominantly by KO^{d4-7} cells (ratios of 100%, 90% and 75%), the percentages of SIX2-expressing cells increased in p1 and decreased on average 1.7-, 1.3- and 1.4-fold, respectively, upon further passaging (Fig. 22C, right and not shown). In organoids formed predominantly by wildtype NPCs, percentages of SIX2-expressing cells stayed constant over four passages (ratio of 25%), or dropped at p1 and stayed constant upon further passaging (ratios of 10% and 5%). When considering the dilution factors, this implies a substantial expansion of SIX2-expressing cells over four passages: for the 25%, 10% and 5% input ratios, the fractions of SIX2-expressing cells increased 4-, 10- and 12-fold on average in each passage, respectively. Notably, the entire population of KO^{d4-7} cells similarly increased 3.7-, 12- and 10-fold on average in each passage in the aforementioned input conditions, indicating that population growth does not solely result from an expansion of SIX2-positive cells. It, therefore, remains to be determined if SIX2-positive cells on top of a tissue hierarchy give rise to SIX2-negative cells or if additional cell types present in the input population, like stromal cells, contribute to the expansion of KO^{d4-7} cells.

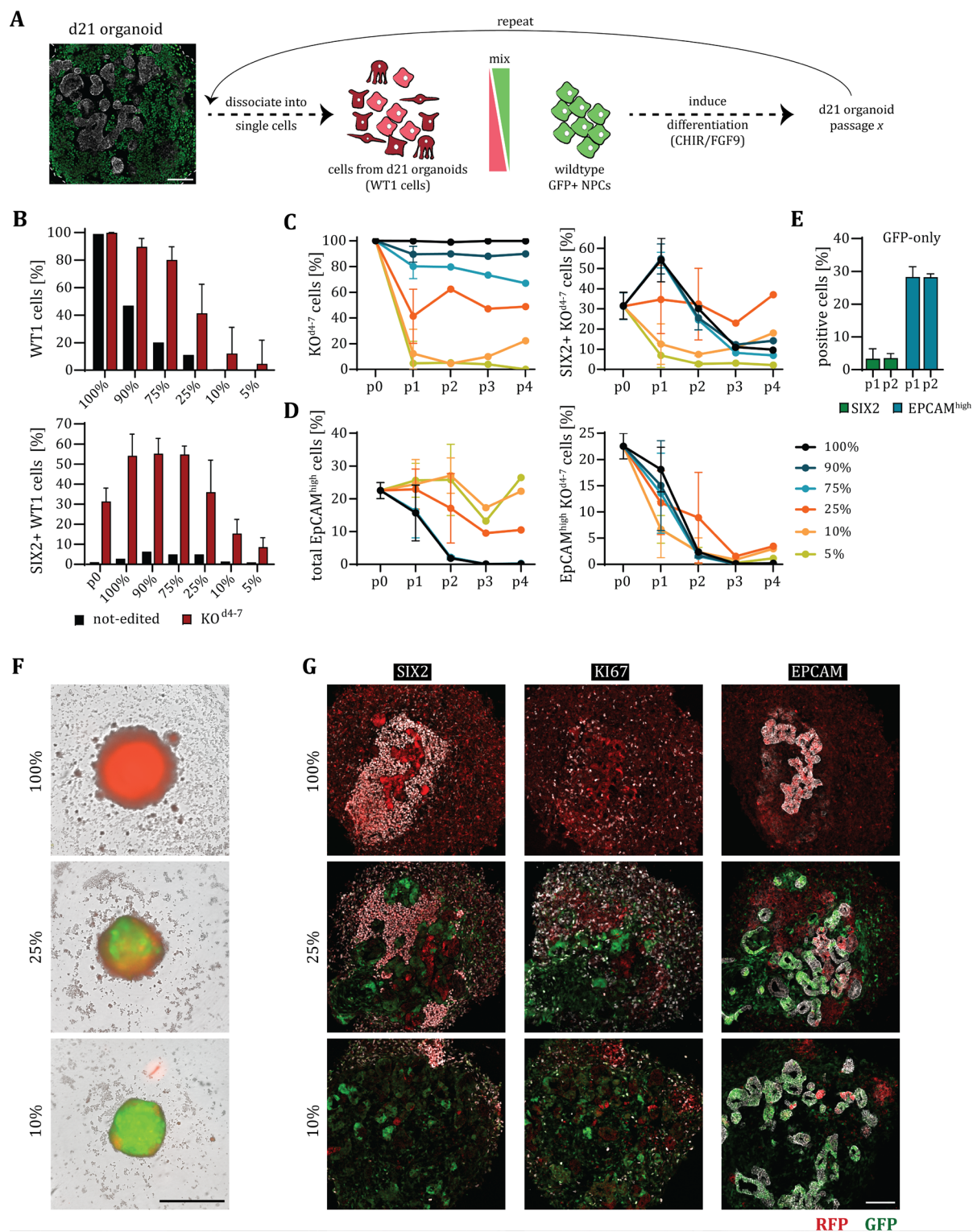


Figure 22. SIX2-expressing cells from KO^{d4-7} d21 organoids can be maintained for several passages in the presence of wildtype NPCs.

A: Experimental procedure; Scale bar: 100 μ m

B: Percentages of WT1 cells (top) and SIX2-positive WT1 cells (bottom) in chimeric organoids after passaging not-edited or KO^{d4-7} cells derived from d21 organoids with wildtype GFP d9 NPCs (p1). Percentages on the x-axis reflect input fractions of WT1 cells. Data is shown as mean \pm SD for n=2 independent experiments.

Results

C+D: Percentages of KO^{d4-7} cells and SIX2-positive KO^{d4-7} cells (**C**), and of total EPCAM^{high} cells and EPCAM^{high} KO^{d4-7} cells (**D**) in chimeric organoids after p1 to p4 of passaging KO^{d4-7} cells derived from d21 organoids with wildtype GFP d9 NPCs. Input ratios of KO^{d4-7} cells are indicated. Data is shown as mean +/- SD from n=1 or 2 independent experiments.

E: Percentages of SIX2 and EPCAM^{high} cells upon culture of GFP-expressing d9 NPCs alone. Data is shown as mean +/- SD from n=2 independent experiments. Note that GFP-expressing NPCs used in p1 to p4 were derived from the same differentiation batch.

F: Images of endpoint organoids derived from passaging RFP-expressing KO^{d4-7} cells from d21 organoids with GFP-expressing d9 NPCs. Images were recorded using an Incucyte® microscope. Shown are images derived from input fractions of 100%, 25%, and 10% KO^{d4-7} cells after p2. Scale bar: 1 mm

G: IF staining for indicated markers in endpoint organoids as in **F**. KO^{d4-7} cells are represented by RFP, wildtype cells are represented by GFP. Scale bar: 100 μ m

Note that “WT1 cells” refers to WT1 not-edited and KO^{d4-7} cells (see Methods for details).

p0 corresponds to original d21 organoids that were dissociated for passaging.

+ = positive

Collectively, it appears that a minimum fraction of wildtype cells is required to maintain SIX2-expressing cells over passages. Based on these experiments, an input fraction of 25% KO^{d4-7} cells was the maximum tolerable input to maintain constant fractions of SIX2-positive cells derived from KO^{d4-7} organoids. This indicates that interactions with wildtype NPCs and/or their differentiated offspring affect the cell type composition of the *WT1* mutant cell population upon passaging.

We also noted a pronounced decline in the frequency of EPCAM^{high} cells within the KO^{d4-7} population over four passages (Fig. 22D, right). We believe that EPCAM^{high} cells in the first two passages are due to carry over from previous passages, indicating that loss of SIX2 was not due to overt differentiation of passaged KO cells. Notably, when we quantified total fractions of EPCAM^{high} cells, we found a complete loss for high input ratios of 100%, 90% and 75% until p3, which indicates that also wildtype NPCs failed to generate EPCAM^{high}-expressing tubules (Fig. 22D, left). However, this was not accompanied by maintenance of SIX2 expression in wildtype cells (not shown). For lower input ratios of 25%, 10% and 5% we detected EPCAM^{high} cells across all passages, which is consistent with differentiation of GFP-expressing wildtype NPCs into EPCAM^{high} cells. Notably, wildtype GFP NPCs in isolation efficiently gave rise to EPCAM^{high} cells, supporting the general ability of this NPC batch to differentiate properly (Fig. 22E). Taken together, this suggests that the microenvironment created by high input ratios of KO^{d4-7} cells interfered with proper differentiation of wildtype NPCs.

In order to confirm our flow cytometry analysis, we performed IF staining for EPCAM, SIX2 and Ki-67 in p2 organoids derived from the 100%, 25% and 10% KO^{d4-7} input conditions (Fig. 22G).

In agreement with our flow cytometry data, the majority of EPCAM-positive tubular structures in the 25% and 10% conditions co-expressed GFP, and were thus derived from “host” NPCs (Fig. 22G). Only a minority of tubules co-expressed RFP and was thus derived from KO^{d4-7} cells. We nevertheless observed few EPCAM-positive tubular aggregates in p2 organoids derived from 100% KO^{d4-7} cells. These structures were surrounded by highly SIX2-positive cells, whereas the

rest of the organoid contained only a few weakly SIX2-positive cells. In organoids derived from the 25% and 10% dilutions, SIX2 staining overlapped with RFP, but was absent from GFP-expressing cells.

Based on the maintenance of SIX2-positive cells over four serial dilutions in the 25% and 10% conditions, we expected to observe Ki-67-staining to be enriched in KO^{d4-7} cells of the organoid. Indeed, we observed focal enrichments of Ki-67-positive cells within the RFP-positive population of p2 chimeric organoids, especially for the 25% input condition (Fig. 22G). Similarly, we measured an enrichment of Ki-67-RFP double-positive cells in KO^{d4-7} cells over time via flow cytometry in this condition (not shown). Interestingly, Ki-67 was not particularly enriched within areas of highly SIX2-positive cells of p2 organoids derived from 100% KO^{d4-7} cells. Likewise, Ki-67 fractions in this condition declined towards p4 (not shown).

Collectively, SIX2-positive cells derived from KO^{d4-7} d21 organoids expanded over several passages in a developmental environment of differentiating wildtype cells and withstood differentiation-promoting cues. This, however, seemed to require a minimum of 50-75% wildtype NPCs within the chimeric organoids. Below this frequency, mutant SIX2-positive cells were lost and “host” NPCs were impaired to differentiate into EPCAM-positive tubules. Therefore, we surmise that SIX2-positive cells on the one hand depend on signals from wildtype cells (niche) in order to grow and, on the other hand, emit differentiation-inhibiting signals that affect wildtype cells.

3.8.2 Transplantation of organoid-derived KO^{d4-7} cells into wildtype organoids

Having shown that cells derived from KO^{d4-7} d21 organoids can be propagated in the presence of wildtype NPCs over several passages, we decided to assess the behavior of those cells in a differentiated context. To mimic a scenario that more closely recapitulates transplantation of tumor cells in PDTX models, we decided to take advantage of differentiated organoids as a substrate for passaging. With this approach, we aimed to assess whether *WT1* KO cells could be transplanted and propagated both, in the presence and absence of growth factors.

3.8.2.1 Transplantation in the presence of growth factors

We dissociated RFP-expressing KO^{d4-7} d21 organoids into single cells and added them to d21 organoids derived from GFP iPSCs (see above) that we injured by mechanically breaking them apart (Fig. 23A). We estimated d21 organoids to contain around 150,000 to 200,000 cells to which we added either 12,500 or 25,000 cells, corresponding to a ratio of roughly 10-20%.

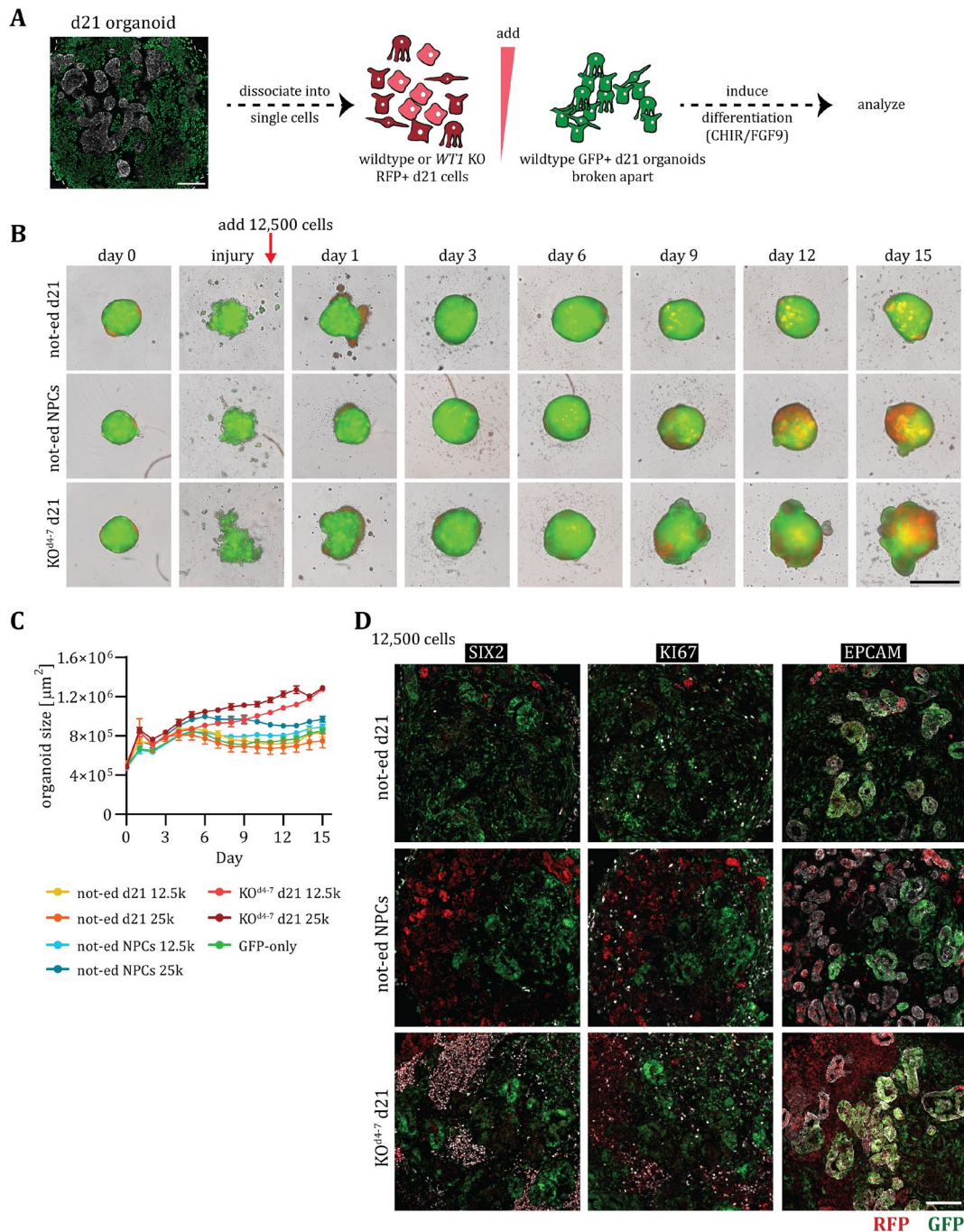


Figure 23. *SIX2*-expressing KO^{d4-7} cells from d21 organoids expand within wildtype organoids in the presence of growth factors.

A: Experimental procedure; scale bar: 100 μm

B: Images of organoids after adding 12,500 RFP-expressing cells from not-edited d21 organoids (not-ed d21, top), not-edited d9 NPCs (not-ed NPCs, middle), or KO^{d4-7} d21 organoids (KO^{d4-7} d21, bottom) to injured wildtype GFP organoids. Images recorded at indicated time points on an Incucyte® system. Scale bar: 1mm

C: Growth of organoids obtained after adding 12,500 (12.5k) or 25,000 (25k) RFP-expressing cells as in **B** to injured wildtype GFP organoids. Values in μm^2 are derived from Incucyte® images and are presented as mean \pm standard error of the mean (SEM) for $n=8$ organoids per condition.

D: IF staining of the indicated markers in endpoint organoids after adding 12,500 RFP-expressing cells as in **B** to injured wildtype GFP organoids. Scale bar: 100 μm

After adding the cells, we performed organoid culture under differentiation- and growth promoting conditions according to the original protocol, including supplementation of CHIR and FGF9 (Fig. 3A). In addition to KO^{d4-7} cells, we also included cells dissociated from not-edited d21 organoids as well as not-edited d9 NPCs as controls. We recorded organoid growth, imaged the developing chimeric organoids and collected endpoint organoids after 15 days for IF staining.

Cells from KO^{d4-7} d21 organoids expanded visibly and induced organoid overgrowth (Fig. 23B, bottom; 23C). Consistent with this, we found large areas of RFP-expressing cells in these organoids that frequently co-stained for SIX2 (Fig. 23D, bottom). We also found an enrichment of Ki-67-positive cells in these areas but only few EPCAM-positive tubules. EPCAM-positive tubules mainly co-expressed GFP, which suggests that they re-formed after the mechanical injury.

In contrast, cells derived from not-edited d21 organoids did not expand (Fig. 23B, top; 23C) and we found only very few RFP-positive not-edited cells in corresponding chimeric organoids (Fig. 23D, top). Likewise, only very few EPCAM-positive tubules co-expressed RFP, but instead were-positive for GFP. Importantly, we barely detected any SIX2-positive cells and normal frequencies of Ki-67-positive cells in these organoids. This indicates that cells derived from not-edited d21 organoids contributed poorly to chimeric organoids and were not able to expand despite growth-promoting signals.

It is therefore possible, that organoid overgrowth is a consequence of the integration efficiency rather than the transformation of KO^{d4-7} d21 cells. However, when we added not-edited d9 NPCs to injured GFP organoids, we observed an increase in RFP fluorescence (Fig. 23B, middle; 23C), and found large areas of RFP-expressing cells in the chimeric organoids (Fig. 23D, middle), indicating successful integration of not-edited d9 NPCs. Likewise, we found EPCAM-positive tubules that co-expressed both, RFP and GFP, but only very few SIX2-positive cells. This suggests that not-edited d9 NPCs integrated well into differentiated wildtype organoids and themselves differentiated properly under the given conditions. In contrast to KO^{d4-7} d21 cells, differentiating NPCs induced neither organoid overgrowth nor a visible increase in Ki-67-positive cells (Fig. 23C; 23D, middle).

Collectively, these findings indicate that KO^{d4-7} cells but not not-edited cells derived from d21 organoids were able to expand upon transplantation into wildtype organoids. Importantly, KO^{d4-7} cells maintained SIX2 expression under these conditions.

It is possible, however, that supplementation of CHIR and FGF9 helped sustain SIX2-positive KO^{d4-7} cells within wildtype organoids. We therefore repeated this experiment and transplanted KO^{d4-7} cells into wildtype organoids without any additional growth factors.

3.8.2.2 Transplantation in the absence of growth factors

As before, we dissociated KO^{d4-7} d21 organoids into single cells and transplanted between 2,500 and 50,000 cells into injured GFP-expressing organoids, spanning input ratios of around 2% to 40% (see above) (Fig. 24A). This time, we kept chimeric organoids in culture medium without additional growth factors. As before, we recorded organoid growth, imaged the developing chimeric organoids and collected endpoint organoids after 13 days for IF staining.

Similar to culture under growth-promoting conditions, we observed a strong increase in organoid size during two weeks of culture (Fig. 24C). Organoid growth scaled with input cell numbers until up to adding 25,000 cells. Notably, even the addition of only 2,500 cells resulted in increased organoid growth compared to GFP-only control organoids. Similarly, we found a strong gain in red fluorescence over the course of the experiment, which also depended on the initial input cell numbers (Fig. 24B).

Importantly, we again found numerous SIX2-expressing colonies in endpoint organoids (Fig. 24D). These were located in direct vicinity to intact EPCAM-positive tubules that co-expressed GFP. This indicates that, like before, EPCAM-positive tubules of GFP organoids re-formed after their injury, and that RFP-expressing KO^{d4-7} cells were incorporated right into the organoid, as we would expect for a transplantation. Notably, we also detected some RFP-EPCAM double-positive tubules probably due to carry over from d21 organoids. In addition, we stained for Ki-67 and found it to be enriched within RFP-positive KO^{d4-7} cells of the chimeric organoids.

This suggests that KO^{d4-7} cells derived from d21 organoids are able to propagate and maintain SIX2 expression in the absence of growth factors when transplanted into wildtype organoids.

Taken together, our functional experiments show that organoids can be exploited as a surrogate for tumor cell transplantation into developmental (d9 NPCs) and differentiated (d21 organoids) tissue contexts, even in the absence of growth-promoting cues. We demonstrated sustained proliferation and maintenance of SIX2-expressing KO^{d4-7} cells derived from d21 organoids, and provide evidence that the host tissue signals to the *WT1* mutant cell population and influences cell type composition.

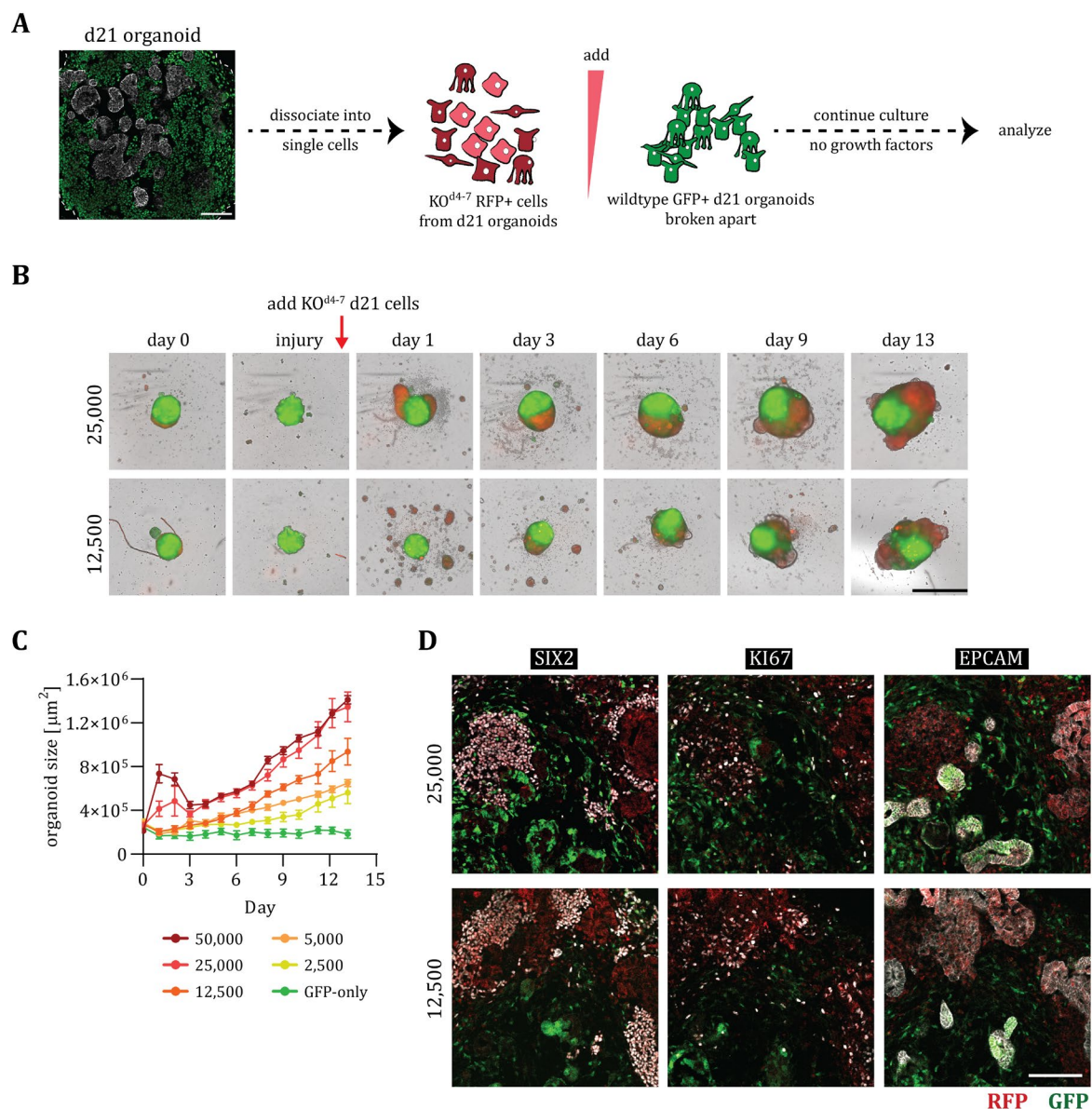


Figure 24. SIX2-expressing KO^{d4-7} cells from d21 organoids expand within wildtype organoids in the absence of growth factors.

A: Experimental procedure; scale bar: 100 μm

B: Images of organoids after adding 12,500 or 25,000 RFP-expressing KO^{d4-7} cells derived from d21 organoids to injured wildtype GFP organoids. Images recorded at indicated time points on an Incucyte® system. Scale bar: 1mm.

C: Growth of organoids obtained after adding the indicated numbers of RFP-expressing KO^{d4-7} cells derived from d21 organoids to injured wildtype GFP organoids. Values in μm^2 are derived from Incucyte® images and are presented as mean \pm SEM for n=8 organoids per condition.

D: IF staining of the indicated markers in endpoint organoids obtained after adding 12,500 and 25,000 RFP-expressing KO^{d4-7} cells derived from d21 organoids to injured wildtype GFP organoids. Scale bar: 100 μm

4. Discussion

Wilms tumor is a pediatric kidney cancer that is thought to arise from impaired nephrogenesis, leading to an expansion of fetal kidney cell types at the expense of mature kidney cells. However, it remains to be determined (a) how and at which stages genetic lesions induce transformation, (b) if and how cell types-of-origin transform into tumor propagating cell types, (c) how different perturbations converge on stable Wilms tumor subtypes, and (d) if such knowledge can inform therapeutic treatments. With the pre-existing models, it is challenging to study Wilms tumorigenesis.

Therefore, in this thesis, I evaluated four different Wilms tumor alterations, previously identified in patients, using hiPSC-derived kidney organoids: (1) overexpression of LIN28A and LIN28B as representatives of the miRNA processing pathway, (2) overexpression of the NPC transcription factor SIX2 and its mutant Q177R variant, (3) mimicking stabilization of β -catenin by chemical activation of canonical WNT signaling, and (4) loss of the tumor suppressor gene *WT1*.

4.1 Overexpression of LIN28 – divergent phenotypes in organoids and mice

Lin-28 was originally identified as a regulator of *C. elegans* development and has since been implicated in many cellular processes, including stem cell regulation and cancer. In fact, both LIN28 paralogs have been found to be involved in up to 20 different tumor types such as tumors of the gastrointestinal tract, neuroblastoma and Wilms tumor. LIN28 elicits most of its effects by regulating *let-7* miRNAs. LIN28A associates with pri-*let-7* in the nucleus, which prevents it from being processed by DROSHA, whereas LIN28B sequesters pri-*let-7* in the nucleolus. Both LIN28A and B are also able to bind pre-*let-7* in the cytoplasm, which on the one hand prevents further processing by DICER, and on the other hand leads to its oligo-uridylation and subsequent degradation by exonucleases, including DIS3L2 (reviewed in Balzeau et al., 2017; Tsalikas and Romer-Seibert, 2015).

It is quite evident that deregulated miRNA processing plays a pivotal role in Wilms tumor and that LIN28 regulates many miRNA processing steps which are executed by factors that are also implicated in Wilms tumor, including *DICER1*, *DROSHA*, *DGCR8* and *DIS3L2*.

Two previous studies in mice have interrogated the effects of transient and constitutive overexpression of LIN28B during kidney development (Urbach et al., 2014; Yermalovich et al., 2019). Driven by the *Wt1* locus, a pulse of LIN28B overexpression at the time when endogenous *Lin28b* is being downregulated, led to prolonged nephrogenesis, increased nephron numbers and

elevated kidney function. In contrast, constitutive overexpression of LIN28B resulted in the development of Wilms tumors in these mice. Importantly, Wilms tumors only developed when LIN28B expression was driven by the *Wt1* locus, which is first active in the intermediate mesoderm, but not when it was driven by the *Six2* or *Foxd1* loci, which are active in NPCs and stromal progenitors, respectively. Notably, when LIN28B expression was switched off, tumors regressed, indicating that a block in kidney development caused tumorigenesis. Both studies showed that LIN28B regulates the persistence of SIX2-expressing NPCs, which upon transient and constitutive LIN28B overexpression mediates prolonged nephrogenesis or tumor formation, respectively. In addition, transient LIN28B overexpression, via repression of *let-7*, resulted in an upregulation of the *Igf2* locus, which itself is implicated in Wilms tumorigenesis (Yermalovich et al., 2019). Based on these findings, we hypothesized that LIN28 overexpression may phenocopy Wilms tumorigenesis in kidney organoids and serve, at least partially, as a representative alteration for the broader class of miRNA processing genes.

Initially, we overexpressed LIN28A in human kidney organoids using an adaptation of the protocol developed by Taguchi et al. (2014). When we induced LIN28A before the NPC stage, we observed a reduction of epithelial structures, in particular of LTL-positive tubules, and a concomitant expansion of SIX2-positive NPCs, which is consistent with the LIN28 mouse model (Fig. 3C). However, since we obtained heterogeneous phenotypes, we decided to repeat these experiments using both, a different kidney organoid protocol and a different hiPSC line background. To our surprise, we were not able to reproduce the previous findings. While we still observed a reduction of mature nephron elements upon early (Dox d4), but not later (Dox d7, d9) LIN28A overexpression, we did not find any persisting SIX2-expressing cells and observed a decline in Ki-67, which contrasts findings in the mouse model (Fig. 7; 8; 9) (Urbach et al., 2014). When we overexpressed LIN28B in these organoids, we obtained the same phenotype.

To sum up, LIN28 overexpression phenotypes in organoids generated with the Taguchi/Brown protocol are consistent with findings in mice, while phenotypes in organoids generated with the Morizane protocol are not. This points both, to differences between the two organoid protocols and to species-specific differences between mice and humans.

Notably, of the two LIN28 isoforms LIN28B appears to be more relevant, both in patients and in mouse kidney development. Indeed, *Lin28a* and *Lin28b* transcripts showed different abundances and expression dynamics during kidney development, pointing to *Lin28b* being the predominant paralog (Yermalovich et al., 2019). In addition, studies found increased *LIN28B* expression in Wilms tumors, often associated with a *LIN28B* copy number gain, while *LIN28A* is only rarely expressed (Gadd et al., 2017; Urbach et al., 2014; Viswanathan et al., 2009). It is therefore unclear if the phenotype observed upon LIN28A overexpression in Taguchi/Brown organoids reflects a

genuine Wilms tumor phenotype or an unrelated differentiation defect. Analysis of the respective phenotype for LIN28B overexpression in these organoids and comparison with Wilms tumor patient samples may shed light on potential differences or similarities between LIN28A and LIN28B overexpression. Notably, LIN28A and LIN28B overexpression in our Morizane organoids resulted in very similar phenotypes.

Even though both organoid protocols recapitulate embryonic development, they apply different growth factor cocktails at different steps, and the generation of NPCs takes place at a different pace and with different efficiencies. This emphasizes small but potentially crucial distinctions between the two protocols.

The Taguchi/Brown protocol generates nephron progenitors within EBs at an efficiency of around 60%, based on expression of SIX2 (Fig. 3D). In contrast, the Morizane protocol produces NPCs in a monolayer at an efficiency of around 80-90% (not shown). This aligns quite well with reported efficiencies of these protocols (Morizane and Bonventre, 2017a; Morizane et al., 2015; Taguchi et al., 2014). A lower efficiency in NPC specification leads to a higher fraction of non-NPCs within a given cell population, and it is conceivable that such non-kidney cells might provide niche signals that inhibit NPC differentiation and nephrogenesis. Indeed, we found large numbers of SIX2-expressing cells in unstructured areas of d21 Taguchi/Brown organoids, which points to incomplete differentiation. In contrast, SIX2-positive cells were completely absent from d21 Morizane organoids, and scRNA-seq did not reveal any progenitor gene expression in these organoids (Wu et al., 2018). Moreover, Morizane organoids also contained fewer off-target cells than organoids derived using the protocol by Melissa Little's group (Takasato et al., 2015; Wu et al., 2018), which indicates that the conditions applied by the Morizane protocol are more stringent.

The presence (Taguchi/Brown) and absence (Morizane) of SIX2-expressing cells in wildtype organoids is surprising, considering that both protocols use CHIR as the inducer for differentiation and self-organization. In fact, in Morizane organoids, SIX2 gets downregulated by d12 (Fig. 15B), whereas it persists in Taguchi/Brown organoids. In mammalian development, SIX2-expressing progenitors continue to self-renew at branching UB tips until they succumb to a final wave of commitment shortly after birth in mice and around gestation week 36 in humans (Hartman et al., 2007; Hinchliffe et al., 1991; Short et al., 2014). This may suggest that the presence of SIX2-expressing cells defines a window of opportunity for an effect of LIN28 overexpression. This window would be broader during *in vivo* development and in Taguchi/Brown organoids where SIX2-expressing cells persist, and much narrower in Morizane organoids where SIX2 is rapidly downregulated.

Next, both protocols apply different growth factor cocktails and different incubation times to steer hiPSCs towards the NPC stage. This potentially results in developmental trajectories that yield similar, yet not identical differentiation intermediates that are more or less susceptible to LIN28 overexpression. Moreover, we bluntly overexpressed LIN28A and LIN28B without prior knowledge of the actual level of induction in patients or mouse models. Since *in vivo* developmental processes are tightly regulated, oncogenic transformation might likewise require specific levels of LIN28, which we may not mimic accurately.

Notably, overexpression of LIN28A and LIN28B starting at d4 resulted in reduced *SIX2* expression in d9 NPCs (Morizane protocol), compared to no Dox controls (Fig. 10E). We can therefore not exclude that overexpression of LIN28A and LIN28B already impaired the specification of NPCs, instead of preventing their differentiation. This might explain why the corresponding Dox d4 organoids built fewer nephron structures. In addition, LIN28A and LIN28B protein expression in d21 organoids was rather heterogeneous, as revealed by IF staining (Fig. 10A). This indicates that in some cells the promoters of our transgenes might have been silenced during the differentiation process. However, flow cytometry analysis of mCherry revealed a pronounced induction of the shared transcript (Fig. 10B). Still, differences in protein stability, feedback loops or post-transcriptional and -translational regulation may differentially influence the persistence of mCherry and LIN28 proteins.

Importantly, together with the protocol, we also changed our cell line background. Several reports have highlighted variable differentiation capacities of distinct hiPSC or human ESC lines (Koyanagi-Aoi et al., 2013; Osafune et al., 2006). Indeed, we quite robustly obtained structured kidney organoids from the ND5 hiPSC line using the Taguchi/Brown protocol, but not using the Morizane protocol (data not shown). This hints at distinct properties of the ND5 and the WT29 lines, which may also manifest in distinct phenotypes of LIN28 induction.

An additional explanation for deviating phenotypes between the Lin28 mouse model and Morizane organoids might be a requirement for additional genetic events, particularly within a stringent short-term *in vitro* differentiation system. Indeed, we found both LIN28A and LIN28B to be highly expressed in WT1-positive podocytes and LTL-positive proximal tubules of Dox-treated organoids, which indicates that their overexpression alone was not sufficient to prevent kidney differentiation (Fig. 7B; 8A; 10B). Notably, in Wilms tumor patients, mutations in miRNA processing genes frequently coincide with loss-of-imprinting at 11p15 that results in biallelic *IGF2* expression (Walz et al., 2015). This further suggests that mutations in miRNA processing genes might require additional genetic events to induce Wilms tumorigenesis. In addition, both, sporadic deletion of *Drosha* and expression of a dominant-negative DROSHA E1147K variant driven by the *Six2* locus severely affected kidney development in mouse embryos,

but did not induce Wilms tumor formation (Kruber et al., 2019). However, since *Six2*-driven LIN28 overexpression did not induce Wilms tumor formation either, it is still possible that DROSHA E1147K will induce Wilms tumorigenesis in mice upon earlier induction.

Considering the dependency on additional mutations, it is also conceivable that Wilms tumorigenesis has different requirements in mice versus humans. In fact, while WT1 loss in humans is sufficient to induce Wilms tumor formation, or at least precursor lesions, the corresponding mouse model requires additional biallelic expression of *Igf2* (Hu et al., 2011). In addition, it is possible that tumorigenesis depends on interactions with cell types that are present *in vivo* but not in organoids. Therefore, mouse kidney development may be more susceptible to Lin28 overexpression than human *in vitro* kidney organoid differentiation is.

Finally, induction of *LIN28B* expression that is observed in Wilms tumor patients (Gadd et al., 2017) could potentially be consequential to impaired differentiation in Wilms tumor instead of causing it. In fact, incomplete cell reprogramming *in vivo* resulted in the development of Wilms tumor-like tumors that showed upregulation of an ESC-like gene signature, including *Lin28a* and *Lin28b* (Ohnishi et al., 2014). Interestingly, we found strongly induced mRNA expression of *LIN28A* and *LIN28B* in differentiation-impaired *WT1* KO organoids compared to not-edited counterparts (not shown).

Therefore, we conclude that LIN28 overexpression in Morizane organoids is not sufficient to recapitulate a Wilms tumor phenotype, suggesting that this may require less stringent differentiation conditions or additional mutations. Divergent phenotypes between the Taguchi/Brown and Morizane protocols can be explained by differences in their developmental trajectories and differentiation efficiencies. On the other hand, species-specific differences in human and mouse kidney development and the properties of an *in vitro* system versus *in vivo* physiology may lead to different LIN28 overexpression phenotypes in kidney organoids and mouse models.

4.2 Activation of canonical WNT signaling by CHIR may mask effects of SIX2 and SIX2 Q177R overexpression in human kidney organoids

Alongside LIN28A and LIN28B, we overexpressed the nephron progenitor transcription factor SIX2 and its SIX2 Q177R variant in Morizane organoids. Both *SIX1* and *SIX2* Q177R mutations were identified as recurrent genetic events in Wilms tumor patients (Gadd et al., 2017; Walz et al., 2015; Wegert et al., 2015). Structural analyses indicate that position 177 is located in the DNA binding domain of SIX1 and SIX2, and chromatin immunoprecipitation sequencing (ChIP-seq) revealed a more divergent binding motif of SIX1 Q177R compared to wildtype SIX1, suggesting altered DNA binding capacities. Indeed, *SIX1/2* mutant tumors were associated with high expression of *CITED1*, *EYA1* and *NCAM1* that are expressed in kidney progenitors (Wegert et al., 2015).

SIX2 is required for maintaining a self-renewing kidney progenitor population, which is essential to ensure repeated UB branching and to provide sufficient cells for nephron formation. Indeed, *Six2* KO studies in mice have reported a rapid exhaustion of the NPC pool, formation of ectopic renal vesicles and premature arrest of nephron formation. Consequently, *Six2* KO mice have dramatically smaller kidneys and die at birth (Kobayashi et al., 2008; Self et al., 2006). In contrast, ectopic expression of *Six2* in kidney organ cultures inhibited the differentiation of mesenchymal cells into epithelia (Self et al., 2006). Consistent with this, another gain-of-function study found that persistent *Six2* expression prevented differentiation of NPCs into mature nephrons (Chung et al., 2016). This indicates that SIX2 promotes nephron progenitor maintenance and prevents differentiation and epithelialization.

Based on the functions of wildtype SIX2 and the prevalence of SIX2 Q177R in Wilms tumor patients, we expected that overexpression of both wildtype and mutant SIX2 would yield organoids with fewer tubules and glomeruli as well as persistent progenitor cells.

Indeed, similar to LIN28 Dox d4, overexpression of both, wildtype and mutant SIX2 from d7 but not from d9, resulted in organoids with fewer nephron elements. However, these organoids were smaller and Ki-67 was reduced compared to controls, which is not consistent with tumor formation (Fig. 7; 8; 9). Clearly, we could not use SIX2 staining as a marker for maintained NPC identity in these organoids. However, SIX2-expressing cells did not co-express another progenitor marker SIX1, and cells were broadly scattered throughout the organoid, which is in contrast to differentiation-resistant SIX2-positive cells in *WT1* KO organoids that formed patches, reminiscent of growth in colonies. In addition, we found SIX2 staining or mCherry reporter expression within both, LTL-positive proximal tubules and *WT1*-positive podocytes (Fig. 7B; 8A), which indicates that overexpression of neither wildtype nor mutant *SIX2* was sufficient to prevent NPC differentiation into these cell types.

Notably, we induced the expression of SIX2 and SIX2 Q177R ectopically in cells that would normally not express *SIX2*, especially upon induction from d7. It is therefore conceivable that ectopic SIX2 might interfere with the generation of d9 NPCs, leading to higher frequencies of non-NPCs in the cell pool, which are not able to generate tubular cells and podocytes. This would explain why organoids from Dox d7 treated cells had fewer nephron structures, while organoids from Dox d9 treated cells were less affected. Introducing the Q177R mutation into the *SIX2* gene using CRISPR/Cas9 gene editing would ensure expression of mutant SIX2 at physiological levels in the normal SIX2-expressing cell population. Similarly to *LIN28* induction, *SIX1/2* Q177R mutations have also been found to co-occur with other genetic events, including biallelic expression of *IGF2* and mutations in *DROSHA* (Gadd et al., 2017; Walz et al., 2015). Therefore, it is possible that additional mutations are required to induce a Wilms tumor phenotype in kidney organoids.

It is important to acknowledge that the balance between NPC self-renewal and differentiation is tightly regulated by an interplay of SIX2 and canonical WNT signaling, and that we actually manipulated both of these variables simultaneously.

As explained before, WNT9b secreted by cells of the UB is involved both, in maintaining self-renewing NPCs and in inducing them to form pre-tubular aggregates by activating *Wnt4* and *Fgf8*-expression. These in turn initiate MET and the formation of *Pax8*-expressing renal vesicles (Karner et al., 2011; Kobayashi et al., 2008; Park et al., 2012). Conversely, SIX2 has been shown to repress *Wnt4* expression by binding to its cis-regulatory regions, and *Six2* KO mice show ectopic *Wnt4* expression (Kispert et al., 1998; Kobayashi et al., 2008; Park et al., 2012; Self et al., 2006). It has also been proposed that SIX2 interprets a uniform WNT9b signal in a cell type-specific context: WNT9b activates genes required for NPC maintenance in cells in which SIX2 is present, whereas it activates genes required for differentiation, like *Fgf8* or *Wnt4*, in cells in which SIX2 is low or absent (Karner et al., 2011). Another study revealed co-binding of SIX2 and β -catenin to regulatory regions of both, genes that are involved in progenitor self-renewal and genes that induce NPC differentiation. For example, WNT/ β -catenin signaling activates differentiation-promoting genes like *Wnt4* and *Fgf8*, but co-binding of SIX2 maintains them silent in NPCs. At the same time, lower levels of SIX2 would allow β -catenin to activate these genes. Interestingly, β -catenin was shown to bind a distal enhancer of the *Six2* gene and reduce *Six2* transcription. In addition, NPC genes may be co-activated by SIX2 and β -catenin (Park et al., 2012). Another study suggested that the UB secretes basal levels of WNT9b, which supports progenitor self-renewal at the UB tip, whereas so far unknown signals may amplify β -catenin activity away from the tip, which favors differentiation (Ramalingam et al., 2018). Therefore, it appears that both the levels of canonical WNT signaling activity and of SIX2 expression are relevant for the correct balance between progenitor maintenance and induction.

Based on this complex interplay, it is viable to assume that overexpression of SIX2 enhances NPC maintenance at the expense of NPC differentiation by outcompeting WNT effects. In kidney organoids, we would thus expect loss of nephron structures and maintenance of SIX2-expressing NPCs. In addition, the Q177R variant may activate additional progenitor genes and cell proliferation, resulting in tumor formation.

In our organoid system, however, we mimic WNT9b secretion by the UB by exogenously activating canonical WNT signaling via CHIR. It is very likely that this signal by far exceeds endogenous fine-tuned levels of WNT activity, which overrides the NPC promoting effects of SIX2 overexpression, and thus induces differentiation of NPCs. In fact, the aforementioned SIX2 gain- and loss-of-function studies were performed *in vivo* within an endogenous signaling environment (Chung et al., 2016; Kobayashi et al., 2008; Self et al., 2006).

A more straightforward hypothesis is that activation of canonical WNT signaling by CHIR mimics downstream effects of WNT4, which directly induce MET. Studies in mice suggest, however, that MET processes induced by WNT4 are rather elicited via non-canonical WNT/Ca²⁺ signaling and not via canonical WNT/ β -catenin signaling (Burn et al., 2011; Tanigawa et al., 2011).

Notably, Morizane et al. (2015) showed that SIX2-positive NPCs can spontaneously differentiate into PAX8/LHX1 double-positive renal vesicles upon continuous exposure to FGF9 in the absence of WNT signaling, albeit at a lower efficiency. It would therefore be interesting to investigate an endogenously engineered SIX2 Q177R variant in such a scenario.

In conclusion, the possibility that exogenous activation of WNT signaling may mask effects of SIX2 / SIX2 Q177R overexpression in kidney organoids extends to the general applicability of kidney organoids as disease models: It is likely that mutations associated with defective kidney development or Wilms tumor result in deregulation of signaling pathways that are required for *in vivo* kidney development. However, in order to differentiate hiPSCs into kidney cell types, we manipulate such pathways *in vitro*, and may therefore mask the effects of certain mutations. Hence, it is crucial to consider which pathways are activated or inhibited exogenously, when evaluating the phenotypes of genetic alterations in kidney organoids.

4.3 Ectopic activation of WNT/ β -catenin signaling in kidney organoids via CHIR recapitulates its roles during kidney development

Canonical WNT signaling plays multiple roles during embryonic kidney development, including primitive streak specification, maintenance and differentiation of NPCs, and nephron patterning. In the absence of WNT proteins, a destruction complex of AXIN, APC, GSK-3 β and CK1 binds β -catenin and phosphorylates several amino acid residues (Nusse and Clevers, 2017). Mechanistically, it has been shown that AXIN recruits CK1 to phosphorylate S45 of β -catenin. This serves as a priming site for GSK-3 β and initiates a cascade of subsequent phosphorylation events which ultimately mark β -catenin for proteasomal degradation (Amit et al., 2002). When WNT ligands are present and engage their Frizzled receptors, the destruction complex falls apart and cannot phosphorylate β -catenin anymore, which is stabilized and translocates to the nucleus to regulate target genes in concert with co-operating transcription factors (Nusse and Clevers, 2017).

In Wilms tumors and other cancer types, such as colorectal cancer, liver cancer and melanoma, mutations in *CTNNB1* give rise to stabilized variants of β -catenin which mediate ectopic activation of WNT target genes (Gadd et al., 2017; Kim and Jeong, 2019; Treger et al., 2019).

More specifically, *CTNNB1* mutations in Wilms tumor particularly affect the S45 position of β -catenin and abolish the phosphorylation site that is required to initiate β -catenin degradation. Stabilized β -catenin in turn translocates to the nucleus (Koesters et al., 1999, 2003). Notably, such *CTNNB1* mutations rarely occur alone but they are very frequently associated with loss of *WT1* and mutations in *MLLT1* (Gadd et al., 2012, 2017; Treger et al., 2019). In addition, they are mostly found within full tumors but not within nephrogenic rests (Fukuzawa et al., 2007; Grill et al., 2011). This suggests that β -catenin stabilization potentially occurs as a second event in *WT1* or *MLLT1* mutant tumors late during Wilms tumorigenesis and induces the progression of precursor lesions into full tumors (Gadd et al., 2012, 2017; Walz et al., 2015).

We decided to mimic mutations of *CTNNB1* using chemical inhibition of GSK-3 β by CHIR to ectopically stabilize β -catenin. Since we use CHIR in our organoid protocol from d9 to d10 to induce NPC differentiation (Fig. 3A), we maintained exposure to CHIR beyond d10 and found dose-dependent phenotypes: while low concentrations (0.5 μ M) of CHIR abrogated most proximal nephron parts, including podocytes and proximal tubules, higher concentrations (1 μ M and 3 μ M) also reduced EPCAM-positive epithelia and induced maintenance of SIX2-expressing cells. We also found a relative increase in Ki-67-positive cells, accompanied by organoid overgrowth upon 0.5 μ M and 1 μ M CHIR (Fig. 11).

In a mouse model, combined KO of *Wt1* and expression of stabilized β -catenin (*Wt1/Ctnnb1*) driven by the *Six2* and *Cited1* loci resulted in the development of Wilms tumor-like tumors,

supporting the role of β -catenin as a late event. Those tumors mainly consisted of disorganized epithelia and contained only few stromal and blastemal elements. Interestingly, in mice in which *Wt1* deletion failed, stabilized β -catenin alone gave rise to very similar tumors (Huang et al., 2016). This is not consistent with human *CTNNB1* mutant Wilms tumors which are mainly of mixed histology (Gadd et al., 2012, 2017; Walz et al., 2015).

In contrast, expression of stabilized β -catenin in the stromal lineage driven by the *Foxd1* locus lead to maintenance of NPCs in nephrogenic rests, and the corresponding kidneys were transcriptionally similar to human Wilms tumor patient samples, indicating a pivotal role for β -catenin activation in stromal cells and paracrine effects on NPCs during Wilms tumorigenesis (Drake et al., 2020).

Treatment of our organoids with moderate levels of CHIR (0.5 μ M or 1 μ M) beyond the NPC stage lead to organoid overgrowth accompanied by an increase in Ki-67-positive cells. In these organoids, we found both, areas with big epithelial aggregates, and areas with SIX2-expressing cells (Fig. 11B-E). While we have never specifically confirmed the presence of stromal cells in our organoids, it is possible that epithelial outgrowth and maintenance of SIX2 reflect distinct phenotypes evoked by ectopic activation of WNT signaling in NPCs and stromal cells, respectively.

As described above, canonical WNT signaling has been identified as the primary inductive signal emitted from the UB to induce NPCs to form pre-tubular aggregates and to initiate MET at the onset of nephrogenesis (Karner et al., 2011; Park et al., 2012). Consistent with this, transient activation of WNT signaling in isolated mesenchyme or in SIX2-positive NPCs induces their epithelialization (Kuure et al., 2007; Park et al., 2012). Accordingly, many kidney organoid protocols, including ours, use a brief pulse of WNT signaling activation to induce NPC differentiation (Fig. 3A, Morizane et al., 2015; Takasato et al., 2015). In contrast, constitutive pharmacological activation of WNT signaling in isolated NPCs, or expression of a dominant-active form of β -catenin in mice induced the formation of *Fgf8* and *Wnt4*-expressing pre-tubular aggregates, but prevented an actual MET and the expression of epithelial markers like *Cdh1* (Park et al., 2007, 2012). Likewise, induction of stabilized β -catenin from the pre-tubular aggregate stage on using a *Wnt4*-driven Cre recombinase (Cre), lead to developmental arrest (Deacon et al., 2019). This indicates that canonical WNT signaling is required to induce NPC differentiation and MET to initiate nephrogenesis, and that it needs to be downregulated for cells to further differentiate into epithelial structures.

Stabilization of β -catenin in Wilms tumor and our CHIR treatment both reflect constitutive activation of WNT signaling. In our organoids, constitutive treatment with 1 μ M or 3 μ M CHIR strongly reduced or completely abolished EPCAM-positive epithelia, respectively. In contrast, milder treatment with 0.5 μ M CHIR did not change the percentage of EPCAM-positive cells,

pointing to successful MET, but these epithelia appeared disorganized (Fig. 11D/E). This indicates that activation of WNT signaling in kidney organoids exerts dose-dependent effects on MET.

As mentioned, treatment of developing kidney organoids with CHIR differentially affected distinct nephron cell types. While WT1/PODXL-positive glomeruli and LTL-positive proximal tubules were already reduced at 0.5 μ M and abolished at 1 μ M CHIR, EPCAM-positive tubules were only reduced at 1 μ M and abolished at 3 μ M CHIR.

Notably, in addition to roles during progenitor differentiation and MET, studies have shown that WNT/ β -catenin signaling is required for proximal-distal axis patterning during nephrogenesis, both, early in s-shaped bodies and later in mature nephrons (Deacon et al., 2019; Lindström et al., 2015).

Lindström et al. (2015) identified a gradient of canonical WNT signaling activity along the proximal-distal nephron axis: WNT signaling activity was highest in distal tubules, got gradually reduced towards proximal tubules and was completely absent from glomeruli. Pharmacological activation and inhibition of canonical WNT signaling in *ex vivo* kidney cultures via CHIR and IWR1, respectively, shifted nephron segment identities along the proximal-distal axis. Indeed, treatment with CHIR resulted in a reduction of proximal nephron structures (Lindström et al., 2015). This is consistent with our findings in kidney organoids that glomeruli and proximal tubules are affected by smaller CHIR concentrations than more distal tubules that express EPCAM. We therefore propose that ectopic activation of canonical WNT signaling by CHIR imposes an all-distal identity onto developing nephrons in our kidney organoids. Similar to our experiments, Morizane et al. (2015) showed that treatment of developing kidney organoids with the Notch inhibitor DAPT impaired the formation of proximal tubules, which is consistent with a role for Notch signaling in specifying the proximal-distal axis (Cheng et al., 2007; Lindström et al., 2015). Interestingly, Lindström et al. (2015) also revealed dose-dependent effects of CHIR treatment on their kidney explants, with low and moderate levels modulating nephron axis patterning and high doses abrogating nephron formation. While in our case, all nephron structures were lost upon 3 μ M CHIR, in this study 6 μ M CHIR were required to disrupt epithelialization.

Importantly, in our experiments, loss of nephron structures was accompanied by maintenance of occasional SIX2-positive cells in CHIR treated d21 organoids. However, the aforementioned studies either reported downregulation of SIX2 upon ectopic WNT signaling activation (Park et al., 2007, 2012) or did not provide any data on SIX2 (Lindström et al., 2015). Of note, we found persistent SIX2-expressing cells in unstructured portions of kidney organoids generated with the Taguchi/Brown protocol (Fig. 3C). Interestingly, the medium used for organoid culture at the liquid-air interface contains 3 μ M CHIR, which is not removed. While continuous exposure to WNT signaling might impair epithelialization as described above, diffusion of CHIR from the

medium into the developing organoids may also create gradients of WNT signaling activity. Low local levels of WNT activity may therefore be insufficient to induce NPC differentiation and instead help maintain SIX2-positive NPCs (see above). We similarly speculate that, even though CHIR is uniformly distributed in the organoid culture medium in our 96-well plate setting, diffusion of CHIR might create gradients of WNT signaling activity within the 3D developing organoids that evoke distinct responses in different areas. Consequently, we obtained heterogeneous organoids with structured EPCAM-positive parts opposed to unstructured areas with SIX2-expressing cells (Fig. 11).

Besides mutations in *CTNNB1*, truncating mutations of *WTX* (*AMER1*) similarly lead to stabilization of β -catenin. *WTX* acts as part of the β -catenin destruction complex, and protein truncations result in loss of its β -catenin binding sites. Interestingly, *WTX* mutations do not correlate with *WT1* loss, which indicates that stabilization of β -catenin directly by removing S45 or indirectly by inhibiting the destruction complex, may have distinct functional outcomes (Gadd et al., 2017; Hohenstein et al., 2015; Huff, 2011). By targeting GSK-3 β , CHIR treatment indirectly inhibits β -catenin destruction, and may also interfere with additional roles of GSK-3 β beyond phosphorylating β -catenin (Beurel et al., 2015). In addition, the levels of WNT pathway activation imposed by CHIR, even though provided at different concentrations, may deviate from endogenous signaling, resulting in non-physiological responses. This may explain the total loss of epithelial structures and maintenance of SIX2-expressing cells upon prolonged exposure to 3 μ M CHIR.

Our results therefore indicate that constitutive activation of WNT signaling in developing kidney organoids via CHIR interferes dose-dependently with both, the induction of MET and patterning of the proximal-distal nephron axis. This is consistent with studies in mice and *ex vivo* cultures, and corroborates the applicability of kidney organoids to study the roles of signaling pathways in NPC induction, MET and nephron patterning (Karner et al., 2011; Lindström et al., 2015; Park et al., 2007, 2012). While organoid overgrowth upon CHIR treatment supports tumorigenesis, additional experiments and comparison with human Wilms tumors are required to distinguish between MET or patterning defects and Wilms tumorigenesis definitively. Genetic deletion of the S45 phosphorylation site of β -catenin could be a viable alternative for Wilms tumor modeling, but will most likely interfere with normal kidney organoid development. Instead, fine-tuned inducible expression of such a mutant in kidney organoids, both with and without additional genetic alterations, could shed light on the role of β -catenin stabilization in Wilms tumorigenesis.

4.4 *WT1* KO organoids recapitulate roles of WT1 during kidney development

Loss of *WT1* is one of the most prevalent alterations in Wilms tumor. The *WT1* gene on chromosome 11p13 encodes a zinc-finger transcription factor, and due to combinations of alternative exons, alternative start codons, alternative splice sites and RNA editing, the locus can in theory generate 36 different proteins. Next to interacting with DNA, WT1 also binds RNA and is involved in posttranscriptional regulation (reviewed in Hastie, 2017; Miller-Hodges and Hohenstein, 2012). Although *WT1* expression after birth is restricted to only few cell types, including the podocytes of the kidney (Hastie, 2017), it plays a pivotal role during many developmental processes. Indeed *Wt1* KO mice are embryonic lethal and display severe defects in several tissues, including a complete lack of kidneys and gonads (Kreidberg et al., 1993; reviewed in Miller-Hodges and Hohenstein, 2012). In humans, germline mutations of *WT1* have been associated with Wilms tumor predisposition syndromes including WAGR, DDS and Frasier syndrome. (Hastie, 2017; Treger et al., 2019).

In the developing kidney, *WT1* is first expressed in the intermediate mesoderm. Afterwards, its expression is elevated in the MM, cap mesenchyme and pre-tubular aggregates, before it gets restricted to the proximal portion of renal vesicles, comma- and s-shaped bodies, and finally to glomerular podocytes. Thus, loss of WT1 at different developmental stages results in distinct phenotypes from Wilms tumor to glomerulosclerosis (reviewed in Dong et al., 2015a; Hastie, 2017).

We set out to develop a model for Wilms tumor in hiPSC-derived kidney organoids by deleting *WT1* in iPSCs as well as at later stages during kidney organoid differentiation.

In contrast to the *Wt1* KO mouse which did not have any kidneys (Kreidberg et al., 1993), we succeeded in generating *WT1* KO organoids from *WT1* KO iPSCs. Importantly, while *Wt1* KO mice were still able to generate MM, their UB did not grow out, and finally the MM underwent apoptosis. Co-culture of isolated MM with embryonic spinal cord, as an inducer of nephron formation, revealed that *Wt1* KO MM was unable to respond to inductive signals, indicating a cell-autonomous role of WT1 in the MM (Kreidberg et al., 1993). Indeed, our *WT1* KO organoids displayed elevated apoptosis during organoid culture compared to not-edited controls. However, we formally only measured this between d14 and d18 and not around the NPC stage (Fig. 13E). Notably, both, deletion of Fgf receptor (*Fgfr*) 1 and *Fgfr*2 within the MM, and combined deletion of *Fgf20* and *Fgf9* resulted in failed kidney development, very similar to the *Wt1* KO (Barak et al., 2012; Poladia et al., 2006). In fact, WT1 directly binds to and regulates the transcription of several *Fgf* genes, and treatment of E11.5 kidney cultures lacking *Wt1* with recombinant FGF20 largely rescued apoptosis within the MM (Motamedi et al., 2014). We therefore surmise that FGF9, which is supplemented in our culture medium from d7 to d14, suppresses a potential induction of

apoptosis upon loss of *WT1*, which allows us to derive *WT1* KO organoids. Apoptosis between d14 and d18 might reflect a further dependence of cell survival on *WT1* at later stages of organoid development.

We found a reduction of *PODXL* and *NPHS1*-expressing podocytes and of *EPCAM*^{high}-expressing tubules in *WT1* KO organoids, irrespective of the KO time point (Fig. 13C; 14A). Notably, *WT1*-positive cells were much more reduced than *EPCAM*^{high} cells. This either reflects different proliferation rates of tubular cells and podocytes that are derived from residual unedited cells in the organoids, or that *WT1* KO NPCs contributed to *EPCAM*^{high} tubules. In fact, *WT1* mutations were present both, in stromal cells and in *EPCAM*-positive epithelia of 3D organoids derived from Wilms tumor patients (Calandrini et al., 2020). Thus, potentially, a fraction of *EPCAM*^{high} tubules in *WT1* KO organoids is derived from KO cells and not from cells that escaped Cas9-induced double-strand breaks.

In contrast, we found *SIX2*-positive cells in *KO*^{iPSC}, *KO*^{d4-7}, *KO*^{d9-11}, but not in *KO*^{d11-14} organoids. Since *SIX2* gets downregulated by d12 in not-edited organoids (Fig. 15A/B), it is likely that Cas9 induction between d11 and d14 results in a depletion of *WT1* only after *SIX2* had been downregulated. At the same time this suggests that later KO of *WT1* does not reactivate *SIX2* expression. Thus, absence of *WT1* impairs the developmental progression of *SIX2*-positive NPCs, whereas the reduction of epithelia and podocytes in *KO*^{d11-14} organoids potentially reflects additional defects of kidney development upon *WT1* loss that are independent of *SIX2* downregulation (see below).

When we more closely evaluated *SIX2*-positive cells in d21 KO organoids, we found co-expression of *SIX2* with intermediate levels of *EPCAM*. Flow cytometry analysis revealed that this *SIX2*-*EPCAM*^{mid} population was enriched in *KO*^{iPSC} and *KO*^{d4-7}, to a lesser extent in *KO*^{d9-11}, but not in *KO*^{d11-14} organoids (Fig. 14D). *EPCAM* levels increased between d7 and d10 in all conditions, which suggests the activation of an epithelial program in NPCs similar to induction during kidney development. In the absence of *WT1*, this program is arrested at a *SIX2*-*EPCAM*^{mid} stage. Isolation of *NCAM1*⁺*CD133*⁻ *SIX2*-expressing cells from human fetal kidney similarly revealed an *EPCAM*^{dim} subpopulation and single-cell qPCR defined these cells as being in the process of MET (Podeshakked et al., 2017).

Notably, during kidney development, timed ablation of *Wt1* in kidney organ cultures and in mice demonstrated an essential role of *WT1* in the completion of MET at the onset of nephron development (Berry et al., 2015; Davies et al., 2004; Hu et al., 2011). As explained above, one of the pivotal genes in this process is *Wnt4*, which is activated due to signals from the UB. In fact, *WT1* has been implicated in directly regulating *Wnt4* expression (Essafi et al., 2011; Sim et al., 2002). Thus, it is conceivable that loss of *WT1* in our organoid system, like *in vivo* and *ex vivo*,

impedes the completion of MET programs, resulting in an aberrant SIX2-EPCAM^{mid} population. Notably, this population expanded between d12 and d21 (Fig. 15E), and thus appears to contain arrested, proliferative SIX2-positive NPCs. Interestingly, we did not identify such a population in CHIR treated organoids, where SIX2 and EPCAM seemed to occur mutually exclusive.

4.5 *WT1* KO organoids transcriptionally resemble human Wilms tumors

RNA-seq of KO^{iPSC} and KO^{d4-7} samples confirmed a developmental delay of *WT1* KO organoids, which was associated with the induction of progenitor- and muscle-specific genes, the concomitant downregulation of differentiation-related genes and the induction of cell cycle-associated transcription (Fig. 17-19). Importantly, transcriptional changes found in *WT1* KO organoids correlated with gene expression signatures of Wilms tumor patients and only to a smaller extent with those of other kidney tumors (Fig. 20).

Loss of *WT1* is considered an early, rate-limiting event during Wilms tumor formation, as *WT1* mutations are frequently found within intralobar nephrogenic rests, which are considered precursor lesions of Wilms tumor (Park et al., 1993). The predominant histology of *WT1* mutant Wilms tumors is stromal, with few epithelial and blastemal elements (Schumacher et al., 1997). Wilms tumors with loss of *WT1* are often associated with an activation of muscle gene expression, including *MYOD*, *MYH3* and *MYOG*, whereas this association is much weaker in Wilms tumors with intact *WT1* (Miyagawa et al., 1998). Consistent with this, Gadd et al., identified a subtype of Wilms tumor that is characterized by low expression of *WT1*, often due to *WT1* mutations, and upregulation of muscle-specific genes (Gadd et al., 2012). These tumors frequently contain nephrogenic rests and display a mixed histology. Comparison of this subset with public data sets revealed the expression of genes specific to the pre-induction intermediate mesoderm, which indicates a developmental arrest before induction of NPC differentiation and explains the presence of mesenchymal elements within nephrogenic rests. Notably, this subtype also showed frequent mutations of *CTNNB1*, which is common in *WT1* mutant Wilms tumors and is thought to be acquired as a secondary event within nephrogenic rests, driving tumor progression (Gadd et al., 2012). In a more recent study, the authors further confirmed the association of *WT1* mutations and intralobar nephrogenic rests, and in many *WT1* mutant tumors muscle transcription was upregulated (Gadd et al., 2017).

Skeletal muscle and kidney are specified from neighboring mesoderm subpopulations, the paraxial and the intermediate mesoderm, respectively. Notably, gene expression profiling of long-term cultures derived from *WT1* mutant Wilms tumors revealed congruence with genes

expressed in paraxial mesoderm (Royer-Pokora et al., 2010). In addition, an early study proposed a direct role of WT1 in preventing myogenesis both *in vitro* and *in vivo* (Miyagawa et al., 1998) Muscle and neuronal cell types are known off-target populations associated with kidney organoid differentiation (Wu et al., 2018). Of note, we found an induction of both, muscle and neuronal genes in *WT1* KO organoids. However, based on our own analysis with Wilms tumor patient data as well as the aforementioned studies, we are confident that induction of muscle gene expression upon *WT1* loss in kidney organoids recapitulates patient-specific alterations, rather than the expansion of an off-target population.

The correlation of our RNA-seq data with those of Wilms tumor patients was moderate (R=0.45, Fig. 20A) and thus not ideal. A very simple explanation is that our protocol only generates the MM, but lacks the UB and all of its progeny, like collecting ducts. In addition, our protocol does not induce differentiation of stromal cells or the formation of blood vessels, although occasional endothelial cell populations have been described (Little and Combes, 2019). In addition, our organoids lack innervation and immune cells, which interact with the tumor. The absence of those cell types in our organoids naturally affects the correlation between organoid and patient data. In addition, the notion that *WT1* mutations frequently co-occur with other alterations like β -catenin stabilization raises the possibility that our organoids indeed represent precursor lesions, similar to nephrogenic rests, rather than full tumors. Additional experiments using a combination of *WT1* loss and, for example, expression of a stabilized variant of β -catenin might be viable to assess whether the corresponding organoids show different phenotypes and if they correlate even better with patients. Nevertheless, the overlap of our organoids with patient data, particularly with respect to subtype specific expression of muscle-related genes, is striking and provides proof-of-concept for modeling Wilms tumor in kidney organoids.

4.6 Kidney organoids and mouse models allow to study Wilms tumor initiation

Existing model systems for Wilms tumor include cell lines, PDX, 3D cultures of primary tumor tissue and mouse models (Introduction 1.2.3). While the majority of these systems originate from primary tumors, mouse models and hiPSC-derived organoids offer a setting to study Wilms tumor initiation.

Indeed, in addition to the traditional *Wt1* KO mouse (Kreidberg et al., 1993), several other *Wt1* mouse models have been generated, which develop Wilms tumors upon loss of *Wt1*.

The first model combines biallelic expression of *Igf2* with a sporadic KO of *Wt1*, induced by a ubiquitously expressed Tamoxifen-inducible Cre (*Wt1/Igf2*) (Hu et al., 2011). Even though both, WT1 depletion and *Igf2* upregulation alone were insufficient to induce tumors, combined WT1

loss and *Igf2* upregulation resulted in Wilms tumor formation. While human *WT1* mutant Wilms tumors are mostly associated with stromal histology, tumors of *Wt1/Igf2* mice were triphasic with a predominance of blastemal cells. In addition, they showed elevated expression of *Six1*, *Pax2* and *Eya1*, but not of *Six2*. At the same time, expression of *Wnt4* was decreased, which is in agreement with previous studies showing the direct regulation of *Wnt4* by WT1 to induce MET (Davies et al., 2004). Of note, in our *WT1* KO organoids *SIX2*, *SIX1* and *EYA1* were upregulated (cluster 1), whereas *WNT4* expression was delayed (cluster 17) (not shown).

As an extension to the study above, Huang et al. (2016) generated *Wt1/Igf2* mice with cell type-specific deletion of *Wt1*, using the *Six2* and *Cited1* loci to drive Cre expression. Interestingly, only deletion of *Wt1* in descendants of *Cited1*-positive cells resulted in tumor development. Similar to the ubiquitously expressed Cre, these mice developed triphasic tumors, albeit with slightly reduced fractions of stromal and blastemal elements. While these tumors displayed high expression of *Eya1* and *Pax2*, the authors also detected high levels of *Wnt4* both using ubiquitous and *Cited1*-driven *Wt1* ablation, which contrasts their previous findings.

In addition, this study introduced a second mouse model, combining a *Six2*- or *Cited1*-driven KO of *Wt1* with expression of stabilized β -catenin (*Wt1/Ctnnb1*). These mice generated tumors that were mostly epithelial, which is in contrast to the predominant stromal histology found in human *WT1* mutant Wilms tumors, both with and without additional *CTNNB1* mutations (Gadd et al., 2012; Schumacher et al., 1997). Moreover, *Wt1/Ctnnb1* tumors lacked expression of genes specific to intermediate mesoderm or MM, like *Eya1*, *Osr1*, *Pax2* and *Hoxa11*. Interestingly, expression of stabilized β -catenin alone, without loss of *Wt1*, resulted in tumors that were indistinguishable from *Wt1/Ctnnb1* tumors. Finally, deletion of *Wt1* in *Foxd1*-expressing stromal progenitors did not induce tumorigenesis, suggesting that *Wt1* mutant tumors do not originate from committed stromal progenitors, despite the presence, or even predominance (in human tumors) of stromal histology (Huang et al., 2016).

Notably, the *Six2*-Cre lines used to drive Wilms tumor mutations in NPCs were effectively heterozygous for *Six2* due to knock-in of a Cre cassette into the *Six2* locus. It is therefore possible that haploinsufficiency for *Six2* may prevent tumorigenesis in the context of certain mutations, such as deletion of *Wt1*. The same may be relevant for the *Lin28* mouse model (see above), in which *LIN28* overexpression did not induce tumor formation when driven by the *Six2* locus (Urbach et al., 2014). Notably, the *Six2*-Cre mouse line used by Huang et al. (2016), displayed an unexpected increase in nephron numbers upon *Six2* haploinsufficiency due to increased proliferation, as well as deregulation of a subset of NPC markers (Combes et al., 2018). It is therefore still unclear, in what way *Six2* haploinsufficiency may influence tumorigenesis in the context of Wilms tumor mutations.

A different study set out to delineate the roles of WT1 during different phases of kidney development by deleting *Wt1* using stage-specific Cre drivers (Berry et al., 2015). Deletion of *Wt1* driven by the *Nestin* (*Nes*) locus (*Nes-Cre*) occurs in the MM before NPCs are induced to differentiate and undergo MET. This time point therefore resembles our early KO^{iPSC} and KO^{d4-7} samples. Indeed, *Nes*-driven KO of *Wt1* resulted in kidneys that displayed an expansion of the MM and a loss of epithelial structures likely due to a failure to upregulate epithelial genes like *Pax8* and *Cdh1*. In addition, the SIX2-positive cap mesenchyme appeared disorganized and expanded beyond its normal compartment close to the UB. Importantly, gene expression signatures of these kidneys were similar to those of human *WT1* mutant Wilms tumors, and overlapping genes were enriched for GO terms associated with muscle structure and function. This is consistent with our findings that early loss of *WT1* as in the KO^{iPSC} and KO^{d4-7} conditions yields a Wilms tumor phenotype with induction of muscle gene expression. Notably, these kidney phenotypes were analyzed in embryos, and mice died right after birth. However, in one surviving animal, the authors found a Wilms tumor, which indicates that loss of *Wt1* driven by the *Nes* locus can result in Wilms tumor formation (Berry et al., 2015).

Taken together, KO of *Wt1* in mice yields phenotypically different Wilms tumors, which are or are not dependent on additional genetic events. While the *Wt1/Igf2* mouse strictly requires an upregulation of *Igf2* to induce Wilms tumor formation, the *Nes-Cre Wt1* KO mouse can develop tumors without additional events. In addition, *Wt1/Ctnnb1* tumors are predominantly epithelial, while human tumors with the same genetic alterations are more frequently of the stromal or mixed type. Moreover, in these mice two Wilms tumor events are introduced simultaneously, whereas this likely occurs sequentially in human tumors (Gadd et al., 2012).

Deletion of *Wt1* within committed *Six2*- or *Cited1*-expressing progenitor cell populations provides proof-of-principle that these cell types can drive tumorigenesis and that the phenotype of the corresponding tumor depends on the genotype rather than the cell population of origin.

However, it is questionable to what extent such mouse models per se recapitulate the human disease, in addition to well-known species-specific differences between mice and humans. Comparison of gene expression signatures of such tumors with patient data would inform if these mouse models are suitable for further analyses of Wilms tumorigenesis.

4.7 Later loss of WT1 is consistent with defects in podocyte development

In the study described above (Berry et al., 2015), *Wt1* deletion was not only induced in the MM (*Nes-Cre*) but also around the MET stage using a *Wnt4-Cre*, and just after MET using a *Pax8-Cre*. To some extent, these two developmental stages reflect our KO^{d9-11} and KO^{d11-14} organoids, respectively.

Wt1 deletion driven by *Wnt4-Cre* generated a mixed phenotype that showed signs of MM condensation, MET and occasional formation of early tubules. However, mature tubules and glomeruli were lacking, and the MM expanded (Berry et al., 2015). In our KO^{d9-11} organoids, we similarly found fewer tubules and glomeruli, and a persistence of SIX2-expressing cells.

In contrast, KO of *Wt1* driven by *Pax8-Cre* resulted in normal MM condensation and MET, but mature tubules and glomeruli did not develop. In addition, the immature nephrons showed patterning defects. Notably, in these kidneys, *Six2*-expressing cells were strictly confined to cap mesenchyme, which is consistent with a block in development after MET. Gene expression analysis revealed that upregulated genes were enriched for GO terms related to kidney development, and gene signatures resembled *WT1* wildtype Wilms tumors, which are thought to arise at later stages than *WT1* mutant tumors (Berry et al., 2015). The phenotype of *Pax8-Cre Wt1* KO kidneys thus resembles our KO^{d11-14} organoids, which harbored fewer tubules and glomeruli but did not maintain SIX2 expression.

Loss of glomerular structures upon *Wt1* KO after MET (*Pax8-Cre*) or in KO^{d11-14} organoids therefore points to additional roles of WT1 beyond exiting the SIX2-positive NPC stage. Notably, in addition to a predisposition to Wilms tumor, DDS and Frasier syndrome with mutant *WT1* are associated with impaired podocyte development or maintenance, leading to glomerulopathy. Likewise, a mouse model in which *Wt1* was deleted specifically in developing podocytes showed defects in podocyte maturation, which lead to kidney failure and death shortly after birth (Dong et al., 2015b). In fact, WT1 ChIP-Seq experiments have revealed WT1 binding to gene regulatory regions of around 50% of all described podocyte-specific genes, underscoring the pivotal role of WT1 in podocyte development and maintenance. Indeed, WT1 was shown to bind to 18 out of 31 genes currently known to be mutated in podocyte disease, including *Nphs1* and *Nphs2* (Dong et al., 2015b; Kann et al., 2015, reviewed in Hastie, 2017). We noted that the vast majority of WT1-positive cells in our *WT1* KO organoids co-expressed PODXL, which is a described transcriptional target of WT1, indicating that the few podocytes detectable in these organoids were derived from residual unedited cells in the organoids (Fig. 14A).

Potentially, KO^{d9-11} and KO^{d11-14} organoids can be used to further study the roles of WT1 during NPC differentiation and MET, and podocyte differentiation, respectively.

4.8 *WT1* KO organoids extend the scope of existent kidney disease models

To our knowledge, we established the first hiPSC-derived kidney organoid model for Wilms tumor. However, we need to note a recent study that investigated the role of mutations in the YEATS domain of *MLLT1*, a reader of histone acetylation that is mutated in Wilms tumor (Gadd et al., 2017; Perlman et al., 2015; Wan et al., 2020). The authors expressed a mutant *MLLT1* version in developing mouse kidney organoids generated with the protocol by Taguchi et al. (2014), and found blastema-like aggregates that were reminiscent of Wilms tumor. However, this study did not generate a human model and did not provide any additional characterization to determine how well these organoids resembled actual Wilms tumor (Wan et al., 2020)

In the past, several studies set out to develop organoid models for different kidney diseases. These include models for polycystic kidney disease (PKD), glomerulopathy, congenital nephrotic syndrome, nephronophthisis, as well as acute kidney injury, elicited by drug nephrotoxicity.

Morizane et al. (2015) treated d21 kidney organoids with the antibiotic gentamicin or with the anticancer drug cisplatin (Morizane et al., 2015), and found upregulation of kidney injury molecule (*KIM*)-1 and of the DNA damage marker γ H2AX. Notably, injury mediated by gentamicin was restricted to proximal tubules, while cisplatin affected both proximal and distal tubules, which is consistent with their reported mode of actions (reviewed in Glezerman and Jaimes, 2016; Randjelovic et al., 2017). Other groups obtained similar results using different organoid systems, supporting the applicability of kidney organoids for assessing drug nephrotoxicity (Freedman et al., 2015; Takasato et al., 2015).

PKD is caused by mutations in either *PKD1* or *PKD2*, and is characterized by the formation of liquid-filled cysts that strongly impair kidney function. Using *PKD1* or *PKD2* KO iPSCs, Freedman et al. (2015) generated kidney organoids that formed large fluid-filled cysts that originated from hyper-proliferative kidney tubular epithelial cells and resembled prenatal cysts of PKD patients (Cruz et al., 2017; Freedman et al., 2015). Of note, the authors failed to robustly model PKD using patient-derived iPSCs due to high variability of corresponding organoids, which emphasizes the benefits of engineered iPSC lines to investigate an otherwise heterogeneous disease. *PKD1/2* KO organoids provide proof-of-concept for modeling genetically defined diseases in kidney organoids and offer a platform for genetic or compound screens that may reveal pathways involved in cystogenesis or identify compounds that reduce cyst formation.

Formation of cysts is also a phenotype of nephronophthisis, a ciliopathy that mainly affects children. Kidney organoids generated from patient-derived iPSCs recapitulated the cilia defect, and gene correction confirmed the causal role of an inherited gene mutation (Forbes et al., 2018).

Diseases of the glomerulus are another set of disorders that were addressed using kidney organoid models. One of the genes implicated in glomerular disease is *PODXL*, which is strongly

expressed in podocytes but not in tubular cells. *PODXL*-deficient kidney organoids revealed that *PODXL* is not required for proper differentiation of podocytes but for the establishment of junctions between adjacent podocytes, emphasizing its role in podocyte function (Freedman et al., 2015). This model may therefore provide additional insights into *PODXL*-associated glomerular disease mechanisms.

Congenital nephrotic syndrome is a glomerular disorder that is frequently caused by mutations in *NPHS1* or *NPHS2*. Both encode podocyte proteins that are required to form the slit diaphragm, which is an essential component of the glomerular filtration barrier and ensures the retention of serum proteins in the blood during glomerular filtration. Patient-specific kidney organoids that harbor a missense mutation in the *NPHS1* gene showed mislocalization of the *NPHS1* protein in podocytes, and transplantation of these organoids into mice revealed that mutant podocytes were unable to form slit diaphragms, validating a patient phenotype in organoids (Tanigawa et al., 2018). A different study investigated a novel *NPHS1* variant by isolating glomeruli from kidney organoids generated from patient-derived iPSCs, and uncovered a novel mechanism of action (Hale et al., 2018).

Together, these models emphasize the general applicability of kidney organoids to study a variety of different kidney diseases from injury over PKD to glomerular diseases, both using patient-derived iPSCs and gene editing of conventional iPSC lines. In addition, as *in vitro* systems, kidney organoids offer a platform to pinpoint disease-causing mutations via gene corrections and rescue experiments, and to perform genetic and compound-based screens. These systems therefore validate our intention to provide a kidney organoid model for Wilms tumor and inspire potential future applications for our system in uncovering tumorigenic pathways.

4.9 *WT1* KO organoids contribute a novel developmental tumor model

On top of our phenotypic characterization based on flow cytometry, IF stainings and gene expression analyses, we performed serial passaging and transplantation experiments in order to test for classical tumor cell properties including immortality and sustained proliferation. Serial passaging of cells derived from *WT1* KO organoids with wildtype NPCs revealed an expansion of cells and maintenance of *SIX2* expression for a period of 60 days, but only in the presence of wildtype cells (Fig. 22). In addition, we transplanted single-cell suspensions generated from *WT1* KO organoids into wildtype organoids. Over a course of two weeks, cells expanded within the wildtype organoids and maintained *SIX2* expression, even in the absence of growth factors (Fig. 23; 24). These experiments underscore that *WT1* KO organoids not only phenotypically resemble Wilms tumor but show functional characteristics of tumor cells. This emphasizes the authenticity of *WT1* KO organoids as the first hiPSC-derived Wilms tumor model.

To our knowledge, there are no other hiPSC-derived organoid models for kidney tumors available to date, but several groups have generated hiPSC-derived models for tumors of the central nervous system (CNS) both using similar and different approaches compared to our model.

Atypical teratoid/rhabdoid tumor (AT/RT) is a fatal brain tumor that, like Wilms tumor, arises in early childhood, most frequently due to loss of *SMARCB1*. Studies in mice have shown that deletion of *Smrcb1* needs to occur in a restricted time window during embryonic development to allow tumor formation. This is reminiscent of findings in Wilms tumor that loss of *WT1* needs to occur in the pre-induction mesenchyme to induce tumorigenesis, and matches our findings that early *WT1* depletion results in KO organoids whose gene signatures resemble those of human Wilms tumors.

Combined KO of *SMARCB1* and *TP53* in iPSCs yielded neural progenitors that, upon transplantation into mouse brains, gave rise to tumors (Terada et al., 2019). However, these tumors did not recapitulate the typical rhabdoid histology of AT/RT, which was only detected when mutant iPSCs were directly transplanted without prior differentiation into neural progenitors. Interestingly, the authors identified an ESC-like gene expression signature both, in iPSC-derived tumors and patient samples. Similarly Ohnishi et al. (2014) reported the activation of embryonic gene expression programs in Wilms tumor-like cancers which arose upon incomplete *in vivo* reprogramming in mice, but this signature has not been re-confirmed in other Wilms tumor model systems since. Wilms tumor most likely develops through a developmental arrest and expansion of the arrested cell population, whereas AT/RTs seem to acquire the embryonic signature over time. Notably, this study did not generate brain organoids from mutant iPSCs, and tumors developed only *in vivo* after injection of cells into mouse brains. It would thus be interesting whether *SMARCB1/TP53* mutant organoids reflected rhabdoid tumors, as a full *in*

in vitro model. Vice versa, we have never tested transplantation of *WT1* mutant d9 NPCs or d21 organoids into mice. Our results that *SIX2*-expressing cells can be maintained within mature kidney organoids suggests that they would also expand upon *in vivo* transplantation. However, this was out of scope for this project.

Another study developed 3D organoid models for primitive neuroectodermal tumors of the CNS and glioblastoma multiforme (Bian et al., 2018). The authors used both, oncogene overexpression via transposon-mediated gene insertion, and CRISPR/Cas9-mediated mutation of tumor suppressor genes, in order to generate single mutations and several combinations of alterations that were reported in distinct human brain tumors. Notably, the plasmids for the corresponding alterations were electroporated into early brain organoids, after their neural induction. Co-transfection of a GFP vector allowed the authors to identify developing tumors as an expansion of GFP-positive foci. After one month, tumors developed from transfected cells within a subset of the organoids, which resembled both primitive neuroectodermal tumors and glioblastomas depending on the respective mutation. Ectopic transplantation of tumor organoids under the kidney capsule of mice revealed invasiveness of the glioblastoma models, which is consistent with the disease in glioblastoma patients (Bian et al., 2018).

Notably, the strategy of introducing mutations into developing organoids differs from ours. We used a cell line carrying a *WT1* gRNA and an inducible Cas9, which, depending on the efficiency of double strand breaks, induces a *WT1* KO in the majority of cells. In contrast, plasmid delivery into 3D aggregates via electroporation introduces mutations in only a fraction of cells, which offers the opportunity to study tumorigenesis within a wildtype tissue context.

Importantly, serial passaging of cells derived from *WT1* KO organoids revealed that wildtype cells are required for the long-term maintenance and expansion of *SIX2*-expressing progenitor cells, which underscores the importance of niche factors provided by wildtype cells (Fig. 22). Similar to introducing mutations into few cells within aggregates, our experiments of mixing *WT1* KO d9 NPCs with wildtype d9 NPCs at the onset of organoid culture offers a system to study clonal growth of *WT1* KO cells (Fig. 21A). In fact, similar to an expansion of GFP-positive foci (Bian et al., 2018), we observed an overgrowth of KO^{d4-7} cells in these chimeric organoids (Fig. 21C-E). However, to reveal real clonal expansions over a longer culture period, we would need to decrease the input fractions of KO cells further. Finally, instead of transplanting Wilms tumor organoids into mice, we transplanted single-cell suspensions derived from these organoids within the *in vitro* system into wildtype organoids. Using this approach, we demonstrated the ability of *WT1* KO cells to expand and maintain *SIX2* expression within an *in vitro* “physiological” setting (Fig. 23; 24).

A similar strategy of *in vitro* transplantation has been employed with another brain organoid model for glioblastoma multiforme. In this case, the authors introduced a point mutated *HRAS* transgene into the *TP53* locus within developing brain organoids, generating a subset of cells with both activated *HRAS* and KO of *TP53* (Ogawa et al., 2018). After organoid tumors developed, they co-cultured tumorous fragments with wildtype organoids and found that these fragments first expanded on the surface of the wildtype organoids before they invaded them, recapitulating the invasiveness of glioblastomas. In addition, patient-derived tumor cell lines showed a comparable invasive behavior upon injection into mouse brains and upon co-culture with wildtype organoids. Since we transplanted single-cell suspensions directly into wildtype organoids by breaking them apart, we were not able to study invasive growth in our system. However, combining aggregated cells from *WT1* KO organoids with wildtype organoids would allow us to perform similar invasion studies in our kidney organoid system. Microinjection of cell suspensions into wildtype organoids would also be a viable method for transplantation, which would also avoid a potential regenerative response in the wildtype host organoids due to mechanical injury.

Successful transplantation of tumor organoid-derived single-cell suspensions (Fig. 23; 24) and fragments (Ogawa et al., 2018) into/onto wildtype organoids supports the applicability of organoids as surrogates for transplantation experiments, both for tumor cell propagation, similar to PDX, and for studying functional tumor properties. Sequencing of original *WT1* KO organoids and propagated cells would inform to what extent *WT1* KO cell identity can be maintained over time under the given conditions.

Besides many similarities, the aforementioned studies also highlight approaches that could improve our organoid system to study Wilms tumorigenesis. For example, the strategy of producing a batch of wildtype organoids and electroporating them with different constructs for oncogene overexpression or CRISPR/Cas9-mediated KO confers much more flexibility and allows testing many combinations of mutations simultaneously. Compared to that, generating separate iPSC lines for each alteration via lentiviral transduction of gRNAs or transfection of oncogene constructs is much more cumbersome. However, in Wilms tumor, many alterations, including *WT1* loss-of-function, occur before the NPC stage, and electroporation might negatively affect kidney organoid differentiation in a monolayer format. However, it might be worth optimizing these conditions in order to test the effects of multiple genetic aberrations simultaneously.

4.10 Limitations and future perspectives of hiPSC-derived Wilms tumor organoids

Despite their strong benefits, iPSC-derived kidney organoids come with certain limitations that might affect their applicability in future studies.

First, kidney organoids are immature and show high congruence with cell types present in the fetal kidney of the first Trimester (Combes et al., 2019; Takasato et al., 2015; Wu et al., 2018). The relatively short generation time and fetal properties limit kidney organoids to the investigation of genetically defined pediatric cancers, as opposed to adult kidney tumors, which frequently require the accumulation of multiple genetic events over time. In addition, studying any kidney disease that relies on mature adult cell types, like specific transport proteins, might be precluded by the fetal nature of the system. It is therefore critical to evaluate the properties of the organoid system carefully when planning a new disease model. scRNA-seq studies have characterized different organoid systems and offer a resource for the kind and maturity of cells therein (Combes et al., 2019; Subramanian et al., 2019; Wu et al., 2018). Nevertheless, as delineated above, kidney organoid models have been developed for a variety of diseases and recapitulate many disease-relevant features. In addition, adaptations of the original kidney organoid protocols, like differentiation of kidney organoids on hydrogels or within a flow chamber, allow the generation of kidney organoids with higher maturity of cells and improved vasculature, that might be better suited for modeling certain diseases (reviewed in Little and Combes, 2019).

Second, consistent with our own observations, many publications report variability as a prevalent feature of organoids. A recent study used RNA-seq of whole organoids over time to assess the variability of organoids generated within a given experiment, across separately performed differentiation experiments and from different iPSC lines (Phipson et al., 2019). Indeed, the strongest variability occurred between organoids derived from separate differentiation experiments, and was reflected in different organoid maturation states, as well as the relative abundance of nephron elements and off-target populations. Considering this, it is readily conceivable that organoids are even more variable when generated in different labs or using different protocols (Kim et al., 2020; Little and Combes, 2019; Wu et al., 2018). As described, we have observed differences between organoids generated with the Taguchi/Brown protocol and organoids generated with the Morizane protocol, with respect to both, SIX2 expression and a LIN28 overexpression phenotype. A scRNA-seq study compared organoids derived from the Morizane and Little protocols and found relative differences in the abundance of nephron segments and off-target populations (Wu et al., 2018).

In addition to the intrinsic variability of such protocols, our *WT1* KO approach added another source of variability: use of an inducible Cas9 to create a gene KO inevitably creates a heterogeneous population of cells, of which a fraction are homozygous, heterozygous or wildtype.

Moreover, *WT1* loss seemed to increase apoptosis in developing organoids, which implies that the fraction of KO versus wildtype cells might be skewed upon organoid culture, resulting in an enrichment of actual wildtype cells. As mentioned, we have seen multiple *WT1*-expressing cells in *WT1* KO organoids. In fact, in our current system, we are unable to tell which cells in d21 organoids are actually derived from KO cells, and which are not. Consequentially, these “contaminating” cell types likely limit our ability to detect subtle gene expression changes between *WT1* KO and not-edited organoids. Therefore, more precise analyses of *WT1* KO effects would require either the use of a clonal *WT1* KO line, the purification of selected cell types, or scRNA-seq. Such analyses would also enable us to relate *SIX2*-expressing cells in *WT1* KO d21 organoids back to the time point of their developmental arrest.

Finally, as mentioned above, organoids derived from MM by nature lack the entire branch of UB derivatives. Recent efforts of combining MM and a single UB, both derived from mouse ESCs, with embryonic stromal cells resulted in more sophisticated organoids with branching morphogenesis, nephron structures and maintenance of a progenitor niche. In contrast, co-culture of human iPSC-derived MM and UB only resulted in limited branching, hinting at a requirement for stromal cells or further optimization of the protocol (Taguchi and Nishinakamura, 2017). In general, however, this shows that kidney organoids containing both functional UB and MM can be derived from hiPSCs, which may ultimately allow the generation of even more physiological organoids.

Along similar lines, kidney organoids lack the entire tissue environment of the kidney, including blood vessels, neurons and an immune system. This is important to consider especially in the context of tumorigenesis, since the tumor microenvironment strongly influences tumorigenesis and therapy response (Hanahan and Weinberg, 2011). However, as mentioned above, culture of organoids in a flow chamber has been shown to increase organoid vasculature, and co-culture approaches with endothelial cells in microfluidic devices, or with cancer-associated fibroblasts and immune cells have been proposed (discussed in Little and Combes, 2019). The latter approaches were mainly considered for patient biopsy-derived tumor organoids (Calandrini et al., 2020), but could be extended to hiPSC-derived tumor organoids to better recapitulate the tumor microenvironment.

We have provided evidence for the suitability of *WT1* KO organoids as an *in vitro* model for Wilms tumor. Based on this, it will now be interesting to extend this model by combining *WT1* KO with *CTNNB1* mutations or *IGF2* upregulation, which co-occur in Wilms tumor patients, and to perform more detailed transcriptional and functional experiments. We still do not know to which developmental stage arrested *SIX2*-expressing cells in *WT1* KO organoids correspond, and scRNA-seq would help uncovering this. In addition, it may be exciting to further analyze our

KO^{d9-11} or KO^{d11-14} organoids, which may provide insights into the roles of WT1 in post-NPC kidney development or podocyte differentiation. Moreover, with our model we have set a baseline for generating additional Wilms tumor models using other known alterations, like upregulation of *IGF2*, expression of the frequent *DROSHA* E1147K mutation or combinations of different events. We could also try to confirm the *MLLT1* phenotype found in mouse kidney organoids in our human system.

We have shown that overexpression of LIN28 paralogs and SIX2 Q177R alone are insufficient to induce a Wilms tumor phenotype under the given conditions. The advancement of gene editing technologies, however, allows us to combine different alterations in the same system. We could therefore test the effects of SIX2 Q177R, at best by introducing the mutation into the endogenous locus, together with the *DROSHA* E1147K mutation or with biallelic *IGF2* expression.

Reprogramming of Wilms tumor-derived cells into iPSCs might even offer the generation of Wilms tumor patient-specific organoids.

As an *in vitro* system, Wilms tumor organoids could also be used for both, genetic and compound screens. To this purpose, protocols are being adapted to grow larger batches of organoids in spinner flasks, and to use liquid handling systems to facilitate both organoid production and high-throughput screenings in multi-well plates (Czerniecki et al., 2018; Przepiorski et al., 2018). For example, by introducing a SIX2 reporter into the *WT1* line, such screenings could reveal pathways or compounds that are able to induce differentiation of SIX2-expressing NPCs in *WT1* KO organoids and restore nephron development. Considering that shut-down of LIN28 overexpression in the corresponding mouse model re-initiated nephrogenesis and resulted in tumor regression (Urbach et al., 2014), it is conceivable that induction of differentiation may be a viable treatment option for Wilms tumor. Using Dox-inducible constructs, Wilms tumor organoids represent a suitable system to investigate this.

In addition, kidney organoids could be used to study other pediatric tumors, like malignant rhabdoid tumor of the kidney (MRTK), which mostly arises due to inactivating mutations in *SMARCB1* that could be introduced into kidney organoids (Jackson et al., 2009).

In general, kidney organoid protocols continually evolve to provide better models for kidney development and for an ever-increasing variety of kidney disorders and cancers.

5. Conclusion

In this thesis, I have successfully established and characterized a human iPSC-derived kidney organoid system, and have probed different classes of Wilms tumor patient alterations.

We have shown that overexpression of LIN28A / B or SIX2 / SIX2 Q177R do not induce organoid overgrowth but rather result in impaired differentiation. We have mimicked *CTNNB1* gain-of-function mutations using chemical inhibition of GSK-3 β and subsequent activation of WNT signaling, and found dose-dependent defects in MET and nephron patterning. It remains to be determined to which extent these defects correlate with Wilms tumor patients. Finally, we have shown that WT1 depletion induces a developmental arrest of NPCs at a proliferating SIX2-EpCAM^{mid} transition state, which consequentially impairs differentiation into tubules and podocytes. Importantly, gene signatures of *WT1* KO organoids overlap with Wilms tumor patients and show the activation of muscle-specific genes, reflecting a specific subgroup of Wilms tumors associated with *WT1* lesions. Functional analyses using *in vitro* transplantation surrogates confirmed the expansion of *WT1* KO organoid-derived cells and maintenance of SIX2 expression during passaging.

Open questions remain, in particular to which stage of Wilms tumorigenesis the *WT1* KO organoids correspond: precursor lesions, like nephrogenic rests, or more advanced stages, which often harbor additional mutations like β -catenin stabilization or *IGF2* loss-of-imprinting. Our findings that SIX2-expressing cells can be propagated over a period of 60 days, withstanding differentiation-inducing cues and are able to expand upon transplantation into wildtype organoids in the absence of growth factors strongly support tumorigenic transformation.

Collectively, in this thesis, I built and characterized the first human iPSC-derived kidney organoid model for Wilms tumor and provide proof-of-concept for the applicability of kidney organoids to study pediatric tumorigenesis.

6. Methods

6.1 Cell culture

6.1.1 Culture of human iPSCs

ND41865 cells (ND5; Coriell, internal transfer from B. Roska lab) were cultured on Matrigel (Corning; #354277) in mTeSR1 medium (Stem Cell Technologies; # 85850). Medium was exchanged every 24 h. For passaging, cells were detached using TrypLE Express (Thermo Fisher #12604013), and single-cell suspensions were re-plated in mTeSR1 supplemented with 10 μ M ROCK inhibitor (Y-27632 Dihydrochloride; Sigma #Y0503-5MG).

WT29 cells and their derivatives were cultured on Laminin (Biolaminin 521 LN; Biolamina #LN521) in mTeSR1 medium plus 1% Penicillin-Streptomycin (Thermo Fisher #15140122). Cells were passaged using TrypLE as described above and re-plated in mTeSR1 medium supplemented with 2 μ M ROCK inhibitor (Y-27632 Dihydrochloride Tocris #1254).

6.1.2 Generation of kidney organoids

Taguchi/Brown protocol

Organoids from the ND5 line and its derivatives were generated using adapted versions of the protocols by Taguchi et al. (2014) (A. Taguchi and R. Nishinakamura, personal communication) for the generation of NPCs, and by Brown et al. (2015) for organoid culture (A. Brown, personal communication).

hiPSCs were detached, counted and plated at 10,000 cells per well into Nunclon™ Sphera™ 96-Well, Nunclon Sphera-Treated, U-Shaped-Bottom Microplates (Thermo Fisher #174925) in differentiation medium (Dulbecco's Modified Eagle Medium (DMEM)/F12 (Thermo Fisher #21331046), 2% B-27™ Supplement without Retinoic Acid (Thermo Fisher #12587010), 2 mM L-glutamine (Thermo Fisher #25030024), 1% Insulin-Transferrin-Selenium (ITS; Thermo Fisher #41400045), 1% MEM Non-essential amino acids solution (Thermo Fisher #11140035), 90 μ M β -mercaptoethanol (Sigma #M7522)), supplemented with 10 μ M ROCK inhibitor and 0.5 ng/ml BMP4 (R&D Systems #314-BP) (BY medium; d0). The plate was centrifuged briefly to ensure aggregation of cells into EBs. After 24 h, medium was changed to Differentiation Medium plus 1 ng/ml recombinant Activin A (R&D Systems #338_AC) and 20 ng/ml FGF2 (provided by Smith Lab, Cambridge) (AF2 medium). At d3, the medium was changed to Differentiation Medium supplemented with 1 ng/ml BMP4 and 10 μ M CHIR (provided by Steward Lab, Dresden) (BC10

Methods

medium). After 2 days, half of this medium was replaced with BC10 medium plus additional 10 μ M ROCK inhibitor (BC10Y), and at d7 half of this medium was again replaced with BC10Y medium. At d9, medium was changed to ABC3RY medium, containing 10 ng/ml Activin A, 3 ng/ml BMP4, 3 μ M CHIR, 0.1 μ M all trans-Retinoic Acid (Sigma #2625) and 10 μ M ROCK inhibitor. Finally, at d11, medium was changed to Differentiation Medium, supplemented with 1 μ M CHIR, 5 ng/ml FGF9 (R&D Systems #273-F9) and 10 μ M ROCK inhibitor (C1FY). Note: all medium changes were carried out by transferring single EBs into new wells with the next medium.

For organoid culture, single EBs were transferred onto polycarbonate filters (Millipore #VCTP01300) floating on organoid culture medium (DMEM/F12 supplemented with 8% KnockOut™ Serum Replacement (Thermo Fisher #10828028), 1% ITS, 2 mM L-glutamine, 50 μ M β -mercaptoethanol, 1% Penicillin-Streptomycin, 1% HEPES (1M, Thermo Fisher #15630056) and 3 μ M CHIR) in 24-well plates. Organoids were cultured for one week without any medium changes.

This protocol was only used for the ND5 line and its derivatives (Fig. 1 and 2).

Morizane protocol

Organoids from the WT29 hiPSC line and its derivatives were generated using an adapted version of the protocol by Morizane et al. (2015), see also Morizane and Bonventre (2017) (protocol adapted by R. Ungricht, NIBR, CBT).

HiPSCs were detached and counted using a Vi-CELL™ XR Cell Viability Analyzer (Beckmann). Cells were plated at densities of 500,000 to 600,000 cells per well into Laminin-coated 6-well plates in mTeSR1 plus ROCK inhibitor. After a minimum of 6 h, the mTeSR1 medium was removed and cells were gently washed with Dulbecco's Phosphate Buffered Saline (PBS; without magnesium and calcium; Thermo Fisher #14190169). Differentiation was induced by culturing cells in basic differentiation medium (BDM; advanced RPMI 1640 (Thermo Fisher #12633012), 1% Glutamax (Thermo Fisher #35050038), 1% Penicillin-Streptomycin) supplemented with 8 μ M CHIR (Tocris #4423) and 5 ng/ml human recombinant Noggin (Peprotech #120-10C) (= d0). At d2, the CHIR/Noggin medium was replaced. At d4, as soon as cell colonies contracted and showed pronounced bright halo-like outlines, medium was changed to BDM supplemented with 10 ng/ml recombinant Activin A protein (R&D Systems #338_AC). At d7, medium was changed to BDM supplemented with 10 ng/ml FGF9 (R&D Systems #273-F9). At d9, which marked the NPC state, cells were washed, dissociated from the cell culture dish using TrypLE and counted. For organoid culture, cells were seeded at 25,000 or 50,000 cells per well in 150 μ l of BDM supplemented with 3 μ M CHIR, 10 ng/ml FGF9 and 2 μ M ROCK Inhibitor into Corning® Costar® Ultra-Low

Attachment 96-well round bottom plates (Sigma #CLS7007-24EA). Surplus NPCs were frozen in CryoStor® CS10 (Stem Cell Technologies #7930). The plate was briefly centrifuged to help aggregation of cells. After at least 24 h, 100 µl of medium were removed and replaced with 150 µl of BDM plus 10 ng/ml FGF9. At d11, 100 µl of medium were removed and replaced with 100 µl of BDM plus 10 ng/ml FGF9. At d14, 100 µl of medium were replaced with 100 µl of BDM without growth factors. Like that, the medium was changed again at d16 and d18. If culture was extended beyond 21 days, medium was changed 3 times per week.

All experiments involving the WT29 line and its derivatives were done using this protocol (Fig. 3-24).

6.1.3 Dissociation of kidney organoids into single cells

Organoids were harvested into Falcon Tubes using a P-1000 pipette with the tip cut, and washed twice with PBS. Afterwards, a 1:1 mix of Non-enzymatic cell dissociation solution (Thermo Fisher #13151014) and 0.25% Trypsin-EDTA (Thermo Fisher #25200056) was added, and organoids were incubated at 37°C. After 10 minutes (mins), organoids were resuspended ten times to aid the dissociation. In case of remaining fragments, the suspension was returned to 37°C for an additional 10 mins. Afterwards, Trypsin activity was stopped by adding 10% fetal calf serum (FCS; Bioconcept #2-01F36-I) in PBS and cells were centrifuged. Cells were washed once more with 1% FCS and passed through a 50 µm filter (BD Biosciences #340632).

6.2 Measuring organoid growth

Organoid growth was measured based on brightfield images acquired every 24 h or as indicated, using an Incucyte® system. Organoid size was determined by defining objects in brightfield images by manually adjusting minimum area and maximum eccentricity based on images representing phenotypic extremes (very small, very big, a lot of debris, very deformed). These parameters need to be defined in each experiment. Before data export, brightfield object matrices were manually assessed and samples with faulty object detection were excluded.

6.3 Functional assays

6.3.1 Cleaved Caspase Assay

Organoids were grown as described. At d14, half of the cell culture medium was removed and replaced with BDM supplemented with CellEvent™ Caspase-3/7 Green Detection Reagent (dilution: 1:2000; Invitrogen #C10423). At d16, half of the medium was replaced with Caspase-containing medium as before. At d18, half of the medium was replaced with BDM only. Caspase activity was read-out every 12 h using an Incucyte® system (Essen BioScience). Organoid area was defined using brightfield objects with the following parameters: minimum area: 50,000 μm^2 ; maximum eccentricity: 0.85, which were selected based on representative images to exclude debris. Green fluorescence was measured using Top-Hat No Mask segmentation and a radius of 500 μm . Data is presented as mean green fluorescence intensity within the area of the organoid.

6.3.2 Mixing of *WT1* KO and GFP-expressing wildtype d9 NPCs

RFP-expressing *WT1* not-edited, KO^{iPSC} and $\text{KO}^{\text{d4-7}}$ d9 NPCs were mixed with freshly thawed NPCs derived from the WT29-iCas9-GFP hiPSC line at the indicated ratios to obtain a total of 50,000 cells per well. Cell mixes were plated into Corning® Costar® Ultra-Low Attachment 96-well round bottom plates in 150 μl BDM, supplemented with 3 μM CHIR, 10 ng/ml FGF9 and 2 μM ROCK inhibitor. The plate was briefly centrifuged to help aggregation of cells. Organoid culture was performed as described above. At d11, a fraction of single organoids was dissociated on the plate as described for flow cytometry analysis of single organoids (see Section 6.7.3). Samples were measured using the BD LSRFortessa™ HTS module and data was analyzed using Flow Jo. The remaining organoids were cultured until d21 or d30 and processed in the same way. A minimum of six organoids per condition were processed for cryosectioning and IF staining (see below).

We gated for RFP versus GFP in order to discriminate between cells of the *WT1* KO line and cells from the wildtype WT29-iCas9-GFP line. Heterogeneous GFP intensities resulted in contaminating GFP^{low} cells in the RFP gate. Using GFP only samples, we calculated the fraction of contaminating GFP^{low} cells in the RFP gate, which we defined as a normalization factor. Using this factor, we calculated the contaminating GFP fraction in the RFP gate for each sample, and added it to the GFP population and subtracted it from the RFP population. Like this, we obtained corrected fractions GFP and RFP-positive cells. In Fig. 21 and 22 “WT1 cells” reflects *WT1* not-edited, KO^{iPSC} and $\text{KO}^{\text{d4-7}}$ cells that were quantified using this method.

6.3.3 Serial passaging of cells derived from d21 organoids

WT1 not-edited and KO^{d4-7} d21 organoids were dissociated as described. Single cell suspensions were filtered and counted. Appropriate cell numbers were mixed with freshly thawed WT29-iCas9-GFP NPCs at the indicated ratios to a total of 50,000 cells per well. Cell mixes were re-seeded into Corning® Costar® Ultra-Low Attachment 96-well round bottom plates in 150 μ l BDM, supplemented with 3 μ M CHIR, 10 ng/ml FGF9 and 2 μ M ROCK inhibitor. The plate was briefly centrifuged to help aggregation of cells. Organoid culture was resumed as described above. After 12 days, organoids were harvested. A minimum of six organoids were processed for cryosectioning and IF staining, as described below. The remaining organoids were dissociated, filtered and counted as described. Cells from each condition were mixed again with freshly thawed WT29-iCas9-GFP NPCs at the same ratios as in the previous passage. Cells were plated and organoid culture was done as described. The remaining cells were fixed for flow cytometry analysis as described below. This was repeated for up to four passages.

Gating of GFP versus RFP to discriminate the wildtype GFP line from the *WT1* KO line and correction for contaminating GFP cells in the RFP gate was done as described in Section 6.3.2.

6.3.4 Transplantation of cells derived from d21 organoids or d9 NPCs into GFP-expressing wildtype organoids

WT1 not-edited and KO^{d4-7} d21 organoids were dissociated as described above. Single cell suspensions were filtered and counted. *WT1* not-edited d9 NPCs were thawed. We removed 100 μ l of a total of 200 μ l culture medium from d21 organoids generated from WT29-iCas9-GFP cells, and mechanically injured organoids by pipetting them up and down five times with a P-200 pipette. For culture in differentiation- / growth-promoting conditions, the indicated numbers of cells derived from not-edited or KO^{d4-7} d21 organoids and d9NPCs were resuspended in 100 μ l per well of BDM supplemented with 6 μ M CHIR, 20 ng/ml FGF9 and 4 μ M ROCK inhibitor, and added to the GFP organoids. The plate was briefly centrifuged to help aggregation. Organoid culture was resumed as described above for two weeks. Organoids were harvested and fixed for cryosectioning and IF staining as described below.

For culture in the absence of growth factors, dissociated KO^{d4-7} cells from d21 organoids were resuspended in 100 μ l per well of BDM, and added to the injured GFP organoids. The plate was briefly centrifuged to help aggregation. BDM was changed three times a week for two weeks. Organoids were harvested and fixed for cryosectioning and IF staining as described below.

6.4 Molecular biology: Generation of Dox-inducible Wilms tumor oncogene lines

Coding sequences of LIN28A, LIN28B and SIX2 were amplified from hiPSC cDNA and recombined into pDONR221 using Gateway technology (Thermo Fisher #11789020 and #11791020). Point mutation of SIX2 (SIX2 Q177R) was introduced by polymerase chain reaction (PCR). Final and intermediate PCR products were purified via Agarose gel electrophoresis (Thermo Fisher #17856) and gel purification (MinElute Gel Extraction Kit, Qiagen #28604).

Generate Dox-inducible *LIN28A* vector for ND5 cells:

The expression destination vector used for LIN28A overexpression in ND5 cells was pPB-TRE-DEST-rTA-pgk-hph. ND5 hiPSCs were transfected with the expression vector and pBase (Betschinger et al., 2013) using Lipofectamin™ 2000 (Thermo Fisher #11668019) in OptiMem Reduced Serum Medium (Thermo Fisher #319850629), and were selected for stable integration in the presence of 150 µg/ml HygromycinB (Thermo Fisher #10687010). For induction of the constructs, cells were treated with 1 µg/ml Dox.

Generate Dox-inducible mCherry-T2A-LIN28A, -LIN28B, -SIX2 and -SIX2 Q177R vectors for WT29 cells

Coding sequences were amplified from previously generated expression vectors. In two consecutive PCR steps, a T2A sequence was added to the N-terminus of the coding sequence and subsequently, both N- and C-terminal Gateway cloning sites were added. From these constructs, pDONR221-vectors were generated, which were recombined with the pPB-TRE-mCherry-DEST-rTA-HSV-neo expression destination vector using Gateway technology. WT29 hiPSCs were transfected with the expression vector and pBase (Betschinger et al., 2013) using Lipofectamin Stem™ (Thermo Fisher #STEM00015) in OptiMem Reduced Serum Medium (Thermo Fisher #319850629), and were selected for stable integration in the presence of 100 µg/ml G418 (Thermo Fisher #10131027). For induction of constructs, cells were treated with 1 µg/ml Dox.

6.5 Lentivirus production and transduction

Prior to transfection, HEK293T cells were seeded onto collagen I-coated 6-well tissue culture plates (BD biosciences #346400) in packaging medium (DMEM (Thermo Fisher #11965), supplemented with 10% FCS and 1% Non-essential amino acids (Thermo Fisher #11140050)). The next day, cells were transfected with *WT1* gRNA-containing vectors (pRSI16-U6-*WT1*gRNA_RFP-2A-Puro) and Collecta packaging mix (Collecta #CPC-K2A) using the TransIT™293 transfection reagent (Mirus Bio #MIR 2700) in OptiMem Reduced Serum Medium (Thermo Fisher #31985062). The next day, medium was changed to 1 ml of packaging medium for virus production. After 3 days, the virus-containing supernatant was collected, filtered through a 50 µm filter and aliquots were stored at -80°C until further use. For virus titration, WT29-iCas9 cells were seeded into 6-well plates (200,000 cells / well) in mTeSR1 medium supplemented with ROCK inhibitor. After 7 h, different volumes of viral supernatant were added to the cells. After three days with daily mTeSR1 medium changes, cells were detached and RFP fluorescence derived from the pRSI16-U6-*WT1*gRNA_RFP-2A-Puro vector was measured using a BD LSRFortessa™ flow cytometer. Based on this titration, WT29-iCas9 cells were transduced at a multiplicity of infection of 0.5, and infected cells were selected with puromycin (Thermo Fisher #A11138-03) for 6 days. Induction of Cas9 expression upon treatment with 0.2 µg/ml Dox.

6.6 RNA isolation, cDNA synthesis, qPCR

RNA was either isolated from cell suspensions or from dissociated organoids following the protocol of the RNeasy Mini Kit (Qiagen #74104) and the RNase-Free-DNase Set (Qiagen #79256). Samples were resuspended in RLT Lysis Buffer supplemented with 1% β-mercaptoethanol, and were stored at -80 °C until RNA isolation. RNA was eluted from columns in RNase-free water, and RNA concentrations were determined using a NanoDrop (Thermo Fisher).

CDNA was generated from a defined input of RNA (at least 400 ng) using SuperScript III Reverse Transcriptase (Thermo Fisher # 18080044). The cDNA was then diluted to obtain an input of 25 ng for qPCR, which was performed on a Step One Plus™ Real-Time PCR System (Thermo Fisher) using the TaqMan Fast Universal PCR Master Mix (2x) (Thermo Fisher # 4364103). Gene expression of selected markers was detected using probes from the Universal Probe Library (UPL, Roche) together with custom-designed primer pairs (see Appendix). QPCR was performed in technical duplicates and multiplexed with a *GAPDH* probe (Thermo Fisher # 4326317E). Cycle threshold (CT) values were normalized to *GAPDH* (Δ CT method) and, if applicable, normalized to controls ($\Delta\Delta$ CT method).

6.7 Flow cytometry and FACS

6.7.1 Live cells

For flow cytometry analysis and FACS of live cells based on fluorescent proteins, cells were detached from the cell culture dish, or organoids were dissociated into single cells, as described above. Cells were washed with 1% FCS in PBS and resuspended in flow cytometry buffer (2% FCS and 1 mM ethylenediaminetetraacetic acid (EDTA; Thermo Fisher #AM9260G) in PBS).

6.7.2 Flow cytometry of fixed and stained cells

For flow cytometry analysis of additional markers, dissociated cells from monolayer culture or organoids were fixed using the fixative of the BD Cytofix/Cytoperm Fixation/Permeabilization Kit (BD Biosciences #554714) for 20 mins at 4°C. Afterwards 0.4% bovine albumin fraction V solution (BSA, 7.5%, Thermo Fisher #15260037) in PBS was added and cells were centrifuged. Cells were resuspended in the permeabilization buffer of the BD Cytofix/Cytoperm Fixation/Permeabilization Kit and incubated for 10 mins at room temperature (RT). Afterwards, primary antibodies were diluted into this cell suspension and incubated at 4°C for 60 mins. Cells were washed three times and were then resuspended in permeabilization buffer that contained respective secondary antibodies. Cells were again incubated at 4°C, washed three times and resuspended in permeabilization buffer for flow analysis. Primary antibodies used: EPCAM-AF647 (Abcam #ab239273, 1:200); Ki-67/ Ki-67-FITC (eBioscience #11-5698-82, 1:200); SIX2 (Proteintech #11562-1-AP, 1:100); WT1 (Abcam #ab89901, 1:200). For secondary antibodies used, see List of materials (all diluted 1:500). Flow cytometry was performed on a BD LSRFortessa™ or BD LRSII™ device. Data was analyzed in Flow Jo.

6.7.3 High-throughput flow cytometry analysis

For analysis of single organoids, organoid culture medium was removed from the wells and organoids were washed twice with PBS. Afterwards a 1:1 mix of non-enzymatic cell dissociation solution and 0.25% Trypsin-EDTA was added, and organoids were incubated at 37°C. After 10 mins, organoids were resuspended using a P-200 multichannel pipette. In case of remaining fragments, the suspension was returned to 37°C for an additional 10 mins. Afterwards, dissociated cells were transferred into Corning® 96-well Clear V-Bottom TC-treated Microplates (Corning #3894) containing 10% FCS in PBS. Cells were centrifuged, washed with 1% FCS and resuspended in 0.4% BSA for flow cytometry analysis. Samples were analyzed using a High Throughput Sampler (HTS) on the BD LSRFortessa™ device. Data was analyzed in Flow Jo.

6.7.4 FACS-based purification of Wilms Tumor oncogene lines

The mCherry-T2A-LIN28A, -LIN28B, -SIX2 and -SIX2 Q177R hiPSC lines were cultured in the presence of 1 ug/ml Dox for 48 h. Afterwards cells were detached and prepared for FACS as described above. We measured mCherry intensity and sorted a population of 30% of cells around the mCherry peak. After the sort, cells were counted and plated back onto Laminin-coated plates in mTeSR1 supplemented with ROCK inhibitor. FACS was performed on BD FACSAria™ Fusion Cell Sorter.

6.8 Immunofluorescence staining of kidney organoids

Whole-mount-staining of kidney organoids

3D kidney organoids were harvested from polycarbonate filters, transferred into Eppendorf Tubes and washed with PBS. Organoid were fixed with 4% paraformaldehyde (PFA; Electron microscopy sciences #15710) in PBS for 20 mins at RT, and then washed three times with PBS. Afterwards, they were incubated in organoid blocking buffer (0.3% Triton X-100 and 5% normal donkey serum (Sigma #D9663-10ML) in PBS) for a minimum of 3 h at RT on a shaker. Organoids were washed once with PBS and incubated with primary antibodies in antibody dilution buffer (0.3% Triton and 1% BSA) in PBS overnight at 4°C. Afterwards, organoids were washed twice for 1 h and once for 5 h with PBS at RT on a shaker. Subsequently, organoids were incubated with secondary antibodies diluted in antibody dilution buffer overnight at 4°C. Afterwards, they were washed three times for 1 h with PBS. Nuclei were stained with Hoechst 33342 (Thermo Fisher #H3570) during the last wash. Organoids were then transferred onto Greiner Bio-One™ µClear™ 96-Well, Advanced TC-Treated, Flat-Bottom Microplates (Greiner Bio-One™ #655986) that had been pre-coated with Mussel Adhesive Protein (ACROBiosystems #MAP-O4012-1mg). Primary antibodies and dyes used: CDH1 (BD Biosciences #610181, 1:200); Hoechst 33342 (Thermo Fisher #H3570; 1:10000); LTL-Fluorescein (Vectorlabs FL-1321, 1:200); PODXL (R&D Systems #AF1658, 1:500); SIX2 (Proteintech #11562-1-AP, 1:100). For secondary antibodies used see List of materials (all diluted 1:500). Organoids were imaged using a Cell Voyager 7000S (CV7000S) Yokogawa system. Images were handled using Fiji.

Immunofluorescence staining of organoid cryosections

3D kidney organoids were pooled into Falcon Tubes and washed twice with PBS. They were fixed with 4% PFA in PBS for 20 mins at 4°C. Afterwards, organoids were washed three times with PBS. Then, PBS was fully removed and organoids were resuspended in 50% sucrose (Sigma #84097)

in PBS and stored at 4°C overnight. The next day, organoids were embedded in gelatin solution (7.5% gelatin from porcine skin (Millipore #48722) and 10% sucrose in PBS) overnight at 4°C. The next day, organoids were mounted with Q Path Tissue OCT Medium (VWR #0011243) to generate frozen blocks which were cut into 10-14 µm sections. The sections were washed with PBS for 10 mins at RT, and then incubated with blocking/permeabilization buffer (1% BSA and 0.2% Triton X-100 in PBS) for 30 mins at RT. If biotinylated antibodies were used, slides were incubated with blocking/permeabilization buffer for 15 mins, then with blocking/permeabilization buffer plus four drops per ml of Streptavidin block (Streptavidin/Biotin Blocking Kit; Vectorlabs #SP-2002) for 15 mins and then with blocking/permeabilization buffer plus four drops per ml of Biotin block for 15 mins. After a quick wash, slides were incubated with primary antibodies diluted into 1% BSA in PBS for 1 h at RT. Afterwards, slides were washed twice with PBS for each 10 mins, and were then incubated with secondary antibodies and Hoechst 33342 diluted into 1% BSA in PBS for 1 h at RT. After two additional washes with PBS for 10 mins each, slides were mounted in ProLong™ Diamond Antifade Mountant (Thermo Fisher #P36970). Primary antibodies used: CDH1 (BD Biosciences #610181, 1:200); EPCAM-AF647 (Abcam #ab239273, 1:200); Hoechst 33342 (Thermo Fisher #H3570; 1:10000); HOXD11 (Sigma #SAB1403944; 1:300); IGF2 (Thermo Fisher #MA5-17096; 1:200); Ki-67 (SolA15, eBioscience #14-5698-82, 1:200) (Ki-67 / Ki-67-FITC (SolA15, eBioscience #14-5698-82, 1:200); LHX1 (OriGene #TA504528; 1:1000); LTL-Biotinylated (Vectorlabs B-1325, 1:500); LIN28A (Cell Signaling #3978, 1:600); LIN28B (Cell Signaling #4196, 1:250); NPHS1 (R&D Systems #AF4269, 1:60); PAX2 (Invitrogen #71-6000; 1:100); PAX8 (Proteintech #10336-1-AP; 1:100); PODXL (R&D Systems #AF1658, 1:500); SIX1 (Cell Signaling #12891; 1:200), SIX2 (Proteintech #11562-1-AP, 1:100); WT1 (Abcam #ab89901; 1:200). For secondary antibodies used see List of materials (all diluted 1:500).

Images were acquired on a Zeiss LSM710 scanning head confocal microscope and images were handled using Fiji.

Brightfield imaging of kidney organoids

Brightfield images of kidney organoids were acquired either on an Olympus CKX53 system using the cellSens software, or on an Incucyte® system.

6.9 RNA-seq

RNA isolation was performed as described above and RNA concentrations were measured using a NanoDrop. RNA isolation and measurement of RNA concentrations were done by M. Rittirsch (FMI).

RNA-seq library preparation and sequencing were performed by the FMI Functional Genomics Facility, headed by Dr. Sebastien Smallwood. RNA-seq libraries of three independent biological replicates were prepared using the TruSeq mRNA Library preparation kit (Illumina #20020595). Sequencing was performed on an Illumina HiSeq2500 machine (50 bp single-end reads).

For comparison with published gene expression datasets derived from kidney organoids (Wu et al., 2018) (GSE118184) (Fig. 17A), scRNAseq reads of 218 iPSCs and of 25120 (Morizane protocol) and 82024 (Takasato protocol) cells from d26 organoids were normalized and collapsed, and log₂ fold changes (FCs) relative to iPSCs were calculated using a pseudocount of 1. Correlation coefficients are of 12817 genes detected in Wu et al. (2018) and the RNA-seq dataset reported in this thesis.

RNA-seq reads were aligned to the human GRCh38 genome using qAlign from the Bioconductor package QuasR (Gaidatzis et al., 2015).

Principle component analysis (PCA) (Fig. 17B) was performed using the `prcomp` function in R.

For identification of significantly changing genes, edgeR (Robinson and Oshlack, 2010) was used. Significant genes were identified as genes with an absolute FC greater than 3.0 and a false discovery rate of less than 0.001. For heatmap visualization (Fig. 17C) only significantly deregulated genes in at least one of the shown contrasts were considered (7,653 genes).

For calculating gene set overlaps (Fig. 18A), Fisher's exact test odds ratios were determined and enrichments over 100 permutations calculated as Z-scores.

Analyses of enriched gene sets (Fig. 18B) were performed using DAVID (Huang et al., 2009) for GO terms of biological processes.

For tSNE representation of scRNAseq data (Fig. 19) using the Bioconductor package SingleCellExperiment (Amezquita et al., 2020), the top 5% variable genes of week 16 fetal kidney scRNAseq (Hochane et al., 2019) (GSE114530) and d26 kidney organoids (Wu et al., 2018) (Morizane protocol) (GSE118184) were considered. Gene or gene set expression normalized to a random set of 2000 genes is depicted using smoothing.

For the comparison with kidney cancer patient data (Fig. 20), Wilms tumor (WT; Gadd et al., 2017), Kidney Chromophobe Carcinoma (KIRC; TGCA; Davis et al., 2014), Kidney Papillary Cell Carcinoma (KIRP; The Cancer Genome Atlas Research Network, 2016), and Kidney Clear Cell

Methods

Carcinoma (KIRC; TCGA; Creighton et al., 2013) datasets (TARGET-WT, TCGA-KICH, TCGA-KIRP, and TCGA-KIRC) were downloaded from GDC (<https://portal.gdc.cancer.gov>) using the TCGAbiolinks package from Bioconductor. Data sets were normalized and log₂ FCs calculated over the mean of respective control samples using a pseudocount of 1. Correlation coefficients are of the 7,653 genes defined in Fig. 17C. Unsupervised clustering was performed using the aheatmap function from the Bioconductor package NMF.

RNA-seq data analysis was performed by Dr. Jörg Betschinger with help from Dr. Michael Stadler and Dr. Panagiotis Papasaikas (FMI Computational Biology Facility).

7. List of materials

Cell lines

| Cell line | Feature | Resource |
|---|---------------------------------------|-------------------------------------|
| ND41865 (ND5) | Wildtype / parental | Coriell; obtained from B. Roska lab |
| ND5 - pPB-TRE-LIN28A-rTA-pgk-hph | LIN28A overexpression | This thesis |
| WT29 | Wildtype / parental | Kindly provided by M. Müller, NIBR |
| WT29-iCas9 | Dox-inducible Cas9 line | Ungricht et al. in preparation |
| WT29-iCas9-GFP | GFP-positive cells | Ungricht et al. in preparation |
| WT29 - pPB-TRE-mCherry-T2A-LIN28A-rTA-pgk-hph | mCherry and LIN28A overexpression | This thesis |
| WT29 - pPB-mCherry-T2A-LIN28B-pgk-hph | mCherry and LIN28B overexpression | This thesis |
| WT29 - pPB-TRE-mCherry-T2A-SIX2-pgk-hph | mCherry and SIX2 overexpression | This thesis |
| WT29 - pPB-TRE-mCherry-T2A-SIX2 Q177R-rTA-pgk-hph | mCherry and SIX2 Q177R overexpression | This thesis |
| WT29-iCas9 - <i>WT1</i> gRNA1 | Inducible <i>WT1</i> KO | This thesis |
| WT29-iCas9 - <i>WT1</i> gRNA2 | Inducible <i>WT1</i> KO | This thesis |
| WT29-iCas9 - <i>WT1</i> gRNA3 | Inducible <i>WT1</i> KO | This thesis |
| HEK293T/17 | Lentivirus production | ATCC #ATCC® CRL-11268™ |

Media

Differentiation medium (adapted from Taguchi et al. 2014)

| Component | Concentration | Resource |
|--|---------------|-------------------------|
| DMEM/F12 | 1X | Thermo Fisher #21331046 |
| B-27™ Supplement without Retinoic Acid | 2% | Thermo Fisher #12587010 |
| L-glutamine | 2 mM | Thermo Fisher #25030024 |
| Insulin-Transferrin-Selenium | 1% | Thermo Fisher #41400045 |
| MEM Non-essential amino acids solution | 1% | Thermo Fisher #11140035 |
| β-mercaptoethanol | 90 μM | Sigma #M7522 |

List of materials

Organoid culture medium (adapted from Brown et al., 2015)

| Component | Concentration | Resource |
|------------------------------------|---------------|-------------------------|
| DMEM/F12 | 1X | Thermo Fisher #21331046 |
| KnockOut™ Serum Replacement | 8% | Thermo Fisher #10828028 |
| Insulin-Transferrin-Selenium (ITS) | 1% | Thermo Fisher #41400045 |
| L-glutamine | 2 mM | Thermo Fisher #25030024 |
| β-mercaptoethanol | 50 μM | Sigma #M7522 |
| Penicillin-Streptomycin | 1% | Thermo Fisher #15140122 |
| HEPES | 1% | Thermo Fisher #15630056 |
| CHIR 99021 | 3 μM | Steward Lab, Dresden |

Chemicals and recombinant proteins

| Name | Concentration | Resource |
|--|--------------------|---------------------------|
| All trans-retinoic acid | 0.1 μM | Sigma #2625 |
| CHIR 99021 (gift) | Depending on assay | Steward Lab, Dresden |
| CHIR 99021 (purchased) | Depending on assay | Tocris # 4423; 10mg |
| Doxycycline | 0.2 – 1 μg/ml | Clonetech #631311 |
| FGF2 | 20 ng/ml | Smith Lab, Cambridge |
| Geneticin™ Selective Antibiotic (G418 Sulfate) | 100 μg/ml | Thermo Fisher #10131027 |
| human recombinant Noggin | 5 ng/ml | Peptotech #120-10C; 20μg |
| HygromycinB | 150 μg/ml | Thermo Fisher #10687010 |
| Lipofectamin Stem™ Transfection Reagent | - | Thermo Fisher #STEM00015 |
| Lipofectamin™ 2000 Transfection Reagent | - | Thermo Fisher #11668019 |
| Penicillin-Streptomycin | 1% | Thermo Fisher #15140122 |
| Puromycin | 1 μg/ml | Thermo Fisher #A11138-03 |
| Recombinant H/M/R Activin A Protein | 1 – 10 ng/ml | R&D Systems #338-AC; 50μg |
| Recombinant human BMP4 | 0.5 – 3 ng/ml | R&D Systems #314-BP |
| rhFGF9 | 10 ng/ml | R&D Systems #273-F9; 25μg |
| TransIT®-293 Transfection Reagent | - | Mirusbio #MIR 2700 |
| Y-27632 dihydrochloride | 2 – 10 μM | Tocris #1254; 10mg |

Kits

| Application | Resource |
|---|-------------------------|
| BD Cytofix/Cytoperm Fixation/Permeabilization Kit | BD Biosciences #554714 |
| Cellecta packaging mix (4:1 mix of the Gag/Pol & VSV-G) | Cellecta #CPC-K2A |
| CellEvent™ Caspase-3/7 Green Detection Reagent | Invitrogen # C10423 |
| Gateway BP Clonase II Enzyme mix | Thermo Fisher #11789020 |
| Gateway BP Clonase II Enzyme mix | Thermo Fisher #11791020 |
| MinElute Gel Extraction Kit | Qiagen #28604 |
| QIAGEN Plasmid Maxi Kit | Qiagen #12163 |
| QIAprep Spin Miniprep Kit | Qiagen #27106 |
| RNase-free DNase Set | Qiagen #79256 |
| RNeasy Mini Kit | Qiagen #74104 |
| Streptavidin/Biotin Blocking Kit | Vectorlabs # SP-2002 |
| TruSeq Stranded mRNA Library Prep | Illumina #20020595 |

Primary antibodies and dyes

| Target | Species | Application | Dilution | Resource |
|---------------------|----------------|--------------------|-----------------|--------------------------|
| E-CADHERIN | Mouse | IF | 1:200 | BD Biosciences #610181 |
| EPCAM-AF647 | Mouse | IF, Flow | 1:200 | Abcam #ab239273 |
| Hoechst 33342 | - | IF | 1:10000 | Thermo Fisher #H3570 |
| HOXD11 | Mouse | IF | 1:300 | Sigma #SAB1403944 |
| IGF2 | Mouse | IF | 1:200 | Thermo Fisher #MA5-17096 |
| Ki-67 (SolA15) | Rat | IF, Flow | 1:200 | eBioscience #14-5698-82 |
| Ki-67-FITC (SolA15) | Rat | IF, Flow | 1:200 | eBioscience #11-5698-82 |
| LHX1 | Mouse | IF | 1:2000 | OriGene #TA504528 |
| LIN28A | Rabbit | IF | 1:600 | Cell Signaling #3978 |
| LIN28B | Rabbit | IF | 1:250 | Cell Signaling #4196 |
| LTL, Fluorescein | - | IF | 1:200 | Vectorlabs #FL-1321 |
| LTL-Bio | - | IF | 1:500 | Vectorlabs #B-1325 |
| NPHS1 | Sheep | IF | 1:60 | R&D Systems #AF4269 |
| PAX2 | Rabbit | IF | 1:100 | Invitrogen #71-6000 |
| PAX8 | Rabbit | IF | 1:100 | Proteintech #10336-1-AP |
| PODXL | Goat | IF | 1:500 | R&D Systems #AF1658 |

List of materials

| | | | | |
|------|--------|----------|-------|-------------------------|
| SIX1 | Rabbit | IF | 1:200 | Cell Signaling #12891 |
| SIX2 | Rabbit | IF, Flow | 1:100 | Proteintech #11562-1-AP |
| WT1 | Rabbit | IF, Flow | 1:200 | Abcam #ab89901 |

Secondary antibodies

| Antibody | Fluorescent label | Dilution | Resource |
|--------------------|-----------------------|----------|------------------------|
| Donkey-anti-rabbit | Alexa Fluor 488 | 1:500 | Thermo Fisher #A-21206 |
| Donkey-anti-rabbit | Alexa Fluor 594 | 1:500 | Thermo Fisher #A-21207 |
| Donkey-anti-rabbit | Alexa Fluor 647 | 1:500 | Thermo Fisher #A-31573 |
| Donkey-anti-goat | Alexa Fluor 594 | 1:500 | Thermo Fisher #A-11058 |
| Donkey-anti-goat | Alexa Fluor 647 | 1:500 | Thermo Fisher #A-21447 |
| Donkey-anti-sheep | Alexa Fluor 488 | 1:500 | Thermo Fisher #A-11015 |
| Donkey-anti-mouse | Alexa Fluor 488 | 1:500 | Thermo Fisher #A-21202 |
| Donkey-anti-mouse | Alexa Fluor 594 | 1:500 | Thermo Fisher #A-21203 |
| Donkey-anti-mouse | Alexa Fluor 647 | 1:500 | Thermo Fisher #A-31571 |
| Donkey-anti-rat | Alexa Fluor 647 | 1:500 | Abcam #ab150155 |
| Streptavidin | Fluorescent Dye 633-I | 1:500 | Abnova # U0295 |

Plasmids

| Vector | Resource |
|----------------------------------|---|
| pPB_TRE-DEST-rTA-pgk-hph | This thesis; made from pPB_TRE-DEST-rTA-HSV-neo (Villegas et al., 2019) |
| pPB_TRE-mCherry-DEST-rTA-HSV-neo | Made by D. Olivieri from pPB_TRE-DEST-rTA-HSV-neo (Villegas et al., 2019) |
| pDONR221-LIN28A | This thesis |
| pDONR221-LIN28B | This thesis |
| pDONR221-SIX2 | This thesis |
| pDONR221-SIX2 Q177R | This thesis |
| pDONR221-T2A-LIN28A | This thesis |
| pDONR221-T2A-LIN28B | This thesis |
| pDONR221-T2A-SIX2 | This thesis |
| pDONR221-T2A-SIX2 Q177R | This thesis |
| pBase | Betschinger et al., 2013 |
| pRSI16-U6-WT1 gRNA_RFP-2A-Puro | Made at NIBR from pRSI16-U6-sh-UbiC-TagRFP-2A-Puro (Cellecta #SVSHU616-L) |

Cloning primers

| purpose | primer | sequence |
|---|--------|---|
| Generation of pDONRs | | |
| Gateway cloning LIN28A | Fwd | ggggacaagttgtacaaaaaagcaggcttcaccatgggctccgtgtccaacca |
| | Rev | ggggaccactttgtacaagaaagctgggtctcaattctgtgcctccggga |
| Gateway cloning LIN28B | Fwd | ggggacaagttgtacaaaaaagcaggcttcaccatggccgaaggcggggctag |
| | Rev | ggggaccactttgtacaagaaagctgggtcttatgtcttttctttttgaactgaa ggc |
| Gateway cloning SIX2 | Fwd | ggggacaagttgtacaaaaaagcaggcttcaccatgtccatgctgccaccttcg |
| | Rev | ggggaccactttgtacaagaaagctgggtcctaggagcccagggtccacgagg |
| mutagenesis SIX2 Q177R | | |
| | Fwd | ttcaagaaccggcgggcgcgaccggggcgcc |
| | Rev | ggccgcccggtcgcccggccggttctttaa |
| Generation of mCherry-T2A constructs | | |
| Gateway cloning; addition of T2A; universal primer step 2 | Fwd | ggggacaagttgtacaaaaaagcaggcttcaccgagggcagaggaagtctccta acatgcggtg |
| general rev primer step 1 + 2 | Rev | ggggaccactttgtacaagaaagctgggtc |
| Gateway cloning step 1 T2A-LIN28A | Fwd | gaagtctcctaacaatgcggtgacgtggaggagaatcctggccaatgggctccgt gtccaaccag |
| Gateway cloning step 1 T2A-LIN28B | Fwd | gaagtctcctaacaatgcggtgacgtggaggagaatcctggccaatggccaagg cggggctag |
| Gateway cloning step 1 T2A-SIX2 and -SIX2 Q177R | Fwd | gaagtctcctaacaatgcggtgacgtggaggagaatcctggccaatgtccatgctg cccaccttc |

Fwd = forward primer; Rev = reverse primer

gRNA sequences

| Target | # | sequence |
|--------|---|----------------------|
| WT1 | 1 | GGTGTGGCAGCCATAGACCG |
| WT1 | 2 | GCTGCCGGTGCAGCTGTCCG |
| WT1 | 3 | TGTGTTTGCAGCCACAGCAC |

Primers and UPL probes for qPCR

| transcript | primer 1 | primer 2 | UPL probe (Roche) |
|-------------------|------------------------|---------------------------|--------------------------|
| <i>CDH1</i> | ccccctgttggtgtctttatta | ggatgacacagcgtgagaga | 41 |
| <i>HOXA10</i> | cctacacgaagcaccagaca | cgctctcgagtaaggtacatattg | 78 |
| <i>HOXA11</i> | cggcagcagaggagaaaag | gtataggggcagcgctttt | 70 |
| <i>IGF2</i> | cccattcccatacacctta | caatgtggccaaactccttc | 20 |
| <i>LHX1</i> | cggacacactcggtaagatg | tgtacagctgatgttcaagtcattt | 20 |
| <i>LIN28A</i> | ctggaatccatccgtgtca | tctagacctccacagttgtagca | 22 |
| <i>LIN28B</i> | gccatgcacttcaactctcc | atctctgccctagcctcctg | 9 |
| <i>NANOG</i> | cagtctggacactggctgaa | cacgtggtttccaaacaaga | 55 |
| <i>NPHS1</i> | accagcttcccatcactac | gcagctggtcttcaggttct | 22 |
| <i>OSR1</i> | aggcaacgaagtccttagca | cagatacagggattacacttttgc | 52 |
| <i>PAX2</i> | aggcttgagattcagcaac | cggtaactagtggcggatcat | 74 |
| <i>PAX8</i> | agcaagatcctggcaggtta | ggcgtttgtagtcccaat | 22 |
| <i>PODXL</i> | gcgctgctgctactgttgt | ccgtagtagtctgggttgc | 74 |
| <i>SALL1</i> | ccctgtccacgctaagttc | ggctctgtccaatccag | 74 |
| <i>SIX2</i> | ggcaagtcggtgttaggc | ggctggatgatgagtggtct | 88 |
| <i>SLC12A1</i> | tcagtacgggctgatgaaca | aaaagattcccgcagtgatg | 85 |
| <i>TBXT</i> | ttcaaggagctcaccaatga | gaaggagtacatggcgttgg | 88 |
| <i>WT1</i> | gaggacgcctacagcag | agggtggctcctaagttcatctg | 85 |

8. Acknowledgements

First and foremost I want to express my gratitude to Jörg Betschinger for admitting me to his lab and for believing in this promising but challenging project for all these years. I'm happy and proud that we kept going and managed to turn it into something exciting!

I am deeply grateful to Philipp Hoppe and Rosemarie Ungricht at NIBR CBT for having me as a guest for 1.5 years. Without you, I would probably not have started working on the *WT1* knockout, which marked the turning point of my project. I'm really grateful for this exceptional opportunity, that you made me feel welcome, and for the numerous chats about the project, science or life.

I would like to thank the current and previous members of the Betschinger lab for your help and input. Thank you, Mel, for helping me out with countless RNA isolations, and Kim, for being my intern student. I also feel grateful to Lapo, Marie, Britta and particularly Laure at NIBR CBT for making me feel welcome and for your help throughout my time there.

A special thanks goes to my thesis committee, Helge Grosshans and Soeren Lienkamp. You have witnessed the whole path of this work and I've really appreciated your support and input throughout. Thank you, Helge, for being available also aside the TAC meetings. I always valued your help and advice a lot. Thank you very much Susan Gasser, for being my Faculty Representative and Antoine Peters, for chairing my thesis defense.

I would like to express my gratitude to all the FMI facilities that helped me throughout my PhD: Functional Genomics (Sebastien Smallwood) for help with RNA-seq, Bioinformatics (Michael Stadler and Panagiotis Papasaikas) for help with RNA-seq analysis, FAIM (Laurent Gelman, Steven Bourke, Jan Eglinger, Kathrin Volkmann) for help with imaging (LSM710!) and image processing, IT (Alan Naylor, Sjoerd van Eden and Thierry Vioget) for getting me access to the Novartis network and helping me with everyday computer issues, and Hubertus Kohler (FACS) for all the good hours in your lab and for letting me borrow one of the Flow Jo dongles for 2 months in a row.

I would like to thank Brigitte Gross Scherf (Botond Roska lab) for providing the ND5 line, and Matthias Müller (NIBR) for providing the WT29 line.

Thank you, Marietta Zinner, Philipp Hoppe and Philipp Koch for valuable feedback on my thesis.

I would like to thank the Boehringer Ingelheim Fonds for funding me for two years of my PhD and for creating such a great community of young scientists.

Acknowledgements

I feel grateful to Piera Cicchetti for always being available and supportive, and to Elida Keller for handling all kinds of PhD student issues. I'd also like to thank the many FMI admins I interacted with in the past years (especially Gabi, Isabella, Jitka and Thomas) for your timely support in all matters.

I am truly grateful for all the companions that I met during the time at the FMI, in particular Marietta, Seba and Jan, for countless coffee breaks, serious and light conversations and a lot of fun also outside the FMI. Without you, my PhD time would not have been the same. Thanks a lot to the members of the coolest office at the FMI (3.14!), my fellow student reps throughout these years, and everyone who made Happy Hours, Rhine swimming, PhD retreats, coffee breaks and the Annual Meetings fun.

Last but not least, I'm very grateful for all the support I got from outside the FMI bubble. From my family back in Northern Germany, my school friends, who are always excited when I talk about my mini-kidneys, my friends from my time in Freiburg just across the border and everyone I met in Basel.

Most importantly I couldn't feel more grateful to have Philipp by my side: thank you for being my anchor in the past years and for being my biggest fan.

9. References

- Alexandrov, L.B., Nik-Zainal, S., Wedge, D.C., Aparicio, S.A.J.R., Behjati, S., Biankin, A.V., Bignell, G.R., Bolli, N., Borg, A., Børresen-Dale, A.-L., et al. (2013). Signatures of mutational processes in human cancer. *Nature* *500*, 415–421.
- Ambros, V., and Horvitz, H.R. (1984). Heterochronic mutants of the nematode *Caenorhabditis elegans*. *Science* *226*, 409–416.
- Amezquita, R.A., Lun, A.T.L., Becht, E., Carey, V.J., Carpp, L.N., Geistlinger, L., Marini, F., Rue-Albrecht, K., Risso, D., Soneson, C., et al. (2020). Orchestrating single-cell analysis with Bioconductor. *Nat. Methods* *17*, 137–145.
- Amit, S., Hatzubai, A., Birman, Y., Andersen, J.S., Ben-Shushan, E., Mann, M., Ben-Neriah, Y., and Alkalay, I. (2002). Axin-mediated CKI phosphorylation of β -catenin at Ser 45: a molecular switch for the Wnt pathway. *Genes Dev.* *16*, 1066–1076.
- Balzeau, J., Menezes, M.R., Cao, S., and Hagan, J.P. (2017). The LIN28/let-7 Pathway in Cancer. *Front. Genet.* *8*, 1–16.
- Barak, H., Huh, S.-H., Chen, S., Jeanpierre, C., Martinovic, J., Parisot, M., Bole-Feysot, C., Nitschké, P., Salomon, R., Antignac, C., et al. (2012). FGF9 and FGF20 Maintain the Stemness of Nephron Progenitors in Mice and Man. *Dev. Cell* *22*, 1191–1207.
- Bariety, J., Mandet, C., Hill, G.S., and Bruneval, P. (2006). Parietal Podocytes in Normal Human Glomeruli. *J. Am. Soc. Nephrol.* *17*, 2770–2780.
- Ben-David, U., Beroukhi, R., and Golub, T.R. (2019). Genomic evolution of cancer models: perils and opportunities. *Nat. Rev. Cancer* *19*, 97–109.
- Berry, R.L., Ozdemir, D.D., Aronow, B., Lindström, N.O., Dudnakova, T., Thornburn, A., Perry, P., Baldock, R., Armit, C., Joshi, A., et al. (2015). Deducing the stage of origin of Wilms' tumours from a developmental series of Wt1-mutant mice. *Dis. Model. Mech.* *8*, 903–917.
- Betschinger, J., Nichols, J., Dietmann, S., Corrin, P.D., Paddison, P.J., and Smith, A. (2013). Exit from Pluripotency Is Gated by Intracellular Redistribution of the bHLH Transcription Factor Tfe3. *Cell* *153*, 335–347.
- Beurel, E., Grieco, S.F., and Jope, R.S. (2015). Glycogen synthase kinase-3 (GSK3): regulation, actions, and diseases. *Pharmacol. Ther.* *148*, 114–131.
- Bian, S., Repic, M., Guo, Z., Kavirayani, A., Burkard, T., Bagley, J.A., Krauditsch, C., and Knoblich, J.A. (2018). Genetically engineered cerebral organoids model brain tumor formation. *Nat. Methods* *15*, 631–639.
- Breslow, N., Beckwith, J.B., Ciol, M., and Sharples, K. (1988). Age Distribution of Wilms' Tumor: Report from the National Wilms' Tumor Study. *Cancer Res.* *48*, 1653–1657.
- Breslow, N., Olshan, A., Beckwith, J.B., and Green, D.M. (1993). Epidemiology of Wilms Tumor. *Med. Pediatr. Oncol.* *21*, 172–181.
- Brown, A.C., Muthukrishnan, S.D., and Oxburgh, L. (2015). A Synthetic Niche for Nephron Progenitor Cells. *Dev. Cell* *34*, 229–241.
- Burn, S.F., Webb, A., Berry, R.L., Davies, J.A., Ferrer-Vaquer, A., Hadjantonakis, A.K., Hastie, N.D., and Hohenstein, P. (2011). Calcium/NFAT signalling promotes early nephrogenesis. *Dev. Biol.* *352*, 288–298.

References

- Calandrini, C., Schutgens, F., Oka, R., Margaritis, T., Candelli, T., Mathijssen, L., Ammerlaan, C., Ineveld, R.L. van, Derakhshan, S., Haan, S. de, et al. (2020). An organoid biobank for childhood kidney cancers that captures disease and tissue heterogeneity. *Nat. Commun.* *11*, 1–14.
- Caricasole, A., Duarte, A., Larsson, S.H., Hastie, N.D., Little, M.H., Holmes, G., Todorov, I., and Ward, A. (1996). RNA binding by the Wilms tumor suppressor zinc finger proteins. *Proc. Natl. Acad. Sci.* *93*, 7562–7566.
- Cheng, H.-T., Kim, M., Valerius, M.T., Surendran, K., Schuster-Gossler, K., Gossler, A., McMahon, A.P., and Kopan, R. (2007). Notch2, but not Notch1, is required for proximal fate acquisition in the mammalian nephron. *Development* *134*, 801–811.
- Chung, E., Deacon, P., Marable, S., Shin, J., and Park, J.-S. (2016). Notch signaling promotes nephrogenesis by downregulating Six2. *Development* *143*, 3907–3913.
- Clevers, H. (2016). Modeling Development and Disease with Organoids. *Cell* *165*, 1586–1597.
- Combes, A.N., Wilson, S., Phipson, B., Binnie, B.B., Ju, A., Lawlor, K.T., Cebrian, C., Walton, S.L., Smyth, I.M., Moritz, K.M., et al. (2018). Haploinsufficiency for the Six2 gene increases nephron progenitor proliferation promoting branching and nephron number. *Kidney Int.* *93*, 589–598.
- Combes, A.N., Zappia, L., Er, P.X., Oshlack, A., and Little, M.H. (2019). Single-cell analysis reveals congruence between kidney organoids and human fetal kidney. *Genome Med.* *11*, 1–15.
- Creighton, C.J., Morgan, M., Gunaratne, P.H., Wheeler, D.A., Gibbs, R.A., Gordon Robertson, A., Chu, A., Beroukhim, R., Cibulskis, K., Signoretti, S., et al. (2013). Comprehensive molecular characterization of clear cell renal cell carcinoma. *Nature* *499*, 43–49.
- Cruz, N.M., Song, X., Czerniecki, S.M., Gulieva, R.E., Churchill, A.J., Kim, Y.K., Winston, K., Tran, L.M., Diaz, M.A., Fu, H., et al. (2017). Organoid cystogenesis reveals a critical role of microenvironment in human polycystic kidney disease. *Nat. Mater.* *16*, 1112–1119.
- Czerniecki, S.M., Cruz, N.M., Harder, J.L., Menon, R., Annis, J., Otto, E.A., Gulieva, R.E., Islas, L.V., Kim, Y.K., Tran, L.M., et al. (2018). High-Throughput Screening Enhances Kidney Organoid Differentiation from Human Pluripotent Stem Cells and Enables Automated Multidimensional Phenotyping. *Cell Stem Cell* *22*, 1–12.
- Davies, J.A., Lodomery, M., Hohenstein, P., Michael, L., Shafe, A., Spraggon, L., and Hastie, N. (2004). Development of an siRNA-based method for repressing specific genes in renal organ culture and its use to show that the Wt1 tumour suppressor is required for nephron differentiation. *Hum. Mol. Genet.* *13*, 235–246.
- Davis, C.F., Ricketts, C.J., Wang, M., Yang, L., Cherniack, A.D., Shen, H., Buhay, C., Kang, H., Kim, S.C., Fahey, C.C., et al. (2014). The Somatic Genomic Landscape of Chromophobe Renal Cell Carcinoma. *Cancer Cell* *26*, 319–330.
- Deacon, P., Concodora, C.W., Chung, E., and Park, J.-S. (2019). β -catenin regulates the formation of multiple nephron segments in the mouse kidney. *Sci. Rep.* *9*, 1–13.
- Dekel, B., Metsuyanin, S., Schmidt-Ott, K.M., Fridman, E., Jacob-Hirsch, J., Simon, A., Pinthus, J., Mor, Y., Barasch, J., Amariglio, N., et al. (2006). Multiple Imprinted and Stemness Genes Provide a Link between Normal and Tumor Progenitor Cells of the Developing Human Kidney. *Cancer Res.* *66*, 6040–6049.
- Dong, L., Pietsch, S., and Englert, C. (2015a). Towards an understanding of kidney diseases associated with WT1 mutations. *Kidney Int.* *88*, 684–690.

- Dong, L., Pietsch, S., Tan, Z., Perner, B., Sierig, R., Kruspe, D., Groth, M., Witzgall, R., Gröne, H.-J., Platzer, M., et al. (2015b). Integration of Cistromic and Transcriptomic Analyses Identifies *Nphs2*, *Ma6b*, and *Magi2* as Wilms' Tumor 1 Target Genes in Podocyte Differentiation and Maintenance. *J. Am. Soc. Nephrol.* *26*, 2118–2128.
- Drake, K.A., Chaney, C.P., Das, A., Roy, P., Kwartler, C.S., Rakheja, D., and Carroll, T.J. (2020). Stromal β -catenin activation impacts nephron progenitor differentiation in the developing kidney and may contribute to Wilms tumor. *Dev. Camb. Engl.* *147*.
- Drummond, I.A., Madden, S.L., Rohwer-Nutter, P., Bell, G.I., Sukhatme, V.P., and Rauscher, F.J. (1992). Repression of the insulin-like growth factor II gene by the Wilms tumor suppressor *WT1*. *Science* *257*, 674–678.
- Essafi, A., Webb, A., Berry, R.L., Slight, J., Burn, S.F., Spraggon, L., Velecela, V., Martinez-Estrada, O.M., Wiltshire, J.H., Roberts, S.G.E., et al. (2011). A *Wt1*-controlled chromatin switching mechanism underpins tissue-specific *Wnt4* activation and repression. *Dev. Cell* *21*, 559–574.
- Forbes, T.A., Howden, S.E., Lawlor, K., Phipson, B., Maksimovic, J., Hale, L., Wilson, S., Quinlan, C., Ho, G., Holman, K., et al. (2018). Patient-iPSC-Derived Kidney Organoids Show Functional Validation of a Ciliopathic Renal Phenotype and Reveal Underlying Pathogenetic Mechanisms. *Am. J. Hum. Genet.* *102*, 816–831.
- Freedman, B.S., Brooks, C.R., Lam, A.Q., Fu, H., Morizane, R., Agrawal, V., Saad, A.F., Li, M.K., Hughes, M.R., Werff, R.V., et al. (2015). Modelling kidney disease with CRISPR-mutant kidney organoids derived from human pluripotent epiblast spheroids. *Nat. Commun.* *6*, 1–13.
- Fukuzawa, R., Heathcott, R.W., More, H.E., and Reeve, A.E. (2007). Sequential *WT1* and *CTNNB1* mutations and alterations of β -catenin localisation in intralobar nephrogenic rests and associated Wilms tumours: two case studies. *J. Clin. Pathol.* *60*, 1013–1016.
- Gadd, S., Huff, V., Huang, C.-C., Ruteshouser, E.C., Dome, J.S., Grundy, P.E., Breslow, N., Jennings, L., Green, D.M., Beckwith, J.B., et al. (2012). Clinically Relevant Subsets Identified by Gene Expression Patterns Support a Revised Ontogenic Model of Wilms Tumor: A Children's Oncology Group Study. *Neoplasia* *14*, 742–756.
- Gadd, S., Huff, V., Walz, A.L., Ooms, A.H.A.G., Armstrong, A.E., Gerhard, D.S., Smith, M.A., Auvil, J.M.G., Meerzaman, D., Chen, Q.-R., et al. (2017). A Children's Oncology Group and TARGET initiative exploring the genetic landscape of Wilms tumor. *Nat. Genet.* *49*, 1487–1494.
- Gaidatzis, D., Lerch, A., Hahne, F., and Stadler, M.B. (2015). QuasR: quantification and annotation of short reads in R. *Bioinformatics* *31*, 1130–1132.
- Garvin, A.J., Sullivan, J.L., Bennett, D.D., Stanley, W.S., Inabnett, T., and Sens, D.A. (1987). The *in vitro* growth, heterotransplantation, and immunohistochemical characterization of the blastemal component of Wilms' tumor. *Am. J. Pathol.* *129*, 353–363.
- Glezerman, I.G., and Jaimes, E.A. (2016). Chapter 11. Chemotherapy and Kidney Injury. *Am. Soc. Nephrol. Onco-Nephrol. Curric.* 1–10.
- Grill, C., Sunitsch, S., Hatz, M., Hauser-Kronberger, C., Leuschner, I., Hoefler, G., and Guertl, B. (2011). Activation of beta-catenin is a late event in the pathogenesis of nephroblastomas and rarely correlated with genetic changes of the *APC* gene. *Pathology (Phila.)* *43*, 702–706.
- Hale, L.J., Howden, S.E., Phipson, B., Lonsdale, A., Er, P.X., Ghobrial, I., Hosawi, S., Wilson, S., Lawlor, K.T., Khan, S., et al. (2018). 3D organoid-derived human glomeruli for personalised podocyte disease modelling and drug screening. *Nat. Commun.* *9*, 1–17.
- Hanahan, D., and Weinberg, R.A. (2011). Hallmarks of Cancer: The Next Generation. *Cell* *144*, 646–674.

References

- Hartman, H.A., Lai, H.L., and Patterson, L.T. (2007). Cessation of Renal Morphogenesis in Mice. *Dev. Biol.* *310*, 379–387.
- Hastie, N.D. (2017). Wilms' tumour 1 (WT1) in development, homeostasis and disease. *Development* *144*, 2862–2872.
- Hidalgo, M., Amant, F., Biankin, A.V., Budinská, E., Byrne, A.T., Caldas, C., Clarke, R.B., Jong, S. de, Jonkers, J., Mælandsmo, G.M., et al. (2014). Patient-Derived Xenograft Models: An Emerging Platform for Translational Cancer Research. *Cancer Discov.* *4*, 998–1013.
- Hinchliffe, S., Sargent, P., Howard, C., Chan, Y., and van Velzen, D. (1991). Human intrauterine renal growth expressed in absolute number of glomeruli assessed by the disector method and Cavalieri principle. *Lab Invest* *64*, 777–784.
- Hochane, M., Berg, P.R. van den, Fan, X., Bérenger-Currias, N., Adegeest, E., Bialecka, M., Nieveen, M., Menschaart, M., Lopes, S.M.C. de S., and Semrau, S. (2019). Single-cell transcriptomics reveals gene expression dynamics of human fetal kidney development. *PLOS Biol.* *17*, 1–31.
- Hohenstein, P., Pritchard-Jones, K., and Charlton, J. (2015). The yin and yang of kidney development and Wilms' tumors. *Genes Dev.* *29*, 467–482.
- Hu, Q., Gao, F., Tian, W., Ruteshouser, E.C., Wang, Y., Lazar, A., Stewart, J., Strong, L.C., Behringer, R.R., and Huff, V. (2011). Wt1 ablation and Igf2 upregulation in mice result in Wilms tumors with elevated ERK1/2 phosphorylation. *J. Clin. Invest.* *121*, 174–183.
- Huang, D.W., Sherman, B.T., and Lempicki, R.A. (2009). Systematic and integrative analysis of large gene lists using DAVID bioinformatics resources. *Nat. Protoc.* *4*, 44–57.
- Huang, L., Mokkapatil, S., Hu, Q., Ruteshouser, E.C., Hicks, M.J., and Huff, V. (2016). Nephron Progenitor But Not Stromal Progenitor Cells Give Rise to Wilms Tumors in Mouse Models with β -Catenin Activation or Wt1 Ablation and Igf2 Upregulation. *Neoplasia N. Y. N* *18*, 71–81.
- Huff, V. (2011). Wilms' tumours: about tumour suppressor genes, an oncogene and a chameleon gene. *Nat. Rev. Cancer* *11*, 111–121.
- Humphreys, B.D., Valerius, M.T., Kobayashi, A., Mugford, J.W., Soeung, S., Duffield, J.S., McMahon, A.P., and Bonventre, J.V. (2008). Intrinsic Epithelial Cells Repair the Kidney after Injury. *Cell Stem Cell* *2*, 284–291.
- Jackson, E.M., Sievert, A.J., Gai, X., Hakonarson, H., Judkins, A.R., Tooke, L., Perin, J.C., Xie, H., Shaikh, T.H., and Biegel, J.A. (2009). Genomic Analysis Using High-Density Single Nucleotide Polymorphism-Based Oligonucleotide Arrays and Multiplex Ligation-Dependent Probe Amplification Provides a Comprehensive Analysis of INI1/SMARCB1 in Malignant Rhabdoid Tumors. *Clin. Cancer Res.* *15*, 1923–1930.
- Kann, M., Ettou, S., Jung, Y.L., Lenz, M.O., Taglienti, M.E., Park, P.J., Schermer, B., Benzing, T., and Kreidberg, J.A. (2015). Genome-Wide Analysis of Wilms' Tumor 1-Controlled Gene Expression in Podocytes Reveals Key Regulatory Mechanisms. *J. Am. Soc. Nephrol.* *26*, 2097–2104.
- Karner, C.M., Das, A., Ma, Z., Self, M., Chen, C., Lum, L., Oliver, G., and Carroll, T.J. (2011). Canonical Wnt9b signaling balances progenitor cell expansion and differentiation during kidney development. *Development* *138*, 1247–1257.
- Kim, S., and Jeong, S. (2019). Mutation Hotspots in the β -Catenin Gene: Lessons from the Human Cancer Genome Databases. *Mol. Cells* *42*, 8–16.
- Kim, J., Koo, B.-K., and Knoblich, J.A. (2020). Human organoids: model systems for human biology and medicine. *Nat. Rev. Mol. Cell Biol.* *21*, 571–584.

- Kispert, A., Vainio, S., and McMahon, A.P. (1998). Wnt-4 is a mesenchymal signal for epithelial transformation of metanephric mesenchyme in the developing kidney. *Development* 125, 4225–4234.
- Knudson, A.G., Jr, and Strong, L.C. (1972). Mutation and Cancer: A Model for Wilms' Tumor of the Kidney. *J. Natl. Cancer Inst.* 48, 313–324.
- Kobayashi, A., Valerius, M.T., Mugford, J.W., Carroll, T.J., Self, M., Oliver, G., and McMahon, A.P. (2008). Six2 Defines and Regulates a Multipotent Self-Renewing Nephron Progenitor Population throughout Mammalian Kidney Development. *Cell Stem Cell* 3, 169–181.
- Koesters, R., Ridder, R., Kopp-Schneider, A., Betts, D., Adams, V., Niggli, F., Briner, J., and Doeberitz, M. von K. (1999). Mutational Activation of the β -Catenin Proto-Oncogene Is a Common Event in the Development of Wilms' Tumors. *Cancer Res.* 59, 3880–3882.
- Koesters, R., Niggli, F., von Knebel Doeberitz, M., and Stallmach, T. (2003). Nuclear accumulation of beta-catenin protein in Wilms' tumours. *J. Pathol.* 199, 68–76.
- Koyanagi-Aoi, M., Ohnuki, M., Takahashi, K., Okita, K., Noma, H., Sawamura, Y., Teramoto, I., Narita, M., Sato, Y., Ichisaka, T., et al. (2013). Differentiation-defective phenotypes revealed by large-scale analyses of human pluripotent stem cells. *Proc. Natl. Acad. Sci.* 110, 20569–20574.
- Kreidberg, J.A., Sariola, H., Loring, J.M., Maeda, M., Pelletier, J., Housman, D., and Jaenisch, R. (1993). WT-1 is required for early kidney development. *Cell* 74, 679–691.
- Kruber, P., Angay, O., Winkler, A., Bösl, M.R., Kneitz, S., Heinze, K.G., and Gessler, M. (2019). Loss or oncogenic mutation of DRISHA impairs kidney development and function, but is not sufficient for Wilms tumor formation. *Int. J. Cancer* 144, 1391–1400.
- Kuure, S., Popsueva, A., Jakobson, M., Sainio, K., and Sariola, H. (2007). Glycogen Synthase Kinase-3 Inactivation and Stabilization of β -Catenin Induce Nephron Differentiation in Isolated Mouse and Rat Kidney Mesenchymes. *J. Am. Soc. Nephrol.* 18, 1130–1139.
- Lancaster, M.A., and Huch, M. (2019). Disease modelling in human organoids. *Dis. Model. Mech.* 12, 1–14.
- Lancaster, M.A., and Knoblich, J.A. (2014). Organogenesis in a dish: Modeling development and disease using organoid technologies. *Science* 345, 283–293.
- Lindström, N.O., Lawrence, M.L., Burn, S.F., Johansson, J.A., Bakker, E.R., Ridgway, R.A., Chang, C.-H., Karolak, M.J., Oxburgh, L., Headon, D.J., et al. (2015). Integrated β -catenin, BMP, PTEN, and Notch signalling patterns the nephron. *ELife* 4, 1–29.
- Lindström, N.O., Tran, T., Guo, J., Rutledge, E., Parvez, R.K., Thornton, M.E., Grubbs, B., McMahon, J.A., and McMahon, A.P. (2018a). Conserved and Divergent Molecular and Anatomic Features of Human and Mouse Nephron Patterning. *J. Am. Soc. Nephrol.* ASN.2017091036.
- Lindström, N.O., De Sena Brandine, G., Tran, T., Ransick, A., Suh, G., Guo, J., Kim, A.D., Parvez, R.K., Ruffins, S.W., Rutledge, E.A., et al. (2018b). Progressive recruitment of mesenchymal progenitors reveals a time-dependent process of cell fate acquisition in mouse and human nephrogenesis. *Dev. Cell* 45, 651–660.
- Lindström, N.O., Guo, J., Kim, A.D., Tran, T., Guo, Q., Brandine, G.D.S., Ransick, A., Parvez, R.K., Thornton, M.E., Basking, L., et al. (2018c). Conserved and Divergent Features of Mesenchymal Progenitor Cell Types within the Cortical Nephrogenic Niche of the Human and Mouse Kidney. *J. Am. Soc. Nephrol.* 29, 806–824.
- Little, M.H., and Combes, A.N. (2019). Kidney organoids: accurate models or fortunate accidents. *Genes Dev.* 33, 1319–1345.

References

- Little, M.H., Combes, A.N., and Takasato, M. (2016). Understanding kidney morphogenesis to guide renal tissue regeneration. *Nat. Rev. Nephrol.* *12*, 624–635.
- Liu, Z., Lou, H., Xie, K., Wang, H., Chen, N., Aparicio, O.M., Zhang, M.Q., Jiang, R., and Chen, T. (2017). Reconstructing cell cycle pseudo time-series via single-cell transcriptome data. *Nat. Commun.* *8*, 1–9.
- Ma, X., Liu, Y., Liu, Y., Alexandrov, L.B., Edmonson, M.N., Gawad, C., Zhou, X., Li, Y., Rusch, M.C., Easton, J., et al. (2018). Pan-cancer genome and transcriptome analyses of 1,699 paediatric leukaemias and solid tumours. *Nature* *555*, 371–376.
- Miller, R.W., Young, J.L., and Novakovic, B. (1995). Childhood cancer. *Cancer* *75*, 395–405.
- Miller-Hodges, E., and Hohenstein, P. (2012). WT1 in disease: shifting the epithelial-mesenchymal balance. *J. Pathol.* *226*, 229–240.
- Miyagawa, K., Kent, J., Moore, A., Charlieu, J.-P., Little, M.H., Williamson, K.A., Kelsey, A., Brown, K.W., Hassam, S., Briner, J., et al. (1998). Loss of WT1 function leads to ectopic myogenesis in Wilms' tumour. *Nat. Genet.* *18*, 15–17.
- Morizane, R., and Bonventre, J.V. (2017a). Kidney Organoids: A Translational Journey. *Trends Mol. Med.* *23*, 246–263.
- Morizane, R., and Bonventre, J.V. (2017b). Generation of nephron progenitor cells and kidney organoids from human pluripotent stem cells. *Nat. Protoc.* *12*, 195–207.
- Morizane, R., Lam, A.Q., Freedman, B.S., Kishi, S., Valerius, M.T., and Bonventre, J.V. (2015). Nephron organoids derived from human pluripotent stem cells model kidney development and injury. *Nat. Biotechnol.* *33*, 1193–1200.
- Motamedi, F.J., Badro, D.A., Clarkson, M., Lecca, M.R., Bradford, S.T., Buske, F.A., Saar, K., Hübner, N., Brändli, A.W., and Schedl, A. (2014). WT1 controls antagonistic FGF and BMP-pSMAD pathways in early renal progenitors. *Nat. Commun.* *5*, 1–14.
- Murphy, A.J., Chen, X., Pinto, E.M., Williams, J.S., Clay, M.R., Pounds, S.B., Cao, X., Shi, L., Lin, T., Neale, G., et al. (2019). Forty-five patient-derived xenografts capture the clinical and biological heterogeneity of Wilms tumor. *Nat. Commun.* *10*, 1–13.
- Nguyen, L.H., and Zhu, H. (2015). Lin28 and let-7 in cell metabolism and cancer. *Transl. Pediatr.* *4*, 4–11.
- Nishinakamura, R. (2019). Human kidney organoids: progress and remaining challenges. *Nat. Rev. Nephrol.* *15*, 613–624.
- Nusse, R., and Clevers, H. (2017). Wnt/ β -Catenin Signaling, Disease, and Emerging Therapeutic Modalities. *Cell* *169*, 985–999.
- Ogawa, J., Pao, G.M., Shokhirev, M.N., and Verma, I.M. (2018). Glioblastoma Model Using Human Cerebral Organoids. *Cell Rep.* *23*, 1220–1229.
- Ohnishi, K., Semi, K., Yamamoto, T., Shimizu, M., Tanaka, A., Mitsunaga, K., Okita, K., Osafune, K., Arioka, Y., Maeda, T., et al. (2014). Premature Termination of Reprogramming In Vivo Leads to Cancer Development through Altered Epigenetic Regulation. *Cell* *156*, 663–677.
- Osafune, K., Takasato, M., Kispert, A., Asashima, M., and Nishinakamura, R. (2006). Identification of multipotent progenitors in the embryonic mouse kidney by a novel colony-forming assay. *Development* *133*, 151–161.
- Park, J.-S., Valerius, M.T., and McMahon, A.P. (2007). Wnt/ β -catenin signaling regulates nephron induction during mouse kidney development. *Development* *134*, 2533–2539.

- Park, J.-S., Ma, W., O'Brien, L.L., Chung, E., Guo, J.-J., Cheng, J.-G., Valerius, M.T., McMahon, J.A., Wong, W.H., and McMahon, A.P. (2012). Six2 and Wnt Regulate Self-Renewal and Commitment of Nephron Progenitors through Shared Gene Regulatory Networks. *Dev. Cell* 23, 637–651.
- Park, S., Bernard, A., Bove, K.E., Sens, D.A., Hazen-Martin, D.J., Garvin, A.J., and Haber, D.A. (1993). Inactivation of WT1 in nephrogenic rests, genetic precursors to Wilms' tumour. *Nat. Genet.* 5, 363–367.
- Perlman, E.J., Gadd, S., Arold, S.T., Radhakrishnan, A., Gerhard, D.S., Jennings, L., Huff, V., Auvil, J.M.G., Davidsen, T.M., Dome, J.S., et al. (2015). MLLT1 YEATS domain mutations in clinically distinctive Favourable Histology Wilms tumours. *Nat. Commun.* 6, 1–10.
- Phipson, B., Er, P.X., Combes, A.N., Forbes, T.A., Howden, S.E., Zappia, L., Yen, H.-J., Lawlor, K.T., Hale, L.J., Sun, J., et al. (2019). Evaluation of variability in human kidney organoids. *Nat. Methods* 16, 79–87.
- Pode-Shakked, N., Gershon, R., Tam, G., Omer, D., Gnatek, Y., Kanter, I., Oriel, S., Katz, G., Harari-Steinberg, O., Kalisky, T., et al. (2017). Evidence of In Vitro Preservation of Human Nephrogenesis at the Single-Cell Level. *Stem Cell Rep.* 9, 279–291.
- Poladia, D.P., Kish, K., Kutay, B., Hains, D., Kegg, H., Zhao, H., and Bates, C.M. (2006). Role of fibroblast growth factor receptors 1 and 2 in the metanephric mesenchyme. *Dev. Biol.* 291, 325–339.
- Przepiorski, A., Sander, V., Tran, T., Hollywood, J.A., Sorrenson, B., Shih, J.-H., Wolvetang, E.J., McMahon, A.P., Holm, T.M., and Davidson, A.J. (2018). A Simple Bioreactor-Based Method to Generate Kidney Organoids from Pluripotent Stem Cells. *Stem Cell Rep.* 11, 1–15.
- Rakheja, D., Chen, K.S., Liu, Y., Shukla, A.A., Schmid, V., Chang, T.-C., Khokhar, S., Wickiser, J.E., Karandikar, N.J., Malter, J.S., et al. (2014). Somatic mutations in DROSHA and DICER1 impair microRNA biogenesis through distinct mechanisms in Wilms tumours. *Nat. Commun.* 2, 1–10.
- Ramalingam, H., Fessler, A.R., Das, A., Valerius, M.T., Basta, J., Robbins, L., Brown, A.C., Oxburgh, L., McMahon, A.P., Rauchman, M., et al. (2018). Disparate levels of beta-catenin activity determine nephron progenitor cell fate. *Dev. Biol.* 440, 13–21.
- Randjelovic, P., Veljkovic, S., Stojiljkovic, N., Sokolovic, D., and Ilic, I. (2017). Gentamicin nephrotoxicity in animals: Current knowledge and future perspectives. *EXCLI J.* 16, 388–399.
- Rivera, M.N., and Haber, D.A. (2005). Wilms' tumour: connecting tumorigenesis and organ development in the kidney. *Nat. Rev. Cancer* 5, 699–712.
- Robinson, M.D., and Oshlack, A. (2010). A scaling normalization method for differential expression analysis of RNA-seq data. *Genome Biol.* 11, 1–9.
- Royer-Pokora, B., Busch, M., Beier, M., Duhme, C., de Torres, C., Mora, J., Brandt, A., and Royer, H.-D. (2010). Wilms tumor cells with WT1 mutations have characteristic features of mesenchymal stem cells and express molecular markers of paraxial mesoderm. *Hum. Mol. Genet.* 19, 1651–1668.
- Schumacher, V., Schneider, S., Figge, A., Wildhardt, G., Harms, D., Schmidt, D., Weirich, A., Ludwig, R., and Royer-Pokora, B. (1997). Correlation of germ-line mutations and two-hit inactivation of the WT1 gene with Wilms tumors of stromal-predominant histology. *Proc. Natl. Acad. Sci.* 94, 3972–3977.
- Schutgens, F., Rookmaaker, M.B., Margaritis, T., Rios, A., Ammerlaan, C., Jansen, J., Gijzen, L., Vormann, M., Vonk, A., Viveen, M., et al. (2019). Tubuloids derived from human adult kidney and urine for personalized disease modeling. *Nat. Biotechnol.* 37, 303–313.

References

- Scott, R.H., Stiller, C.A., Walker, L., and Rahman, N. (2006). Syndromes and constitutional chromosomal abnormalities associated with Wilms tumour. *J. Med. Genet.* *43*, 705–715.
- Scott, R.H., Murray, A., Baskcomb, L., Turnbull, C., Loveday, C., Al-Saadi, R., Williams, R., Breatnach, F., Gerrard, M., Hale, J., et al. (2012). Stratification of Wilms tumor by genetic and epigenetic analysis. *Oncotarget* *3*, 327–335.
- Self, M., Lagutin, O.V., Bowling, B., Hendrix, J., Cai, Y., Dressler, G.R., and Oliver, G. (2006). Six2 is required for suppression of nephrogenesis and progenitor renewal in the developing kidney. *EMBO J.* *25*, 5214–5228.
- Short, K.M., Combes, A.N., Lefevre, J., Ju, A.L., Georgas, K.M., Lamberton, T., Cairncross, O., Rumballe, B.A., McMahon, A.P., Hamilton, N.A., et al. (2014). Global Quantification of Tissue Dynamics in the Developing Mouse Kidney. *Dev. Cell* *29*, 188–202.
- Sim, E.U.-H., Smith, A., Szilagi, E., Rae, F., Ioannou, P., Lindsay, M.H., and Little, M.H. (2002). Wnt-4 regulation by the Wilms' tumour suppressor gene, WT1. *Oncogene* *21*, 2948–2960.
- Stiller, C.A., and Parkin, D.M. (1990). International variations in the incidence of childhood renal tumours. *Br. J. Cancer* *62*, 1026–1030.
- Subramanian, A., Sidhom, E.-H., Emani, M., Vernon, K., Sahakian, N., Zhou, Y., Kost-Alimova, M., Slyper, M., Waldman, J., Dionne, D., et al. (2019). Single cell census of human kidney organoids shows reproducibility and diminished off-target cells after transplantation. *Nat. Commun.* *10*, 1–15.
- Taguchi, A., and Nishinakamura, R. (2017). Higher-Order Kidney Organogenesis from Pluripotent Stem Cells. *Cell Stem Cell* *21*, 1–17.
- Taguchi, A., Kaku, Y., Ohmori, T., Sharmin, S., Ogawa, M., Sasaki, H., and Nishinakamura, R. (2014). Redefining the In Vivo Origin of Metanephric Nephron Progenitors Enables Generation of Complex Kidney Structures from Pluripotent Stem Cells. *Cell Stem Cell* *14*, 53–67.
- Takahashi, K., and Yamanaka, S. (2006). Induction of Pluripotent Stem Cells from Mouse Embryonic and Adult Fibroblast Cultures by Defined Factors. *Cell* *126*, 663–676.
- Takahashi, K., Tanabe, K., Ohnuki, M., Narita, M., Ichisaka, T., Tomoda, K., and Yamanaka, S. (2007). Induction of Pluripotent Stem Cells from Adult Human Fibroblasts by Defined Factors. *Cell* *131*, 861–872.
- Takasato, M., Er, P.X., Chiu, H.S., Maier, B., Baillie, G.J., Ferguson, C., Parton, R.G., Wolvetang, E.J., Roost, M.S., Chuva de Sousa Lopes, S.M., et al. (2015). Kidney organoids from human iPS cells contain multiple lineages and model human nephrogenesis. *Nature* *526*, 564–568.
- Tanigawa, S., Wang, H., Yang, Y., Sharma, N., Tarasova, N., Ajima, R., Yamaguchi, T.P., Rodriguez, L.G., and Perantoni, A.O. (2011). Wnt4 induces nephronic tubules in metanephric mesenchyme by a non-canonical mechanism. *Dev. Biol.* *352*, 58–69.
- Tanigawa, S., Islam, M., Sharmin, S., Naganuma, H., Yoshimura, Y., Haque, F., Era, T., Nakazato, H., Nakanishi, K., Sakuma, T., et al. (2018). Organoids from Nephrotic Disease-Derived iPSCs Identify Impaired NEPHRIN Localization and Slit Diaphragm Formation in Kidney Podocytes. *Stem Cell Rep.* *11*, 1–14.
- Terada, Y., Jo, N., Arakawa, Y., Sakakura, M., Yamada, Y., Ukai, T., Kabata, M., Mitsunaga, K., Mineharu, Y., Ohta, S., et al. (2019). Human Pluripotent Stem Cell-Derived Tumor Model Uncovers the Embryonic Stem Cell Signature as a Key Driver in Atypical Teratoid/Rhabdoid Tumor. *Cell Rep.* *26*, 2608–2621.

- The Cancer Genome Atlas Research Network (2016). Comprehensive Molecular Characterization of Papillary Renal-Cell Carcinoma. *N. Engl. J. Med.* *374*, 135–145.
- Torrezan, G.T., Ferreira, E.N., Nakahata, A.M., Barros, B.D.F., Castro, M.T.M., Correa, B.R., Krepischi, A.C.V., Olivieri, E.H.R., Cunha, I.W., Tabori, U., et al. (2014). Recurrent somatic mutation in DROSHA induces microRNA profile changes in Wilms tumour. *Nat. Commun.* *5*, 1–10.
- Treger, T.D., Chowdhury, T., Pritchard-Jones, K., and Behjati, S. (2019). The genetic changes of Wilms tumour. *Nat. Rev. Nephrol.* *15*, 240–251.
- Trink, A., Kanter, I., Pode-Shakked, N., Urbach, A., Dekel, B., and Kalisky, T. (2018). Geometry of Gene Expression Space of Wilms' Tumors From Human Patients. *Neoplasia* *20*, 871–881.
- Tsialikas, J., and Romer-Seibert, J. (2015). LIN28: roles and regulation in development and beyond. *Development* *142*, 2397–2404.
- Urbach, A., Yermalovich, A., Zhang, J., Spina, C.S., Zhu, H., Perez-Atayde, A.R., Shukrun, R., Charlton, J., Sebire, N., Mifsud, W., et al. (2014). Lin28 sustains early renal progenitors and induces Wilms tumor. *Genes Dev.* *28*, 971–982.
- Villegas, F., Lehalle, D., Mayer, D., Rittirsch, M., Stadler, M.B., Zinner, M., Olivieri, D., Vabres, P., Duplomb-Jego, L., De Bont, E.S.J.M., et al. (2019). Lysosomal Signaling Licenses Embryonic Stem Cell Differentiation via Inactivation of Tfe3. *Cell Stem Cell* *24*, 257–270.e8.
- Viswanathan, S.R., and Daley, G.Q. (2010). Lin28: A MicroRNA Regulator with a Macro Role. *Cell* *140*, 445–449.
- Viswanathan, S.R., Powers, J.T., Einhorn, W., Hoshida, Y., Ng, T.L., Toffanin, S., O'Sullivan, M., Lu, J., Phillips, L.A., Lockhart, V.L., et al. (2009). Lin28 promotes transformation and is associated with advanced human malignancies. *Nat. Genet.* *41*, 843–848.
- Walz, A.L., Ooms, A., Gadd, S., Gerhard, D.S., Smith, M.A., Guidry Auvil, J.M., Meerzaman, D., Chen, Q.-R., Hsu, C.H., Yan, C., et al. (2015). Recurrent DGCR8, DROSHA, and SIX Homeodomain Mutations in Favorable Histology Wilms Tumors. *Cancer Cell* *27*, 286–297.
- Wan, L., Chong, S., Xuan, F., Liang, A., Cui, X., Gates, L., Carroll, T.S., Li, Y., Feng, L., Chen, G., et al. (2020). Impaired cell fate through gain-of-function mutations in a chromatin reader. *Nature* *577*, 121–126.
- Wegert, J., Bausenwein, S., Roth, S., Graf, N., Geissinger, E., and Gessler, M. (2012). Characterization of primary wilms tumor cultures as an in vitro model. *Genes, Chromosomes Cancer* *51*, 92–104.
- Wegert, J., Ishaque, N., Vardapour, R., Geörg, C., Gu, Z., Bieg, M., Ziegler, B., Bausenwein, S., Nourkami, N., Ludwig, N., et al. (2015). Mutations in the SIX1/2 Pathway and the DROSHA/DGCR8 miRNA Microprocessor Complex Underlie High-Risk Blastemal Type Wilms Tumors. *Cancer Cell* *27*, 298–311.
- Wegert, J., Zauter, L., Appenzeller, S., Otto, C., Bausenwein, S., Vokuhl, C., Ernestus, K., Furtwängler, R., Graf, N., and Gessler, M. (2019). High-risk blastemal Wilms tumor can be modeled by 3D spheroid cultures in vitro. *Oncogene* *39*, 849–861.
- Wu, H., Uchimura, K., Donnelly, E.L., Kirita, Y., Morris, S.A., and Humphreys, B.D. (2018). Comparative Analysis and Refinement of Human PSC-Derived Kidney Organoid Differentiation with Single-Cell Transcriptomics. *Cell Stem Cell* *23*, 869–881.
- Xu, J., Wong, E.Y.M., Cheng, C., Li, J., Sharkar, M.T.K., Xu, C.Y., Chen, B., Sun, J., Jing, D., and Xu, P.-X. (2014). Eya1 Interacts with Six2 and Myc to Regulate Expansion of the Nephron Progenitor Pool during Nephrogenesis. *Dev. Cell* *31*, 434–447.

References

Xu, P.-X., Zheng, W., Huang, L., Maire, P., Laclef, C., and Silviu, D. (2003). Six1 is required for the early organogenesis of mammalian kidney. *Development* *130*, 3085–3094.

Yermalovich, A.V., Osborne, J.K., Sousa, P., Han, A., Kinney, M.A., Chen, M.J., Robinton, D.A., Montie, H., Pearson, D.S., Wilson, S.B., et al. (2019). Lin28 and let-7 regulate the timing of cessation of murine nephrogenesis. *Nat. Commun.* *10*, 1–11.